

CHARACTERIZATION OF SURFACE ROUGHNESS OF BARE AGRICULTURAL
SOILS USING LIDAR

By

JUAN CARLOS FERNANDEZ-DIAZ

A DISSERTATION PRESENTED TO THE GRADUATE SCHOOL
OF THE UNIVERSITY OF FLORIDA IN PARTIAL FULFILLMENT
OF THE REQUIREMENTS FOR THE DEGREE OF
DOCTOR OF PHILOSOPHY

UNIVERSITY OF FLORIDA

2010

© 2010 Juan Carlos Fernandez-Diaz

To my family and to all of you who inspired me to be curious and work hard

ACKNOWLEDGMENTS

First and foremost, I want to acknowledge the great support and guidance from the members of my supervisory committee: Ramesh Shrestha, Jasmeet Judge, William Carter, David Bloomquist and K. Clint Slatton. I thank them for sharing with me their knowledge, experience and spirit; and for guiding me to the completion of this endeavor. I'm also grateful to the persons and institutions that make the University of Florida Alumni Fellowship a reality, and those who support the department of civil engineering. Through them, I had the unique opportunity to reach the summit of higher education in one of the top public universities in the United States of America.

Next, I would like to thank my friends, classmates and colleagues from the Geosensing Systems Engineering program; the National Science Foundation (NSF) National Center for Airborne Laser Mapping (NCALM); and the Center for Remote Sensing at the Department of Agricultural and Biological Engineering; who provided me with invaluable support to complete this work. Finally, I would like to express my deep gratitude to my friends, parents and siblings. Their support and encouragement was crucial to my success in the UF Geosensing Graduate Program.

TABLE OF CONTENTS

| | <u>page</u> |
|--|-------------|
| ACKNOWLEDGMENTS..... | 4 |
| LIST OF TABLES..... | 8 |
| LIST OF FIGURES..... | 10 |
| LIST OF ABBREVIATIONS..... | 13 |
| ABSTRACT..... | 14 |
| CHAPTER | |
| 1 INTRODUCTION AND LITERATURE REVIEW | 18 |
| Introduction..... | 18 |
| Literature Review..... | 20 |
| Characterization of Surface Roughness..... | 20 |
| Surface Digitization Techniques..... | 23 |
| Multi-Scale Nature of Agricultural Surfaces and Detrending Methods..... | 26 |
| Current Limitations of Surface Roughness Characterization..... | 28 |
| Scanning light detection and ranging (LIDAR) technologies..... | 29 |
| 2 CHARACTERIZATION OF GROUND-BASED LIDAR ERRORS AND ACCURACY ASSESSMENT OF DERIVED ROUGHNESS PARAMETERS FROM TWO-DIMENSIONAL (2D) PROFILES | 36 |
| Characterization of Ground-based LiDAR Errors..... | 39 |
| Accuracy Assessment Based on Synthetic Generated Profiles..... | 40 |
| Accuracy of Derived Autocorrelation Function (ACF)..... | 41 |
| Accuracy of Derived of Random Height Root Mean Square (RMS _h)..... | 42 |
| Accuracy of Derived Correlation Lengths..... | 43 |
| Accuracy Assessment Based on Roughness References..... | 43 |
| Digitization Fidelity of the Instruments..... | 45 |
| Accuracy of Derived RMS _h | 46 |
| Validation with Agricultural Soil Measurements..... | 47 |
| Comparison of RMS _h Values..... | 47 |
| Comparison of Correlation Lengths..... | 47 |
| Autocorrelation Functions of Agricultural Soils..... | 48 |
| Chapter Conclusions..... | 49 |
| 3 TESTING ROUGHNESS CHARACTERIZATION ASSUMPTIONS USING A DATABASE OF 2D PROFILES OBTAINED WITH GROUND-BASED LIDAR | 68 |
| Instrumentation and Datasets..... | 68 |

| | |
|--|-----|
| Mobile Terrestrial Laser Scanner (M-TLS) | 68 |
| Data Collection and Preprocessing | 69 |
| 2D Profile Database | 71 |
| Testing Roughness Characterization Assumptions | 72 |
| Value Ranges for Roughness Parameters | 72 |
| Sensitivity of Roughness Parameters to the Detrending Procedure | 73 |
| Correlation between RMS _h and Correlation Lengths | 74 |
| Exponential or Gaussian ACF Models | 75 |
| Chapter Conclusions | 76 |
| | |
| 4 DERIVING THREE DIMENSIONAL (3D) ROUGHNESS METRICS FROM GROUND-BASED LIDAR DIGITAL ELEVATION MODELS (DEMS) | 82 |
| | |
| Datasets and Preprocessing | 83 |
| Averaging Parameter Values Obtained From 2D Profiles | 85 |
| Extending 2D Formulations to 3D | 86 |
| Comparison between 2D and 3D Roughness Parameter Values | 89 |
| Impact of Roughness Underestimation on Microwave Observables | 92 |
| Advanced Detrending and Scale Separation Methods for 3D DEMs | 93 |
| Chapter Conclusions | 95 |
| | |
| 5 THE APPLICATION OF AIRBORNE LIDAR TO MAP SURFACE ROUGHNESS OF LARGE AREAS | 111 |
| | |
| Airborne LIDAR Instrumentation and Datasets | 112 |
| Profiles from a Single Scan Line | 115 |
| Footprint Scale Roughness from Return Waveform Analysis | 116 |
| Point Cloud Binning | 120 |
| Validation of Airborne Roughness Maps | 120 |
| Chapter Conclusions | 122 |
| | |
| 6 CONCLUSIONS AND RECOMMENDATIONS | 131 |
| | |
| Conclusions | 131 |
| Recommendations | 133 |
| Main Contributions | 134 |
| | |
| APPENDIX | |
| | |
| A MICROWAVE SCATTERING AND EMISSION MODELS APPLIED TO SOIL MOISTURE MAPPING | 135 |
| | |
| B IMPROVEMENT TO THE MESHBOARD PROFILE DIGITIZATION METHOD.... | 139 |
| | |
| C SELECTED MATLAB SCRIPTS | 147 |
| | |
| Fit a Plane and Level a Point Cloud | 147 |
| 2D Detrending Function | 147 |

| | |
|---|-----|
| 2D Roughness Parameters Determination Function..... | 148 |
| 2D Accuracy Assessment with Roughness References | 150 |
| 3D Correlation Length from DEMs..... | 155 |
| RMS _h from Single Scan Line from Airborne LiDAR Data | 157 |
| Meshboard Digitizing and Correction..... | 158 |
| LIST OF REFERENCES | 165 |
| BIOGRAPHICAL SKETCH..... | 171 |

LIST OF TABLES

| <u>Table</u> | <u>page</u> |
|--|-------------|
| 2-1 Mean difference in the exponent of generalized power law for profiles with exponential and Gaussian ACF. | 59 |
| 2-2 RMSE (cm) in the estimation of RMS _h for profiles with exponential ACF..... | 60 |
| 2-3 RMSE (cm) in the estimation of correlation length for profiles with exponential and Gaussian ACF. | 61 |
| 2-4 Mean difference (cm) of correlation lengths for profiles with exponential and Gaussian ACF. | 62 |
| 2-5 Raw results obtained from the accuracy assessment experiments. | 63 |
| 2-6 Summary of results obtained from the accuracy assessment experiments. | 65 |
| 2-7 Roughness parameter values obtained from agricultural soils using meshboard and LiDAR. | 66 |
| 2-8 Comparison of roughness parameter values of agricultural soils obtained from LiDAR and meshboard data. | 67 |
| 3-1 3D digital elevation models derived from LiDAR for the study..... | 81 |
| 3-2 Roughness parameter values in cm, derived from 20,072 profiles of agricultural soils..... | 81 |
| 3-3 Mean parameter and fit metric values for different ACF models..... | 81 |
| 4- 1 Correlation coefficient and RMSE in meters between correlation length values derived by averaging profile values and averaging the ACFs. | 104 |
| 4-2 Averaged oriented roughness parameter values obtained from 2D profiles extracted from the DEMs..... | 104 |
| 4-3 3D roughness parameters values obtained from the full DEM and averaging values obtained from 2D profiles. | 107 |
| 4-4 Comparison of 3D roughness parameter values obtained from different approaches..... | 109 |
| 4-5 Difference in microwave observables due to errors in roughness parameterization..... | 109 |
| 4-6 Roughness Parameters derived from 3D models of quasi-periodic surfaces. .. | 110 |

| | | |
|-----|---|-----|
| 5-1 | Optech GEMINI Airborne Laser Terrain Mapper (ALTM) specifications | 130 |
| 5-2 | Optech waveform digitizer specifications..... | 130 |
| 5-3 | Airborne LiDAR datasets | 130 |

LIST OF FIGURES

| <u>Figure</u> | <u>page</u> |
|--|-------------|
| 1-1 Two configurations of reference surface and height random components. | 32 |
| 1-2 Synthetic generated profiles with exponential ACF, an RMS _h of 1cm, and a correlation length of 5 cm. | 32 |
| 1-3 Synthetic generated profile with Gaussian ACF, an RMS _h of 1cm, and a correlation length of 5 cm. | 32 |
| 1-4 Common autocorrelation functions shapes. | 33 |
| 1-5 A meshboard used for surface roughness studies..... | 33 |
| 1-6 A pin profiler deployed over vegetated terrain. | 34 |
| 1-7 A ground-based LiDAR scanner mapping an agriculture soil. | 34 |
| 1-8 Detrending effects on roughness parameter values. | 35 |
| 2-1 Test to characterize of LiDAR random noise..... | 51 |
| 2-2 DEM derived from a LiDAR scan of a smooth flat target. | 51 |
| 2-3 Elevation deviations from the smooth surface, extracting and concatenating profiles along the row direction of the DEM. | 52 |
| 2-4 Characterization of ground-based LiDAR random errors..... | 52 |
| 2-5 Random seed sequence from which correlated sequences are generated. | 52 |
| 2-6 Gaussian and exponential weighting functions used in the moving average method. | 53 |
| 2-7 Generated profile with a Gaussian ACF. | 53 |
| 2-8 Generated profile with an exponential ACF. | 53 |
| 2-9 Section of a pseudorandom roughness reference with an RMS _h of 2 cm. | 54 |
| 2-10 Section of a correlated roughness reference with an RMS _h of 2.7 cm. | 54 |
| 2-11 Scanning geometry of roughness references using ground-based LiDAR. | 54 |
| 2-12 Inputs into the Matlab script used to perform the accuracy assessment based on roughness references. | 55 |

| | | |
|------|---|-----|
| 2-13 | Random component extracted from the reference, the meshboard, and LiDAR-derived profiles..... | 56 |
| 2-14 | Results of the RMS _h accuracy assessment. | 56 |
| 2-15 | Simultaneous profile digitizing with A) meshboard and B) LiDAR..... | 57 |
| 2-16 | Comparison of RMS _h values of bare agricultural soils obtained from meshboard and LiDAR. | 57 |
| 2-17 | Difference between meshboard and LiDAR-derived correlation lengths of bare agricultural soils..... | 58 |
| 3-1 | The M-TLS system performing agricultural surface scanning operations. | 77 |
| 3-2 | Point cloud renderings of a ground-based LiDAR dataset at different processing steps..... | 77 |
| 3-3 | Samples of studied soil surface and their ground-based LiDAR derived 3D DEMs..... | 78 |
| 3-4 | Effects of detrending on the derived roughness parameters.. | 78 |
| 3-5 | Dispersion plots of the random height component derived correlation lengths and RMS _h for the different detrending methods. | 79 |
| 3-6 | Histograms of the exponent values for the Power Law Spectrum ACF model obtained from the soil profiles..... | 79 |
| 3-7 | Histograms of the R ² values of the fit of the observed ACF model with respect to the theoretical models. | 80 |
| 4-1 | Detrending a 3D DEM with linear, quadratic models and a FFT low pass filter..... | 97 |
| 4-2 | Directional roughness..... | 98 |
| 4-3 | Deriving 3D correlation length. | 98 |
| 4-4 | 3D correlation length as a function of the horizontal angle. | 99 |
| 4-5 | 3D Correlation length of a DEM with linear features..... | 100 |
| 4-6 | 3D Correlation length of a DEM after removing the linear features. | 101 |
| 4-7 | Dispersion plots of the 3D RMS _h and the averaged values of RMS _h derived from profiles..... | 102 |

| | | |
|------|---|-----|
| 4-8 | Dispersion plots of the averaged 3D correlation lengths and the averaged from profiles..... | 102 |
| 4-9 | Two stage wavelet bank used to decompose a 3D DEM. | 103 |
| 4-10 | Detrending of a quasi-periodic surface (#20)..... | 103 |
| 5-1 | Geometry of airborne scanning LiDAR data collection. | 124 |
| 5-2 | The National Center for Airborne Laser Mapping (NCALM) Gemini ALTM and waveform digitizer..... | 125 |
| 5-3 | Airborne LiDAR roughness maps. | 126 |
| 5-4 | Surface roughness map of a bare soil area. | 127 |
| 5-5 | Validation areas for the airborne derived roughness maps marked as squares 1 and 2 in 5-3 A. | 128 |
| 5-6 | Validation of the airborne derived RMS _h from the three proposed methods compared to RMS _h values derived from ground-based LiDAR data through similar processing. | 129 |
| A2-1 | Meshboard and the marked control points. | 145 |
| A2-2 | Flat smooth profile at different processing steps. | 145 |
| A2-3 | Coordinate differentials and distortion correction factors. | 146 |

LIST OF ABBREVIATIONS

| | |
|------------------|---|
| ACF | Autocorrelation Function |
| ALTM | Airborne Laser Terrain Mapper |
| CCD | Charged Coupled Device |
| CL | Correlation Length |
| COTS | Commercial-off-the-shelf |
| DEM | Digital Elevation Model |
| EDM | Electronic Distance Measurement |
| ESA | European Space Agency |
| FFT | Fast Fourier Transform |
| FWHM | Full Width at Half Max |
| IEM | Integral Equation Model |
| IFAS | Institute of Food and Agricultural Sciences |
| LiDAR | Light Detection and Ranging. |
| MicroWEX | Microwave Water and Energy Balance Experiment |
| M-TLS | Mobile Terrestrial Laser Scanner system |
| NCALM | National Center for Airborne Laser Mapping |
| PSREU | Plant Science Research and Education Unit |
| RMSE | Root Mean Square Error |
| RMS _h | Root Mean Square of random height variations |
| SAR | Synthetic Aperture Radar |
| SMAP | Soil Moisture Active & Passive |
| SMOS | Soil Moisture & Ocean Salinity |
| UF | University of Florida |
| UF-GEM | University of Florida, Geosensing Engineering and Mapping center. |

Abstract of Dissertation Presented to the Graduate School
of the University of Florida in Partial Fulfillment of the
Requirements for the Degree of Doctor of Philosophy

CHARACTERIZATION OF SURFACE ROUGHNESS OF BARE AGRICULTURAL
SOILS USING LIDAR

By

Juan Carlos Fernandez-Diaz

December 2010

Chair: Ramesh Shrestha
Major: Civil Engineering

The characterization of surface roughness is an active area of research with relevance and applications to many fields of sciences and engineering. For example, in geology it is used to infer what type of process gave origin to particular surface morphologies. In hydrology it is used to model surface water runoff. Here the goal is to facilitate the use of active and passive microwave sensors to map soil moisture. For this purpose, surface roughness is considered the random height variations of the soil surface relative to a reference surface. Roughness is thus considered a stationary, single-scale random process characterized by three parameters: the root mean square (RMS_h) of the height variations, the autocorrelation function (ACF) and its correlation length (CL). To obtain these parameters the general practice is to record the terrain height variation along two-dimensional (2D) transects using mechanical or non contact profilers. The data from these transects are first detrended to separate the reference surface and the random component, and then the random component is used to compute the roughness parameters.

The current definition and parameterization of surface roughness have the advantages of being simple, but it is generally accepted that the way soil roughness

needs to be measured and described for the modeling of microwave phenomena is not yet fully understood. Some practical challenges currently faced include: obtaining precise and accurate roughness parameter values from field instruments and techniques; obtaining measurements that do not contradict the current assumptions of single scale, isotropy and simple Gaussian or exponential ACFs; obtaining good agreement between soil moisture measurements and the values derived from the microwave models using scattering and or emission observations and in situ roughness measurements. The research hypotheses tested in this work, that explain these limitations are: the existence of systematic and random errors that are not properly accounted for in the measurements; the inadequate practice of using 2D profiles to derive 3D characteristics of the surface; the scaling up of *in situ* roughness measurements under the assumptions of homogeneity and isotropy. To test these hypotheses, Scanning light detection and ranging (LiDAR) technology was employed.

LiDAR enables the digitization of surface height variations in three-dimensions (3D) and thus allows for an improved characterization of surface roughness. To address the above mentioned challenges in the characterization of surface roughness with LiDAR technology, a multi-step approach was followed. The first step was to investigate the factors that affect the precision and accuracy of roughness parameterization from 2D measurements. The next step was to analyze and test the current assumptions of roughness characterization following the traditional 2D formulation. This was followed by developing methodologies to characterize roughness from 3D information; that is truly representative of the entire surface. Finally, the issue of scaling was addressed by developing methodologies to use airborne LiDAR to derive millimeter level roughness

maps of large areas and to prove the heterogeneity and anisotropy of roughness characteristics over large areas.

The issue of the accuracy and precision of roughness parameters was studied by performing two accuracy assessments and a direct comparison between a meshboard and the ground-based LiDAR. The first accuracy assessment was based on computer generation of random rough surfaces and the second based on measurements employing roughness references. Results indicate that to obtain accurate and repeatable parameter values it is necessary to properly characterize the instrument random errors. The height variation measurements obtained with any instrument are the result of the addition of two random processes: the surface roughness and the instrument random error. If the instrument error is not properly characterized and considered, the computed roughness parameter values will be corrupted and thus inaccurate. Of the parameters, the RMS_h is the least sensitive to instrument noise and it was determined that this parameter can be derived from ground-based LiDAR with an accuracy of better than 1mm. The achievable accuracy in retrieving the ACF and associated CL depends on the relative magnitudes of the surface's roughness and the instrument error. Correlation lengths can be accurately determined to better than a cm if the surface RMS_h is larger than 1 cm.

With regards to the assumptions used to characterize roughness using the traditional 2D formulation, it was found that agricultural surfaces exhibit multi-scale roughness characteristics. This contradicts the single-scale assumption. However, it is possible to obtain roughness at a particular scale if the proper detrending techniques are applied. It was also determined that the exponential and Gaussian ACF models are

just two limiting cases, and that the majority of surfaces have characteristic ACFs intermediate between these two models. In contrast to what has been commonly reported, no correlation was found between the RMS_h and CL. However, it was found that at small scales there is a possible negative correlation between RMS_h and the maximum observable CL.

3D characterization of surfaces of agricultural fields reveals that they are generally even more multi-scale in terms of their roughness than is evident from the 2D formulation. Roughness parameters obtained from the 2D formulation underestimate the characteristics of the surface; by 25% in terms of the RMS_h and 30% in terms of the CL. This is because profiles generally do not record the extremes of the surface in a single transect and do not necessarily follow the trend of the entire surface. The assumptions of homogeneity and isotropy were proved to not be valid even for small areas. 3D digital elevation models (DEMs) derived from ground-based LiDAR allow for the characterization of roughness with advanced tools in the spatial-temporal domain. When the characterization of millimeter level surface roughness of large areas is required, data from high resolution airborne LiDAR can be used. RMS_h derived from airborne data was within 1 mm of the RMS_h derived from ground-based LiDAR data.

It is expected that the results from this work will motivate a paradigm shift in the way surface roughness data is derived, from a limited sample of in-situ 2D transects to remotely determining 3D roughness of large areas.

CHAPTER 1 INTRODUCTION AND LITERATURE REVIEW

Introduction

Characterization of surface roughness is an active research topic, with potential applications in diverse fields of the basic and applied sciences, including physics, geology, geomorphology, hydrology, ecology, agriculture, civil engineering, manufacturing, and remote detection and sensing [1] - [5]. One use of surface roughness characterization is in the remote sensing and mapping of soil moisture using active and passive microwave sensors [6]. The microwave scattering or emission from a soil surface depends not only on the wavelength, polarization, and angle of incidence of the radiation, but also on the soil's moisture and its surface roughness [2]. For the purpose of modeling microwave emission and scattering for the retrieval of soil moisture, roughness is considered to be the surface height's random variations with respect to a reference. Contact and non-contact instruments are used to digitize the surface height variations along two-dimensional (2D) transects. The digitized transect is then detrended to separate the random height variations from topographic trends. The height variations are then described by three parameters: the root mean square of height (RMS_h), the autocorrelation function, and the correlation length (CL). Despite the relative simplicity of the definition of surface roughness and the traditional surface profiling methods, several limitations and challenges have been encountered by researchers over the years. Based on these challenges, a recent literature review by Verhoest et al. [7] concluded that the method to describe and measure soil surface roughness for the modeling of microwave backscattering is not fully understood.

This dissertation describes the results of experiments designed to characterize and parameterize the roughness of bare agricultural fields using scanning light detection and ranging (LiDAR) technologies. These experiments were performed using a multi-step approach aimed at overcoming some of these documented challenges and limitations. This chapter presents a literature review. The review covers the aspects of characterization of surface roughness; traditional methods and instruments used to digitize surface heights; the current limitations and challenges to overcome to better characterize roughness for its use in microwave models; and finally, there is a short overview of LiDAR technologies. Chapter 2 describes the experiments that constitute the foundation of this study. These experiments were conducted to determine what factors affect the precision and accuracy of the parameters used to characterize roughness derived from surface measurements. Once the ability of the ground-based LiDAR to derive accurate values of roughness parameters was established, the next step consisted of collecting a large database of 2D surface roughness measurements. These measurements were used to test some of the current assumptions used in the characterization of roughness.

Chapter 3 presents the collection and processing of the roughness database, a description of the performed tests, and their results. These tests are also a validation of the different computational tools created to derive 2D roughness parameters values, as the results obtained from them reproduce the current state of knowledge and the known limitations. Having validated the instruments and tools used to perform the roughness characterization in the traditional 2D formulation, the next step was an extension to characterize roughness in a 3D formulation utilizing the 3D information obtained using

the ground-based scanning LIDAR. This characterization of surface roughness in 3D is covered in Chapter 4.

The ground-based LiDAR proved to be an accurate and convenient instrument for the characterization of millimeter level roughness in both 2D and 3D, but limited in terms of the area it can characterize. For the characterization of surface roughness of much larger areas, the use of airborne LiDAR was explored. This is the topic covered in Chapter 5. In addition to the specific conclusions presented in each chapter, general conclusions of the overall work are presented in Chapter 6. Chapter 6 also includes a list of the major contributions of this work toward the general advancement of knowledge and recommendations for further work. Also included as appendices to this dissertation are a description of the most common used microwave scattering and emission models, an improved method to digitize surface transects using the meshboard, and some of the Matlab scripts developed to perform this research.

Literature Review

Characterization of Surface Roughness

There are two main approaches to quantify surface roughness. The first and most common is to assume a mathematically tractable form, of a statistical nature. The second approach consists of measuring and cataloging topographic expressions of unrelated of surfaces without *a priori* assumptions about their final form [1]. Most current microwave scattering or emission models take the first approach, and assume that soil surface roughness can be described as a single scale, stationary, Gaussian, random process. This means that roughness can be fully described by the mean, variance and autocorrelation function of the surface height variations, and that these parameters will have the same value independent of the size of the surface under study [8]. According

to Ulaby et al. [9], for microwave emission and scattering models, soil roughness can be considered as a stochastic varying height of the soil surface with respect to a reference surface. The reference surface can be a) the mean surface if there are only random variations to it, or b) the unperturbed surface of a periodic pattern (Figure 1-1). From the random component, the roughness parameters are computed from the following formulas given in [9].

From a representative sample of a continuous surface height random component ($z(x,y)$) with dimensions L_x and L_y centered at the origin, the first (mean) and second moments of the surface random component are given by:

$$\bar{z} = \frac{1}{L_x L_y} \int_{-\frac{L_x}{2}}^{\frac{L_x}{2}} \int_{-\frac{L_y}{2}}^{\frac{L_y}{2}} z(x, y) dx dy , \quad (1-1)$$

$$\overline{z^2} = \frac{1}{L_x L_y} \int_{-\frac{L_x}{2}}^{\frac{L_x}{2}} \int_{-\frac{L_y}{2}}^{\frac{L_y}{2}} z^2(x, y) dx dy . \quad (1-2)$$

The standard deviation of the height variations (σ_h) or height RMS (RMS h) is:

$$\sigma_h = RMSh = \sqrt{\overline{z^2} - \bar{z}^2} . \quad (1-3)$$

If the random component surface $z(x,y)$ is isotropic, then the previous formulas can be reduced to two dimensions, z and x or y . Also, the general practice is to record the surface height variation along 2D profiles $Z_s(x_i)$ at discrete intervals (Δx). After detrending the surface profile $Z_s(x_i)$ to obtain the random height component $z(x_i)$, the roughness parameters are then computed as described in [9] and as follows.

Random component height mean (should be zero):

$$\bar{z} = \frac{1}{N} \sum_{i=1}^N z_i . \quad (1-4)$$

The standard deviation of the height variations (σ_h) or height RMS (RMS h):

$$\sigma_h = RMS_h = \sqrt{\frac{1}{N-1} \left[\left(\sum_{i=1}^N z_i^2 \right) - N \times \bar{z}^2 \right]} . \quad (1-5)$$

The normalized autocorrelation function for lags h [2]:

$$\rho(h) = \rho(j\Delta x) = \frac{\sum_{i=1}^{N-j} (z_i \times z_{i+j})}{\sum_{i=1}^N z_i^2} . \quad (1-6)$$

The correlation length (l) is defined as the lag for which [2] and [9]:

$$\rho(l) = \frac{1}{e} . \quad (1-7)$$

The normalized exponential autocorrelation function [2]:

$$\rho(h) = e^{\left(-\frac{|h|}{l} \right)} . \quad (1-8)$$

The normalized Gaussian autocorrelation function [2]:

$$\rho(h) = e^{\left(-\frac{h^2}{l^2} \right)} . \quad (1-9)$$

As shown in Figure 1-2, a surface with an exponential ACF is characterized by short range (high frequency) small amplitude height variations, whereas a surface with a Gaussian ACF (Figure 1-3) appears smoother at these higher frequencies or smaller scales [10]. However, the measured ACF of real soils are more complicated than these theoretical formulations. Some studies have observed that the ACF of natural surfaces falls somewhere between the Gaussian and the exponential ACF [11], and a generalized power law spectrum has been proposed to characterize their behavior [2]:

$$\rho(h) = e^{\left(\frac{h}{l}\right)^n} . \quad (1-10)$$

With $n = 1$ this ACF becomes the exponential, with $n = 2$ this ACF becomes the Gaussian, and explains the intermediate ACFs for $1 < n < 2$ [11]. Figure 1-4 shows the shape of the normalized Gaussian, exponential, and generalized power law autocorrelation functions for the same correlation length.

To better describe surface roughness, some researchers suggest an additional parameter, the RMS slope, which is the second derivative of the autocorrelation function evaluated at the origin or [8]:

$$m_{rms}^2 = -\sigma^2 \frac{d^2}{dh^2} \rho(h) \Big|_{h=0} . \quad (1-11)$$

The RMS slope is infinite for surfaces with exponential and power law ACF as can be inferred from Figure 1-4. For surfaces with different ACFs, the RMS slope can be approximated by [1]:

$$m_{rms} = \frac{\sigma_h}{l} . \quad (1-12)$$

Surface Digitization Techniques

There are two types of instruments used to obtain surface profiles to compute the roughness parameters for microwave modeling: a) contact instruments, such as the pin profiler and the meshboard, and b) non-contact instruments, such as LASER profilers, stereo imagers, and acoustic backscatter systems [1], [7], [12] - [14].

The meshboard is usually a metallic plate, generally 2 to 4 meters in length, on which a regular grid has been drawn. The meshboard is placed over the soil surface and a photograph is taken from a perpendicular position. The photograph is then

processed using special image processing software from which the digitized surface profile is obtained. Figure 1-5 shows a meshboard used for a surface roughness data collection over a plowed field. Among the advantages of the meshboard are its simplicity, ease of transportation, and low cost. Sources of error present in meshboard-derived profiles include: parallax and geometric distortion, which originate when the photograph is taken; and interpretation, digitalization, and interpolation errors, which arise in the image processing steps [13]. The pin profiler is in essence a meshboard with a frame that keeps the board suspended off the ground. A beam is welded at the lower edge of the board, on which uniformly spaced holes are drilled and through which metallic rods or pins can slide up or down. During a profile measurement, the board is leveled and the pins are freed to make contact with the ground. Looking down on the meshboard plate, the heads of the pins delineate the soil surface profile. Then the pins' heads against the meshboard are photographed. To obtain the digitized profile, a similar procedure as that described for the meshboard method is applied [7], [1], [13], [15]. Figure 1-6 shows a pin profiler used for surface roughness characterization of vegetated terrain. The main disadvantage of these mechanical methods is that they tend to disturb or destroy the surface that is under study. Meshboards have to be hammered into the soil, while needle-like profilers tend to penetrate into the surface yielding noisy height measurements [13]. An additional disadvantage to these methods is that data collection and processing are very time consuming.

Modern surface digitizing methods are based on non-contact instruments, which have the advantage of not disturbing the study surface. Examples of these instruments

include such systems as laser profiler, optical imaging, and acoustic backscattering. A description of an experimental acoustic backscatter system can be found in [14], and descriptions of stereoscopic optical imagers can be found in [1], [12], [16]. Of relevance to this dissertation are the laser-based instruments, among which, it is possible to make a distinction between prototype one-of-a-kind systems, designed specifically by research institutions to obtain surface roughness profiles and commercial-off-the-shelf (COTS) LiDAR scanners, designed mainly for surveying applications to map surfaces in 3D. Examples of the one-of-a-kind systems are the ESA CESBIO LASER profiler described in [13], the Wageningen University Micro-LASER relief meter described in [17], and the instantaneous-profile laser scanner covered in [18].

Increased availability of COTS LiDAR scanning systems over the past years has made possible their employment for surface roughness studies. However, as of this date very few studies on the characterization of soil surface roughness employing scanning LiDAR have been published. Some examples include work by Davenport et al., in which airborne mapping LiDAR has been used to automatically classify areas with different surface roughness characteristics [20] and on the characterization of the instrument errors applied to surface roughness studies [21]. Perez-Gutierrez et al. used a Trimble ground-based terrestrial LiDAR to obtain four 20 m x 20 m field-surface samples in the Duero Basin, in the north-central region of Spain. Their work confirmed the validity of the use of ground-based LiDAR to digitize agricultural soil surfaces. However, they did not publish the values for the traditional roughness parameters (RMS_h, CL, ACL) obtained from the LiDAR data [22]. Bryant et al. employed an Optech ILRIS-3D LiDAR scanner to digitize test areas at the Walnut Gulch experimental

watershed in southeastern Arizona. 2D profiles were extracted from the 3D surface data and compared to pin profiler measurements. They also attempted to characterize the LiDAR and pin profiler RMS error by digitizing flat surfaces with zero RMS. The obtained RMS was assumed to be a positive bias present in all measurements [15]. Figure 1-7 shows an IIRIS 3D LiDAR scanner, the same instrument employed by Bryant et al. for their study [15].

These studies with COTS LiDARS are limited pilot experiments and the potential of LiDAR to better characterize surface roughness and to overcome many of the limitations of the traditional methods has not been fully exploited. Also, to date there has been very little research on the characterization of 3D soil roughness using these digitization instruments. Most of them limit the 3D data obtained to extract 2D profiles and perform analyses based on the traditional transect methodology. Little is known about how the results obtained with the traditional 2D techniques compare to the ones obtained from 3D characterizations. COTS ground-based LiDARs have the potential to digitize height variations of surfaces with areas of tens of square meters at resolutions in millimeters, a significant advantage over the single short profiles obtained using traditional methods. Even with coarser resolution, Airborne LiDAR has the potential to map and characterize surface roughness at watershed and larger scales. Datasets of this extent so far have not been available, but would be extremely useful for the retrieval of soil moisture data from large-scale spaceborne radar and radiometer observations [6].

Multi-Scale Nature of Agricultural Surfaces and Detrending Methods

Romkens and Wang [23] recognized that agricultural soils exhibit roughness characteristics on four main scales: microrelief variations, which are due to individual

soil grains and aggregates; random roughness, which are surface height variations due to individual soil clods; oriented roughness, or surface height variations due to agricultural structures such as rows and furrows; and higher order roughness, which is the result of height variations on topographic scales. The effects of these roughness scales on microwave signatures depends on wavelength and angle of incidence, and it is generally accepted that the ones that need to be considered are the scales higher than 1/10 of the observational wavelength [24]. In principle, for use in microwave emission and scattering models, random roughness is the one that needs to be parameterized; the oriented and topographic roughness should be directly accounted for in the models [25]. The practical challenge becomes how to properly separate the different components of height variations at the different scales from field measured profiles. In other words, how to properly detrend the profile? The traditional approach for short profiles is to remove the first order or linear trend. For longer profiles four different methods are recommended in [2]. These methods are the application of 1) higher order polynomials, 2) 1-meter linear piecewise detrending, 3) moving average filters, and 4) a Fast Fourier Transform (FFT) based filter that removes higher wavelength components. In Figure 1-8, three detrending methods are applied to a single profile 5 meters long extracted from a ground-based LiDAR-derived surface grid. The first two of these detrending methods are based on linear and quadratic models, while the third method is an FFT-based filter. The FFT filter defines the trend from the frequency components with a spatial wavelength larger than a meter. Part A) of Figure 1-8 depicts the original surface profile and the trends that correspond to the first order, second order, and FFT

trends. It also shows the coefficient of determination (R^2) of the trend with respect to the observed profile, defined as:

$$R^2 = 1 - \frac{\sum_{i=1}^n (o_i - m_i)^2}{\sum_{i=1}^n (o_i - \bar{o})^2} = 1 - \frac{\sum_{i=1}^n (o_i - m_i)^2}{n \times \sigma_o^2}, \quad (1-13)$$

where, o_i is the i^{th} height observation point of the profile and m_i is the respective modeled height according to the trend. The R^2 is a measure of the “closeness” of the modeled trend to the observed data. Part B) shows the extracted height random component from the different detrending methods and their respective RMShs. In part C) of the figure, the autocorrelation functions of the random height components for the different detrending methods are plotted. It can be seen that, as the modeled trend fits better the observed data, both the RMSh and correlation length values are reduced. Optimal detrending will extract random height components at a single scale, which should yield a roughness parameter that reach an asymptotic value indifferent to the profile length [2]. A study by Bryant et al. demonstrated the sensitivity of soil moisture retrieval to the detrending technique used, reporting a variation in retrieval of more that 9% per volume between two different methods [15]. In a study based on synthetic surface profiles, Lievens et al. determined that for soil moisture retrieval, the difference between whether or not the proper detrending was applied could be as high as 25% per volume [25].

Current Limitations of Surface Roughness Characterization

Despite the simplicity of the above definitions and equations, a recent literature review [7], concluded that soil surface roughness description and measurement for the

modeling of backscattering is not fully understood. Current challenges in the characterization of surface roughness can be summarized as:

- Obtaining precise (repeatable) and accurate values of roughness parameters even for the same surface using different techniques and methods [2], [13], [15]. This limitation has been attributed to reasons that include systematic and random instrument errors; non-standardized field data collection practices; sensitivity of the roughness parameters to profile length, horizontal digitizing resolution, height variation accuracy, and detrending techniques.
- Obtaining comprehensive results that support the assumptions that roughness is a stationary single-scale process and that random height variations are isotropic, homogenous, and their autocorrelation functions can be explained either by the Gaussian or exponential ACF models [8], [12].
- Obtaining good agreement between soil moisture measurements and results obtained from the inversion of physical-analytical models that use spaceborne microwave sensor observations and *in situ* roughness measurements [26], [27], [28].

The hypotheses presented in this dissertation argue that these challenges arise because there are instrument errors that are not properly accounted for; the approach of deducing 3D roughness characteristics from a limited number of 2D profiles is not appropriate; that the scale at which roughness needs to be characterized has not been properly determined; and that roughness measurements from small sample profiles do not scale up to represent the roughness of large areas. Scanning LiDAR, mounted in both terrestrial and airborne platforms, is explored as a technological alternative to overcome these limitations.

Scanning light detection and ranging (LIDAR) technologies

Light detection and ranging (LiDAR) is an active remote sensing technique that uses electromagnetic radiation in the visible spectrum to measure the range to a target. Also, properties from the target may be deduced based on the reflection, scattering, absorption, fluorescence, or any other phenomena resulting from the interaction

between the radiation and the target. The origins of LiDAR can be traced to the late 1930s for two different applications: the study of atmospheric components in 1937 [29] and as electronic distance measuring (EDM) devices in 1938 [19]. However, the acronym LiDAR was introduced only in 1953 [29]. In the early days, focused light beams were used as energy source. Substantial advancement in LiDAR technology came with the invention of the laser in the late 1950s [30]. The laser allowed for a coherent, single frequency, and highly collimated beam of optical energy to be used as the energy source. With the implementation of the laser as the light source, the acronym LaDAR for laser detection and ranging came to use, and this is the nomenclature mainly used in military circles today.

In the late 1960s and early 1970s, the laser-based EDMs were capable of measuring distances of up to 60 km and soon were integrated into airborne platforms as the early LASER altimeters. In the late 1970s, optical scanning mechanisms were added to the airborne laser altimeters, allowing the laser beam to be steered in a direction perpendicular to the line of flight [19]. This was the origin of the current airborne scanning LiDAR that has allowed researchers and engineers to map the topography of large areas at fine resolutions with high precision and accuracy [30], [31]. The technology continued to evolve and advances resulted in the miniaturization of lasers, opto-mechanics, detectors, and electronics. Small self contained scanning LiDARs for terrestrial use became available at the end of the 1990s [19]. The principles of operation of these terrestrial or ground-based LiDARs are extensively discussed in [19].

The main advantage that Scanning LiDAR brings to the problem of roughness characterization is that it is capable of accurately reproducing the entire surface rather than under-representing it by transects. Ground-based LiDAR-derived digital elevation models can cover areas of tens to low hundreds of square meters, with sample spacing as low as a few millimeters. This allows for the characterization of surface features at high spatial bandwidths and fine resolutions. This in turn enables the accurate separation of the reference surface and the random components, and thus an accurate determination of the roughness parameters. In addition, information from 3D digital elevation models (DEMs) can be used to describe the directional properties and heterogeneous characteristics of a surface's roughness. Airborne LiDAR can improve the way surface roughness is currently characterized, going from sampling with a few in-situ profiles or relatively small surface models to remotely collecting 3D information of large areas. With this 3D information of large areas, an accurate characterization of surface roughness and its spatial variations can be obtained.

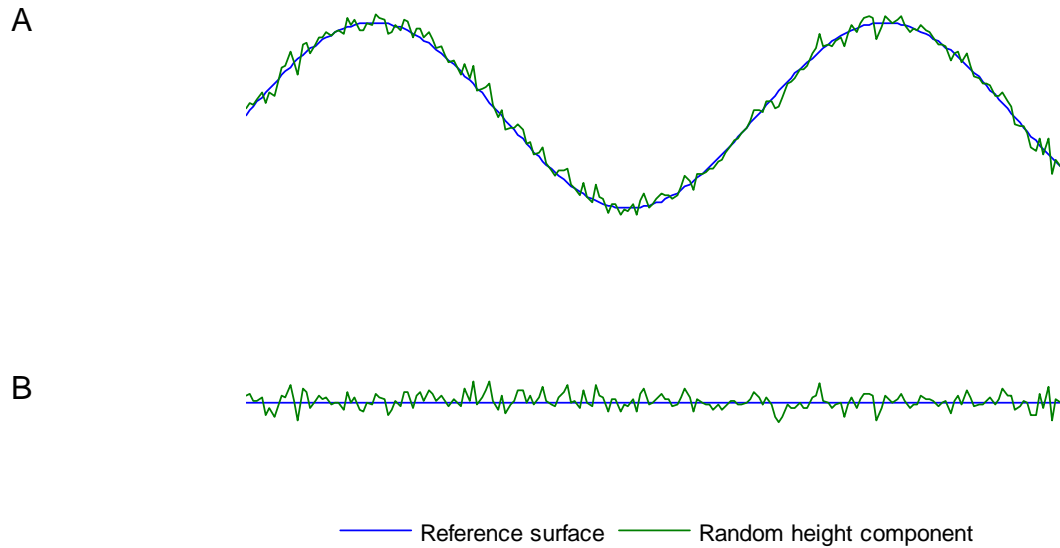


Figure 1-1. Two configurations of reference surface and height random components. a) Reference is a periodic surface. b) Reference is the mean surface.

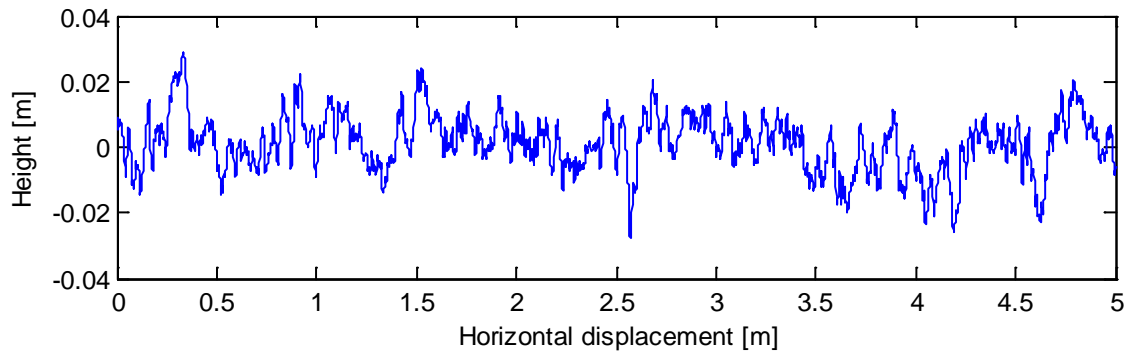


Figure 1-2. Synthetic generated profiles with exponential ACF, an RMS_h of 1cm, and a correlation length of 5 cm.

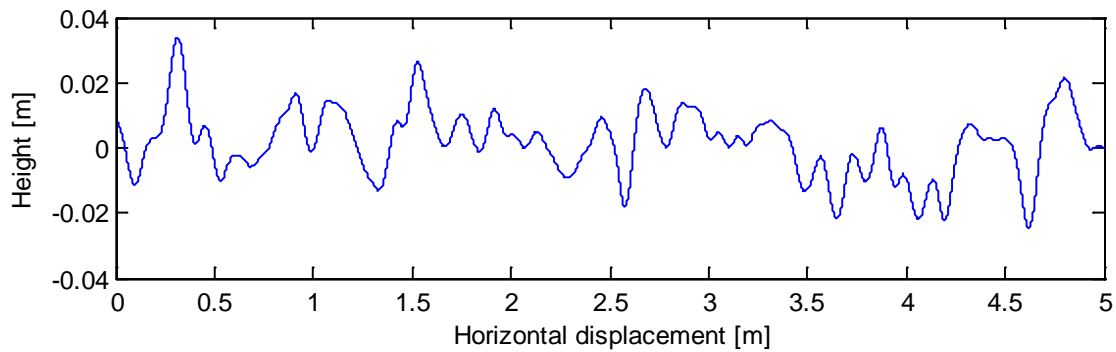


Figure 1-3. Synthetic generated profile with Gaussian ACF, an RMS_h of 1cm, and a correlation length of 5 cm.

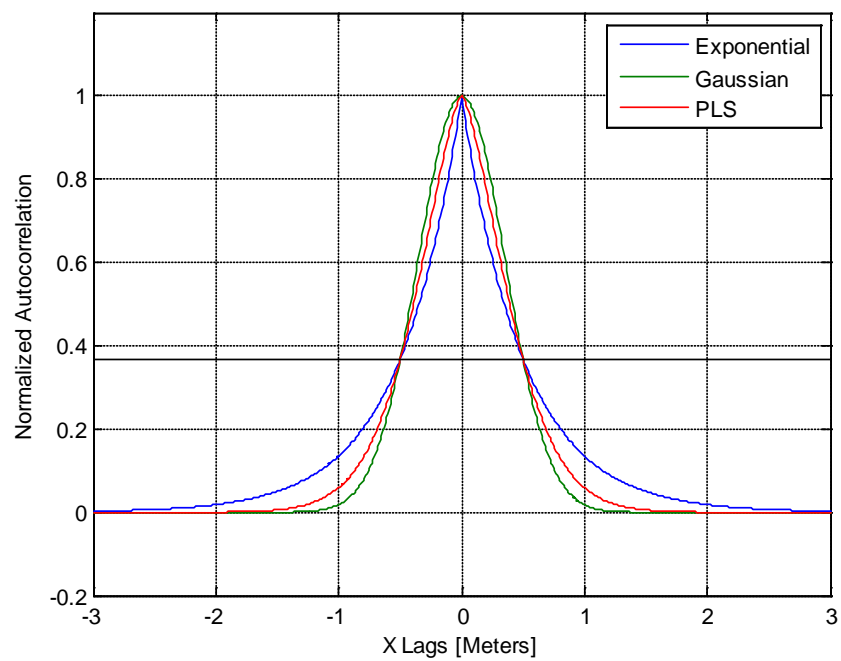


Figure 1-4. Common autocorrelation functions shapes.



Figure 1-5. A meshboard used for surface roughness studies.



Figure 1-6. A pin profiler deployed over vegetated terrain.



Figure 1-7. A ground-based LiDAR scanner mapping an agriculture soil.

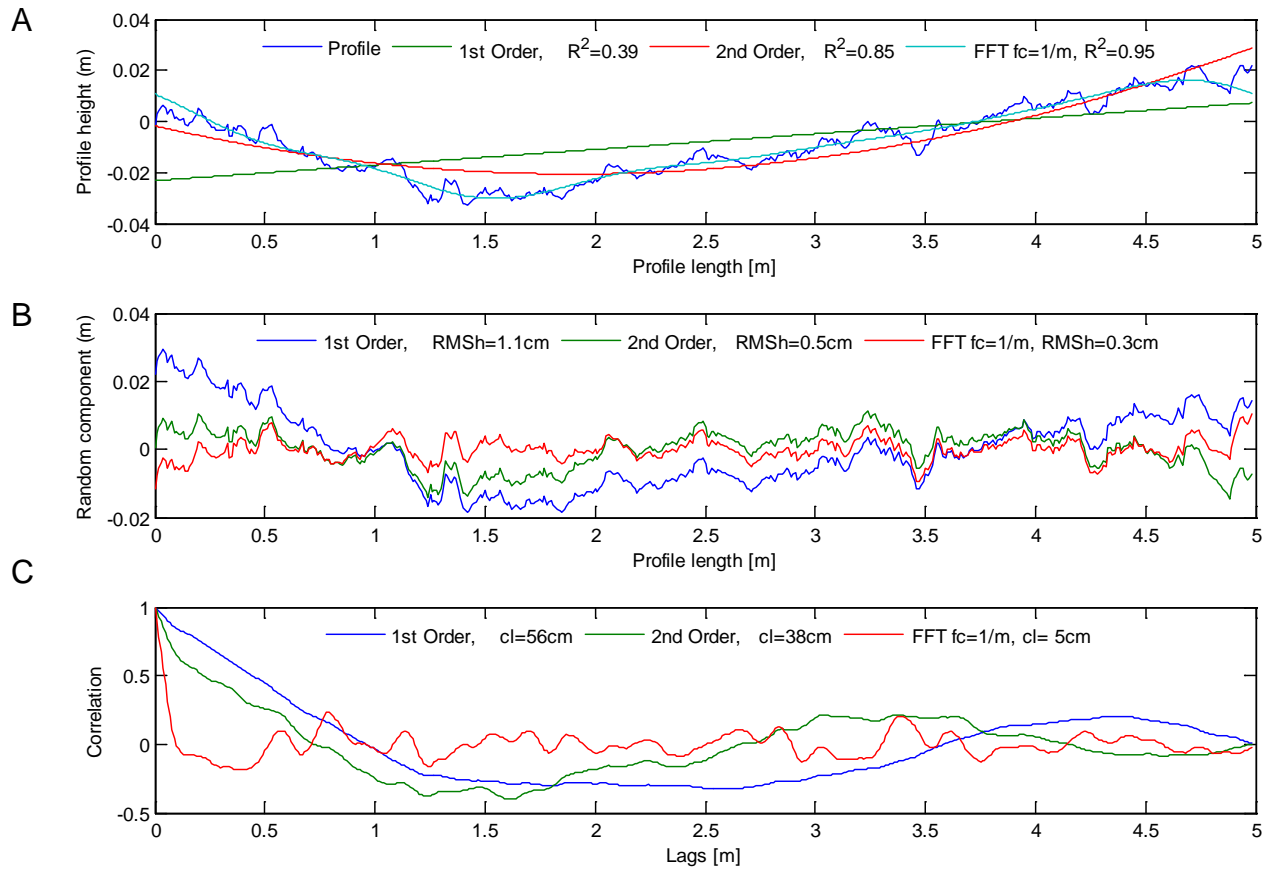


Figure 1-8. Detrending effects on roughness parameter values.

A) The original profile and the modeled trends. B) The extracted random component. C) Derived autocorrelation functions from the random component extracted from the different detrending methods.

CHAPTER 2

CHARACTERIZATION OF GROUND-BASED LIDAR ERRORS AND ACCURACY ASSESSMENT OF DERIVED ROUGHNESS PARAMETERS FROM TWO-DIMENSIONAL (2D) PROFILES

There are many aspects to the problem of obtaining repeatable (precise) and accurate roughness parameters from soil surfaces. Some issues include instrumental errors that affect the digitized profile; the capacity of the instruments to capture the minute height variations at fine resolutions; and non-standardized field data collection techniques in terms of digitized profile length and horizontal sample spacing. Of the roughness parameters, the root mean square of height variations (RMS_h) is the least problematic, as it is the least sensitive to instrumental errors and multiscale effects. The difficulty in obtaining consistent correlation lengths is due to the fact that the retrieval of the autocorrelation function is highly sensitive to noise induced by the instruments, detrending techniques, profile length, and sampling spacing. In a simulation study, Oglivly and Foster determined that, to properly distinguish between exponential and Gaussian ACFs, it is necessary to digitize the profile at a sampling space of at most 0.1 of the correlation length, with a profile length of at least 60 times the correlation length [10]. In a similar, but more recent study, Oh and Kay reported that to precisely determine the RMS_h of a profile, its length had to be at least 40 times the correlation length; and for the precise determination of the correlation length, the profile should be at least 200 times the correlation length. They also determined that the sample spacing should be no longer than 0.2 times the correlation length. [34]. These rules have the disadvantage that an *a priori* knowledge of the correlation length of the surface to be digitized is required. A more practical rule from Ulaby et al. states that the sampling spacing should be smaller than 0.1 of the microwave observation wavelength [9]. In

addition, the studies presented in [10] and [34] do not consider instrumental errors that will corrupt the studied surface and will degrade the accuracy of the retrieved ACF and its respective correlation length.

In terms of adequate profile lengths, Callens et al. used roughness parameters obtained for 25-meter-long profiles from natural soils at different tillage states as reference to compare roughness parameters derived from shorter profiles. They found that for smooth surfaces the profile needed to be at least 10 meters in length to obtain comparable RMS_h values, and profiles of at least 5 meters were required for rougher surfaces. They also determined that long profiles (~ 25 m) are required to accurately estimate correlation lengths [2]. Baghdadi et al. suggested that if a surface has a correlation length between 2 and 20 cm, averaging parameter values obtained from ten 2 m profiles provides a precision of $\pm 5\%$ for RMS_h and between ± 5 to $\pm 15\%$ for correlation length. If ten 1m profiles are used, precision will be reduced to $\pm 10\%$ for RMS_h and $\pm 20\%$ for correlation length. [24]

It has also been found that a large range of roughness parameter values can be obtained from the same surface using different techniques. There have been several attempts to compare the roughness parameters derived from different methodologies with results that have been contradictory or inconclusive. One of the first was by Gatti et al. who compared mechanical and laser profilers. They found that after averaging metrics derived from five to eight profiles, the results between mechanical and LASER profilers agreed to within 20% [33]. Mattia et al. compared roughness metrics obtained from profiles derived from a meshboard, a pin profiler, and a LASER profiler. They found relatively good agreement between the correlation lengths obtained from the

LASER profiler and pin profiler data. The RMS_h obtained from the pin profiler is generally overestimated in comparison with the ones obtained from the LASER profiler. Finally, they found that values for the correlation length and RMS obtained from the meshboard data contained significant systematic errors with respect to the ones obtained from the laser profiler data. They attribute this to errors that occur during the digitization process [13]. Bryant et al. performed a study in which they compared pin profiler and ground-based LiDAR scanner RMS_h results. By digitizing what they assumed to be a smooth surface, with RMS_h = 0, they determined that each method presents a characteristic positive bias of 1.5 mm and 3 mm respectively. When these biases were removed, the RMS_h derived from the two methods had an R² of 0.6 [15]. While these studies compared roughness metrics obtained from different methods, an accuracy assessment with respect to a known reference surface for each method remains to be done [15].

This chapter presents several analyses that were performed to assess the accuracy and precision of roughness parameters derived from ground-based LiDAR measurements. The first analysis consisted on characterizing the instrument random noise present in 2D elevation profiles extracted from flat surfaces. Based on this characterized instrument noise, the second analysis was performed. This consisted of generating 2D profiles with different roughness characteristics and corrupting them with characteristic instrument noise. The effect that the random noise had on the accuracy of the derived roughness parameters was then quantified. The third analysis consisted of performing an accuracy assessment of the derived RMS_h from real measurements using roughness references. Finally, as a validation of the accuracy assessments, a

comparison was conducted between the roughness parameters obtained from meshboard and LiDAR for a sample of 21 profiles of bare agricultural surfaces.

Characterization of Ground-based LiDAR Errors

The ground based-LiDAR employed in this study is an Optech ILRIS-3D scanner (shown in Figure 1-7). The ILRIS is an instrument composed by a time-of-flight LiDAR and a two-axis scanner. A full description of the instrument design, operation, and performance can be found in [19]. To characterize the instrument random error, seven smooth flat surfaces were scanned. Figure 2-1 A) shows a picture of one such reference surface, a smooth metal plate resting on a flat floor. Figure 2-1 B) shows a rendering from the LiDAR scanned point cloud. The points from the area corresponding to the metal plate were then cropped and gridded at 5 mm spacing, creating a 3D digital elevation model (DEM) shown in Figure 2-2. From the DEM, 2D transects were extracted along the row direction. For each point of the transect, the height deviation from the flat surface was determined. Figure 2-3 shows a plot of the height deviations resulting from concatenating all the profiles. Figure 2-4 A) shows a histogram of the deviations, while Figure 2-4 B) shows the logarithm of the power spectral density resultant from applying an FFT to the height deviation sequence of Figure 2-3. From Figure 2-4, it can be observed that the magnitude of LiDAR random error follows a Gaussian distribution and its spectrum is almost uniform for all frequency components. This same process was applied to the other six reference flat surfaces. A total of 848 profiles were extracted, containing 2,012,304 elevation measurements. From these it was found that when extracting 2D profiles, the LiDAR random error can be modeled as Gaussian white noise with a standard deviation of 2.8 mm. This is consistent with the modeling accuracy quoted by the manufacturer.

Accuracy Assessment Based on Synthetic Generated Profiles

To perform the first accuracy assessment of the derived roughness parameter values, a computer simulation approach was followed. First, a moving average method was used to generate 2D profiles with Gaussian and exponential ACFs for five different values of RMS_h (5 mm, 1, 1.5, 2, and 2.5 cm) and correlation length (2, 8, 14, 20, and 26 cm). A total of 50 unique profiles, 50 meters in length with a sampling spacing of 1 mm were generated. These 50 profiles were corrupted by adding random characteristic noise from the LiDAR (white noise with a standard deviation of 2.8 mm). The original and corrupted profiles were then cut into ten 5 meter segments. The corrupted profiles were also resampled at 5 and 10 mm. From the original and the corrupted profiles, the RMS_h, correlation length, and the fit metrics for the different theoretical ACF were computed. The accuracy assessment was performed by comparing the roughness parameter values of the original and corrupted profiles.

To generate the random height component sequences with a given RMS_h, correlation length, and ACF, the moving average method described in [10], [32], [34] was followed. The purpose is to generate a sequence representing random component height variations of the following form:

$$z_i = h(x_i) = h(i\Delta x), \quad (2-1)$$

where i is the sample index and Δx is the sample separation or discretization interval. The first step is to generate a sequence V_i of $2N+1$ uncorrelated random numbers from a standard normal distribution with a zero mean and a standard deviation of 1 (Figure 2-5). It is also necessary to generate a sequence of weights W_i each with a length of $2M+1$ (Figure 2-6). These weights are defined depending on the type of

autocorrelation function, the required RMSh (σ_h), and correlation length (l). For the Gaussian ACF the weight sequence is given by:

$$W_G(i) = \sqrt{\frac{2\Delta x}{\sqrt{\pi}l}} \times \sigma_h \times e^{-2\left(\frac{i\Delta x}{l}\right)^2}. \quad (2-2)$$

The weight sequence for the exponential ACF is given by:

$$W_e(i) = \frac{\sqrt{2\Delta x}}{\pi\sqrt{l}} \times \sigma_h \times K_0\left(\frac{i\Delta x}{l}\right), \quad (2-3)$$

where K_0 is the modified Bessel function of the second kind. The moving average method is then applied to obtain the correlated sequence as:

$$z_i = \sum_{j=-M}^M W_j \times V_{j+i}. \quad (2-4)$$

The resulting correlated sequences are of length $2(N-M)+1$, as shown in Figures 2-7 and 2-8.

Accuracy of Derived Autocorrelation Function (ACF)

To characterize an autocorrelation function two parameters are required: the exponent of the generalized power law (Equation 1-10) and its correlation length. To obtain the value of the exponent from a measured ACF, an iterative linearized least squares method must be employed. The linearized least squares model for Equation 1-10 is:

$$\begin{bmatrix} -e^{-\left(\frac{|h_1|}{l}\right)^{n_0}} \times \left(\frac{|h_1|}{l}\right)^{n_0} \times \ln\left(\frac{|h_1|}{l}\right)^{n_0} \\ \vdots \\ -e^{-\left(\frac{|h_m|}{l}\right)^{n_0}} \times \left(\frac{|h_m|}{l}\right)^{n_0} \times \ln\left(\frac{|h_m|}{l}\right)^{n_0} \end{bmatrix} \times \partial n = \begin{bmatrix} \rho(h_1) - e^{-\left(\frac{|h_1|}{l}\right)^{n_0}} + v_1 \\ \vdots \\ \rho(h_m) - e^{-\left(\frac{|h_m|}{l}\right)^{n_0}} + v_m \end{bmatrix}, \quad (2-5)$$

where l is the determined correlation length, n_0 is the exponent value estimate for the current iteration, $\hat{\partial}n$ is the correction to the estimated value of the exponent that needs to be determined, h_m is the m th observed lag, $\rho(h_m)$ is the value of the measured autocorrelation function for the h_m lag, and v_m are the residuals to be minimized.

Table 2-1 presents the change in the exponent of the generalized power law (Equation 1-10) of the original ACF due to instrument-induced noise. The results indicate that the effect of the instrument noise is a reduction in the exponent value. This means that a profile with a Gaussian ACF will look more like one with an exponential ACF. This effect is particularly noticeable for smooth profiles characterized by small RMS_h and large correlation lengths. For instance, original profiles with RMS_h in the order of 5 mm, the exponent of the generalized power law ACF from the corrupted profiles will be less than 1. Original profiles with Gaussian ACFs will be more affected than those that follow exponential ACFs.

Accuracy of Derived of Random Height Root Mean Square (RMS_h)

Table 2-2 summarizes the root mean square error (RMSE) in the estimation of the RMS_h for original profiles with exponential and Gaussian ACFs. The following is the interpretation of those results:

- For profiles with a true RMS_h much higher than the noise level of the instrument (RMS_h >1 cm), the estimated RMS_h is accurate to approximately 1 mm.
- For profiles with a true RMS_h about three times the noise level of the instrument (RMS_h ~1 cm), the estimated RMS_h is accurate to approximately 1 mm for Gaussian ACF and 2mm for exponential ACF.
- For profiles with a true RMS_h about double the noise level of the instrument (RMS_h <5 mm), the estimated RMS_h is accurate to approximately 2-3 mm for Gaussian ACF and 3 mm for exponential ACF.

For profiles with ACF resembling the Gaussian model, the estimation of RMS_h is less affected by the noise corruption than their exponential counterparts.

Accuracy of Derived Correlation Lengths

Table 2-3 summarizes the root mean square error (RMSE) in the estimation of the correlation lengths for original profiles with exponential and Gaussian ACFs. The net effect of instrument random noise is a reduction in the measured correlation length values with respect to the true value. Table 2-4 gives the average reduction of the measured correlation lengths for the different combinations of RMS_h, correlation lengths, and ACFs. The larger differences occur for those surfaces with low RMS_h and long correlation lengths; exponential surfaces are more affected than those with Gaussian ACFs. The accuracy of the derived correlation lengths of exponential surfaces is degraded on average by a factor of two compared to the surfaces characterized by Gaussian ACFs. The least accurate results of derived correlation lengths are obtained from those surfaces with low RMS_h and long correlation lengths that have an RMSE of 15 to 25 cm. For surfaces with Gaussian ACF, RMS_h higher than 1 cm and correlation lengths lower than 20 cm, the accuracy of instrument-derived correlation lengths is within 2 cm. The accuracy of derived correlation lengths for surfaces with exponential and similar characteristics is within 4 cm.

Accuracy Assessment Based on Roughness References

The second accuracy assessment was based on real measurements conducted under laboratory conditions. To perform this evaluation, a set of references with known roughness characteristics was constructed from square wooden pegs of 0.96 cm with variable heights. The pegs were mounted on two 1.22 m aluminum U-rails, yielding a single 2.44m long reference with 254 height values. These references provide a

spectral sampling of 0.04 wavelengths for L-band to 0.17 for C-band. By using different height pegs in a pseudorandom sequence, uncorrelated height profiles were generated with RMS_h values of 0.9, 2, 3, and 3.8 cm. Figure 2-9 shows a section of one of such uncorrelated roughness reference. Correlated sequences with a generalized power law spectrum ACF ($n \sim 1.5$) were also produced with RMS_h values of 0, 0.9, 1.6, 2.7, and 3.7 cm. See Figure 2-10 for a roughness reference with a correlated height sequence.

A total of 28 reference profiles (2.44 m in length), 16 pseudorandom and 12 correlated, were digitized using the meshboard and the ground-based LiDAR. Meshboard data were collected and processed using the procedure described in Appendix B. Using the LiDAR, the references were scanned from an oblique view at a range of 8–9 m and with a sample spacing of 3–4 mm (Figure 2-11). The resulting point cloud was rectified and transformed into a regularly spaced 9.6 mm grid to match the spacing of the reference pegs. The final meshboard digitized profile and the LiDAR-derived grids were analyzed using a script that extracts the study profile, detrends them to obtain the random height component, and computes the roughness parameters. The correlation coefficient and coefficient of determination (R^2) between the observed height profiles with respect to reference profile were computed as measures of how well the instrument reproduced the reference target (i.e., digitization fidelity). Figure 2-12 is a graphic representation of the three different data sources that are loaded onto the Matlab script that performs the accuracy assessment. Figure 2-13 shows a comparison of the height random component from the reference and those extracted from meshboard and LiDAR data, and from which the roughness parameters are computed. The individual results for each of the 28 tests performed for the accuracy

assessment are presented in Table 2-5, while the overall results are summarized in Table 2-6.

Digitization Fidelity of the Instruments

Two metrics were employed to quantify how well the instruments record the height variations of the study surface, the correlation coefficient and the coefficient of determination (R^2). These are defined as

$$\rho_{x,y} = \frac{Cov(o, r)}{\sigma_o \sigma_r} = \frac{\sum_{i=1}^n (o_i - \bar{o})(r_i - \bar{r})}{\sigma_o \sigma_r}, \quad (2-6)$$

$$R^2 = 1 - \frac{\sum_{i=1}^n (o_i - r_i)^2}{\sum_{i=1}^n (o_i - \bar{o})^2} = 1 - \frac{\sum_{i=1}^n (o_i - r_i)^2}{n \times \sigma_o^2}, \quad (2-7)$$

where o_i is the i^{th} height observation point from the meshboard or LiDAR data and r_i is the respective height according to the reference.

The data show that the meshboard records the surface height variations with great fidelity for both uncorrelated and correlated profiles with correlation coefficients exceeding 0.96 and R^2 exceeding 0.92. The LiDAR scanner has less fidelity than the meshboard, especially with uncorrelated height sequences for which it shows poor performance with R^2 between 0.44-0.77. This is due mainly to the higher noise level injected by the LiDAR and because a rough uncorrelated surface will have rapid height variations. These variations cause effects such as multipathing, shadowing, and ringing that affect the LiDAR performance. However, for correlated surfaces, which is the case of most natural soils, the scanner performs well with correlation coefficients greater than 0.94 and R^2 greater than 0.87.

Accuracy of Derived RMS_h

Results of RMS_h accuracy assessment are illustrated in Figure 2-14. It was found that the RMS_h obtained from the meshboard match the reference RMS_h to within 1 mm, independent of the surface RMS_h for both uncorrelated and correlated surfaces. The RMSE for meshboard-derived RMS_h of correlated surfaces ($n = 12$) was 1.1 mm and 0.9 mm overall ($n = 28$). In previous studies by [13] and [33] data from a laser profiler were used as a benchmark to compare meshboard-derived roughness parameters and not even a close agreement was achieved. This improvement can be attributed to the proper removal of the systematic errors caused by image distortion as described in Appendix B. The results of the accuracy of the RMS_h values obtained from the LiDAR are different for uncorrelated and correlated surfaces. For uncorrelated surfaces, the RMS_h is underestimated with respect to the reference and as the roughness of the surface increases the underestimation also increases. This is due to the multipath, shadowing, and ringing effects that tend to smooth the digitized surface. With respect to correlated surfaces, the experiments show that for a uniform flat surface, the LiDAR overestimates the RMS_h by 4 mm, which is consistent with the results obtained in [15]. However, in their work they assumed that this was a positive bias present in all LiDAR derived RMS_h values. In contrast, results from this experiment show that the RMS_h values derived from LiDAR are positively biased only in the range between 0 to 9 mm, unbiased for surfaces with RMS_h between 1 to 2 cm, and for surfaces with RMS_h between 2 and 4 cm are underestimated by only 1 mm. RMSE for LiDAR-derived RMS_h of correlated surfaces was found to be 2.5 mm.

Validation with Agricultural Soil Measurements

As a final validation of the accuracy assessments, a comparison of roughness parameter values was performed. For this, 21 profiles of agricultural soils with different roughness characteristics were obtained each with a length of 2.13 m. Data collection was performed simultaneously with the LiDAR scanner and meshboard as shown in Figure 2-15. In addition to the comparison, it was determined how well the measured soil surface ACF matched the Gaussian or exponential models. For this purpose, the exponent of the power spectrum law was determined for each experimentally determined autocorrelation function. Also the coefficient of determination (R^2) was computed between the measured ACF and each of the theoretical models for two different intervals, one considering the entire lag range from 0 to the maximum lag and another just considering the lag range from 0 to the correlation length. The individual results for the 21 comparison of roughness parameters values are presented in Table 2-7 and summarized in Table 2-8.

Comparison of RMS_h Values

The comparison of the derived values for RMS_h is illustrated in Figure 2-16. A very good agreement was found between the values estimated by the two methods with an R^2 of 0.947, which was much better than the 0.6 obtained in [15] for the Arizona set and the no agreement reported in [13] and [33]. This is also in agreement with the results of the accuracy assessments performed with synthetic profiles and roughness references.

Comparison of Correlation Lengths

The agreement between the derived correlation lengths was weak, with a correlation coefficient of only 0.50 and an R^2 of 0.25. Figure 2-17 shows the difference in the derived correlation lengths. Where the solid dots represent the LiDAR-derived

RMS_h and correlation length, the tip of the horizontal error bar corresponds to the correlation length obtained from the meshboard. As can be seen, the largest differences occur for RMS_h values below 1.5 cm. This was predicted from the accuracy assessment based on synthetically generated profiles, where it was demonstrated that is extremely difficult to obtain accurate values of correlation lengths from smooth surfaces due to the corruption of the autocorrelation function from the instrument-generated noise. In addition, these differences can be attributed to the modification of the surface profile by the meshboard and the inherently large statistical variation of correlation length values. Despite the low correlation, it is worth noticing that 81% of the absolute differences in the derived correlation lengths were below 5 cm, and 52% below 2 cm. Also, good agreements of the derived correlation length have not been reported before.

Autocorrelation Functions of Agricultural Soils

With regard to the ACF model that best describes natural soils, it was found that the averaged exponent of a power law spectrum was 1.47 for the meshboard and 1.23 for the LiDAR. This result is also expected from the previous results of the accuracy assessment based on the synthetic profiles. Because the LiDAR has a higher noise level than the meshboard, the derived ACF from LiDAR will be closer to the exponential ACF model with an exponent value of 1. In terms of the R^2 comparing the measured ACF with the theoretical models; if only the lag range from zero to the correlation length is considered, the exponential model is marginally better than the Gaussian. However, if the entire lag range is considered, the Gaussian model is a marginally better fit than the exponential.

Chapter Conclusions

From the analyses presented in this chapter, it can be concluded that the main issue affecting the precision and accuracy of the derived roughness parameters is not properly considering the effects of the instrumental systematic and random errors. Surface heights and roughness are random processes. When digitizing the surface with any instrument, the instrument random errors are mixed with the random surface heights. Thus, what is obtained from the instrument measurements is the addition of two random processes. To properly retrieve the roughness parameters, the instrument's systematic errors must be removed and the random errors properly characterized. When the random errors are properly characterized, their effects on the surface measurements can be quantified and accurate estimates of the parameters can be obtained. Of the roughness parameters, the RMS_h is the least sensitive to instrument noise. The measured RMS_h value will asymptotically approximate the true value as the instrument characteristic noise is much smaller than the surface RMS_h. For surfaces with RMS_h comparable to the instrument noise, the measured RMS_h can be corrected by:

$$RMS_{h_{est}} = \sqrt{RMS_{h_{meas}}^2 - \sigma_{inst}^2}, \quad (2-8)$$

where $RMS_{h_{est}}$ is the estimated value, $RMS_{h_{meas}}$ is the measured value and σ_{inst}^2 is the instrument characterized noise variance.

To accurately determine the correlation length it is necessary to properly retrieve the autocorrelation function. The measured autocorrelation function is the ACF resulting from the addition of two random processes. In theory, instrument random noise is usually Gaussian white noise. This means that the instrument random errors have no

correlation length. In practice, the correlation length is non-zero but relatively small. The effect of the instrument noise on the retrieved ACF is a reduction of the value of the exponent of the generalized power law (Equation 1-10) and a reduction of the correlation length. The magnitude of the reductions is proportional to the relative size of the instrument's noise standard deviation and correlation length with respect to the random height's variation RMS_h and correlation length. The closer the instrument noise level is to the surface RMS_h, the greater the reduction of exponent and correlation length values.

It was also determined that due to its lower noise level, under laboratory conditions the meshboard has a higher digitization fidelity than the LiDAR. However, under field conditions, this performance is not achievable because the meshboard unavoidably disturbs the surface under study. Beside its destructive nature, an additional disadvantage of the meshboard method is that it is very time consuming. When the errors from the ground-based LiDAR are properly accounted for, it is possible to derive RMS_h values accurate to 1 mm and correlation length values accurate to less than 1 cm from its data.

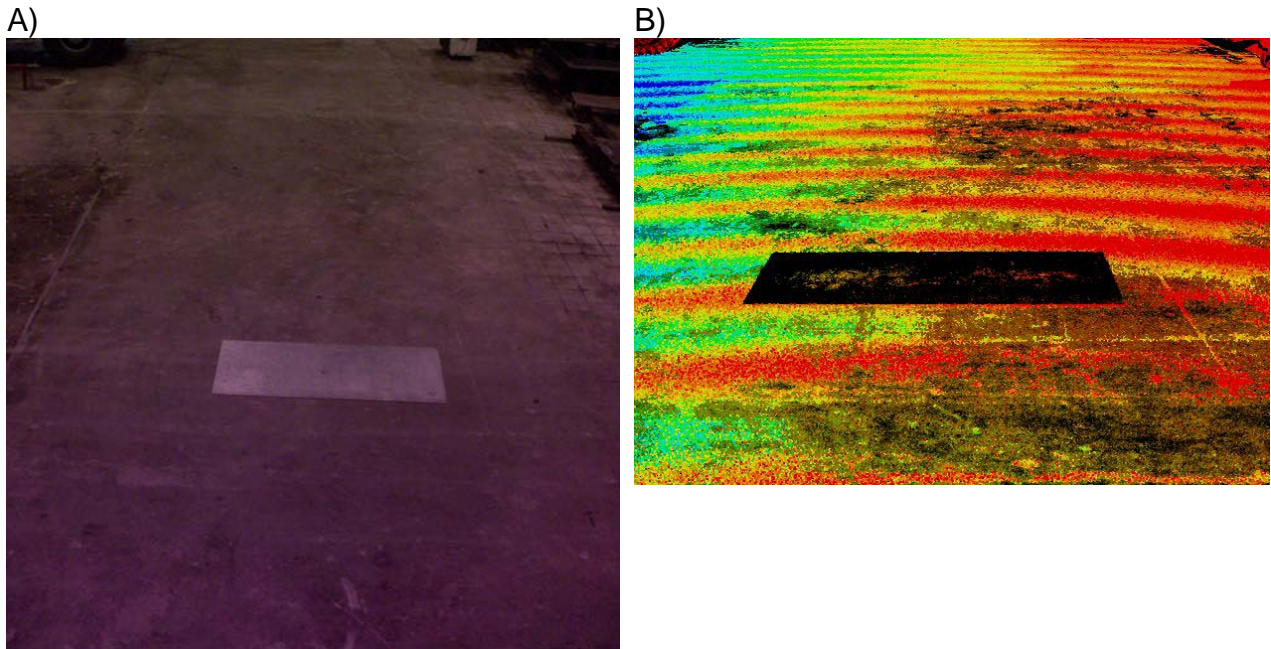


Figure 2-1. Test to characterize of LiDAR random noise. A) Photo of a smooth flat target. B) Rendering from the LiDAR scanned point cloud.

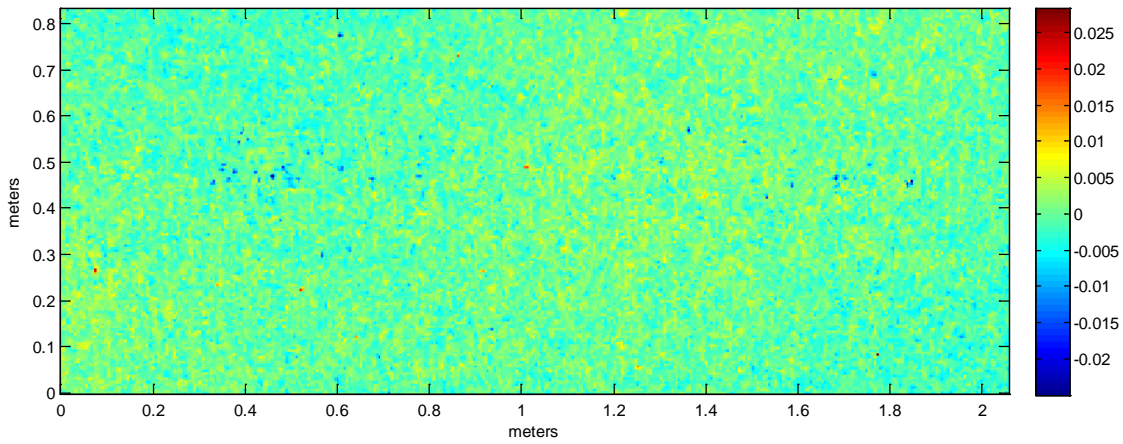


Figure 2-2. DEM derived from a LiDAR scan of a smooth flat target.

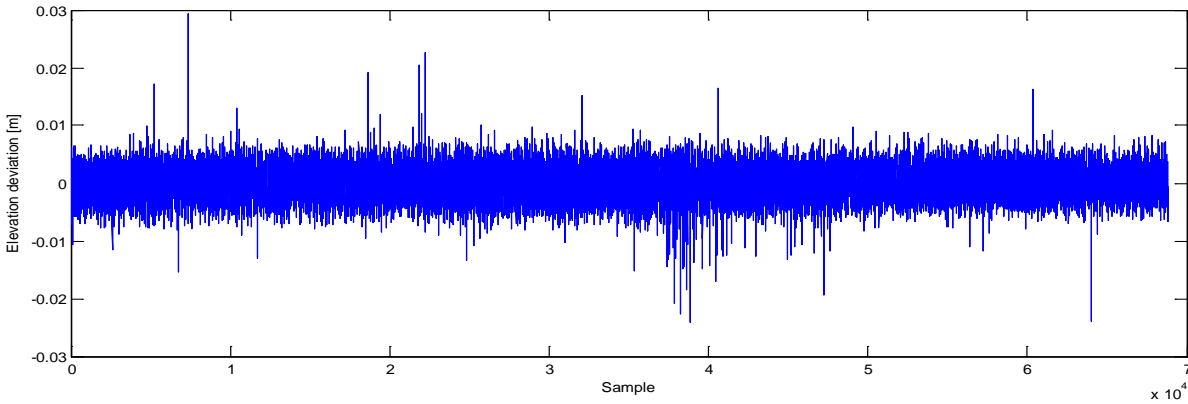


Figure 2-3. Elevation deviations from the smooth surface, extracting and concatenating profiles along the row direction of the DEM.

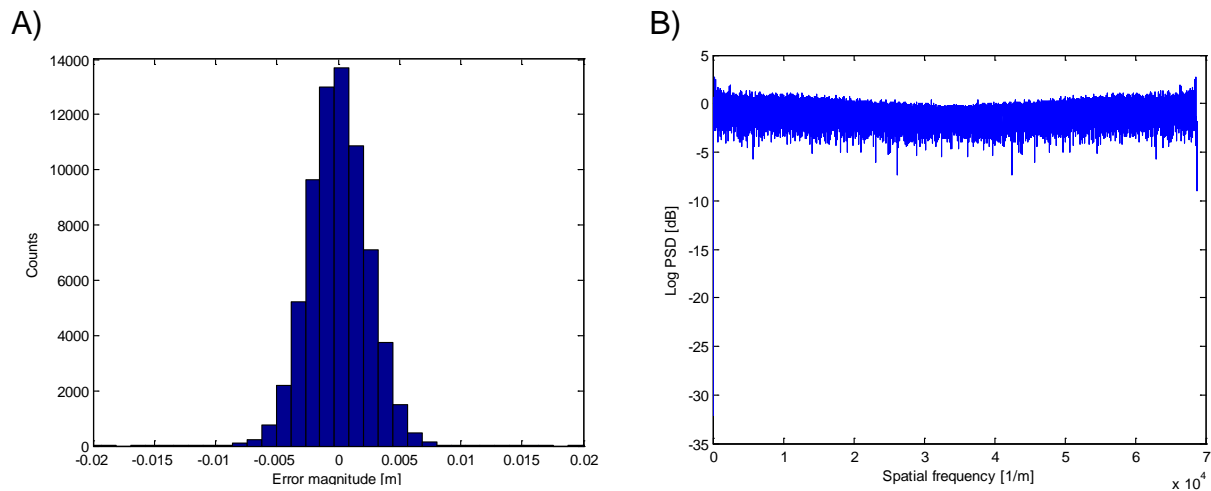


Figure 2-4. Characterization of ground-based LiDAR random errors. A) Distribution of magnitudes. B) Power spectral density.

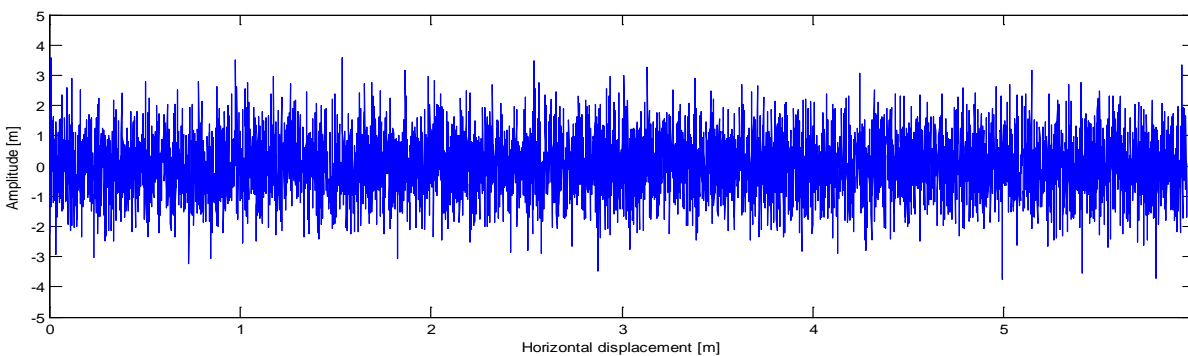


Figure 2-5. Random seed sequence from which correlated sequences are generated.

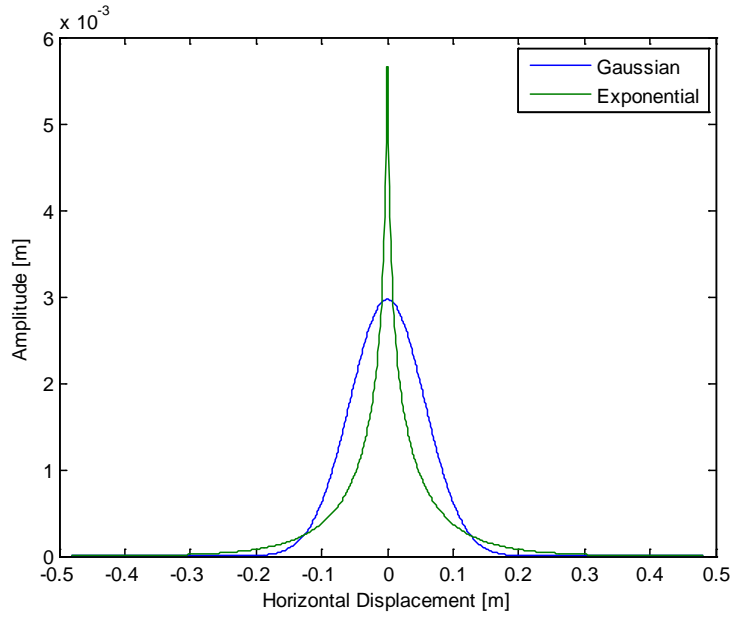


Figure 2-6. Gaussian and exponential weighting functions used in the moving average method.

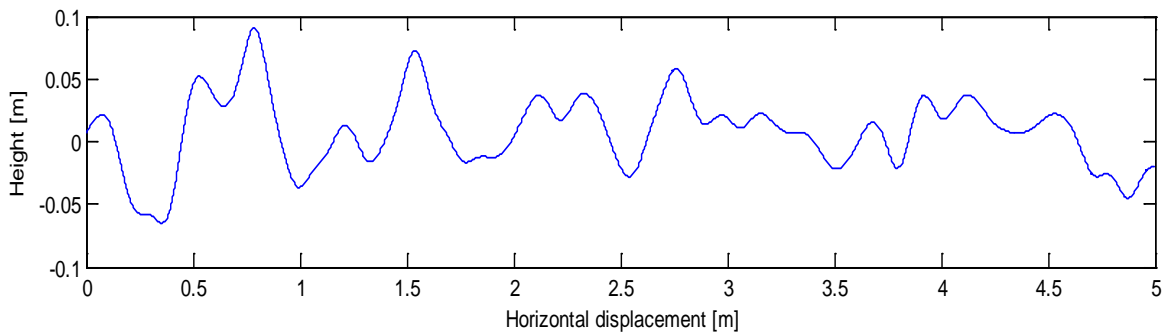


Figure 2-7. Generated profile with a Gaussian ACF.

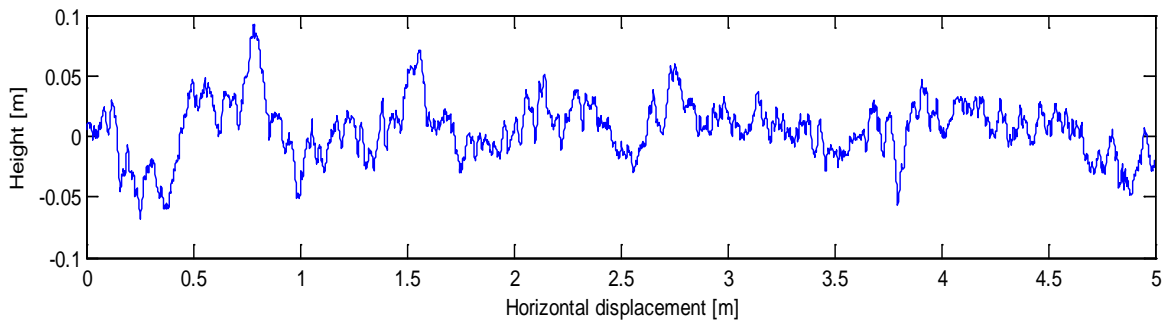


Figure 2-8. Generated profile with an exponential ACF.

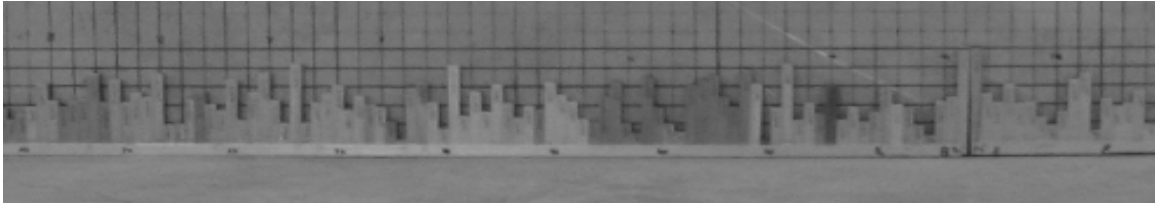


Figure 2-9. Section of a pseudorandom roughness reference with an RMS_h of 2 cm.



Figure 2-10. Section of a correlated roughness reference with an RMS_h of 2.7 cm.



Figure 2-11. Scanning geometry of roughness references using ground-based LiDAR.

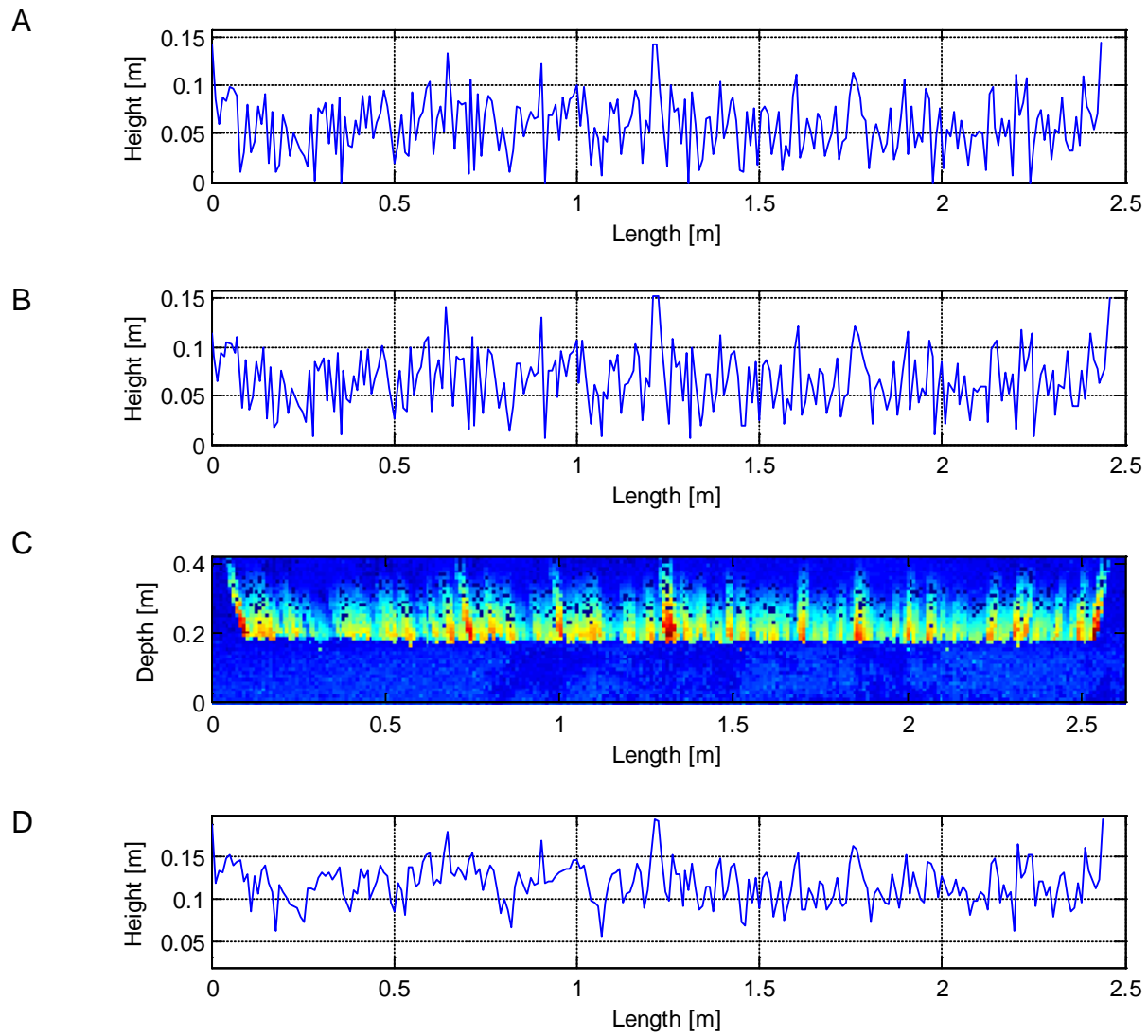


Figure 2-12. Inputs into the Matlab script used to perform the accuracy assessment based on roughness references.

A) The roughness reference profile. B) Measured profile using the meshboard. C) 3D grid derived from the ground-based LiDAR. D) Extracted profile from the 3D grid.

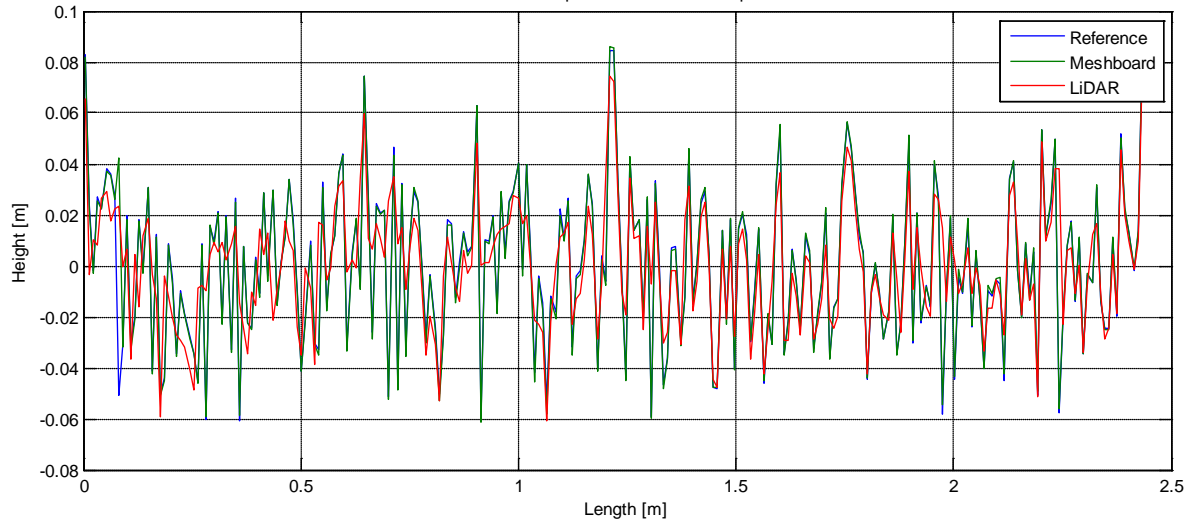


Figure 2-13. Random component extracted from the reference, the meshboard, and LiDAR-derived profiles.

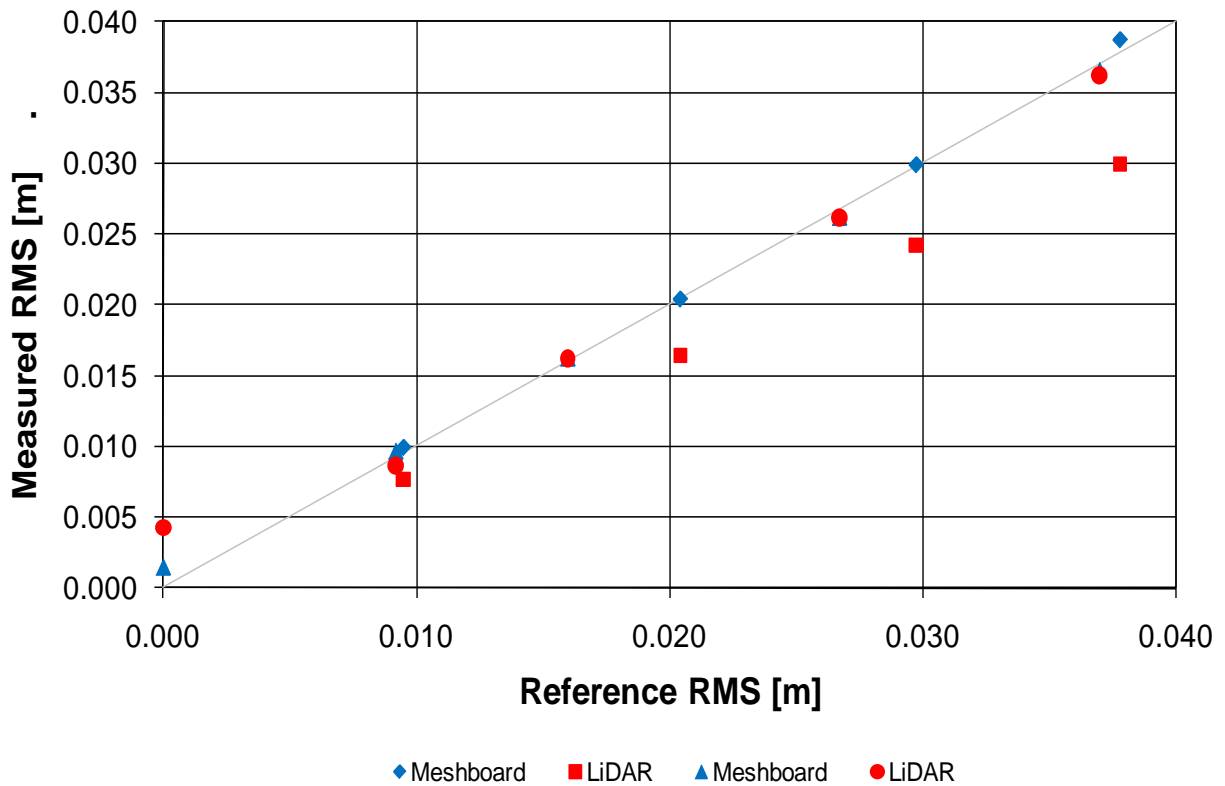


Figure 2-14. Results of the RMS accuracy assessment.

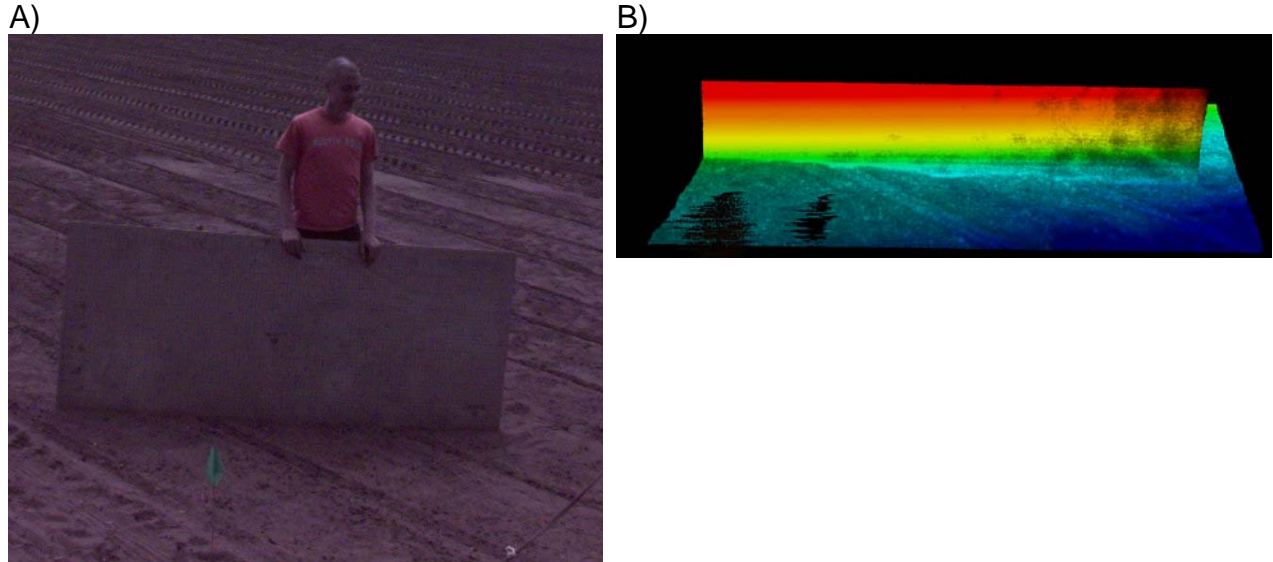


Figure 2-15. Simultaneous profile digitizing with A) meshboard and B) LiDAR.

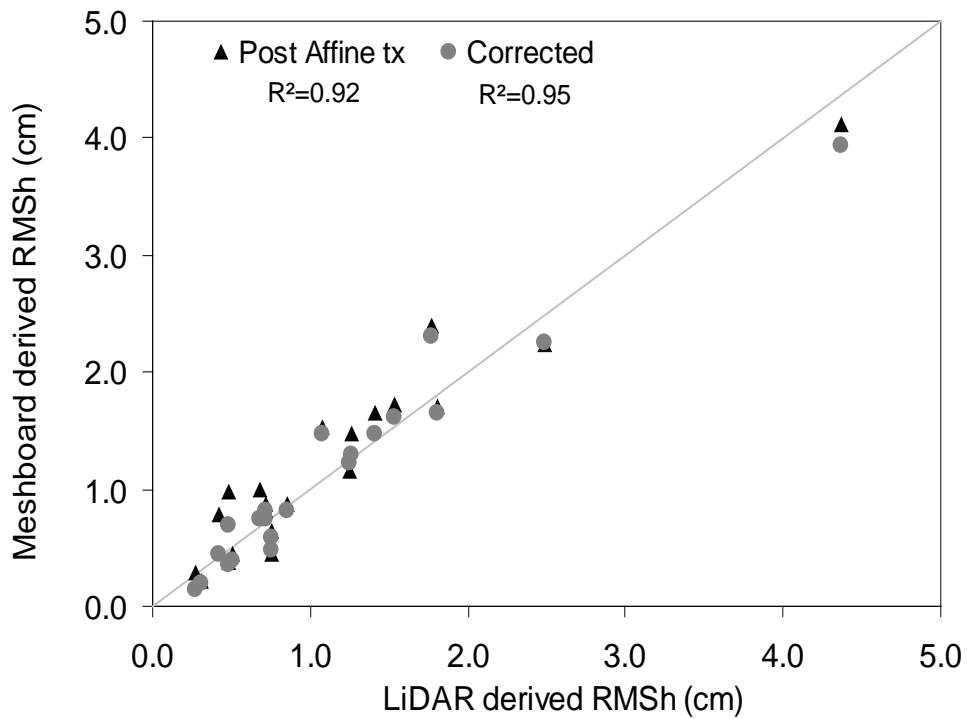


Figure 2-16. Comparison of RMSh values of bare agricultural soils obtained from meshboard and LiDAR.

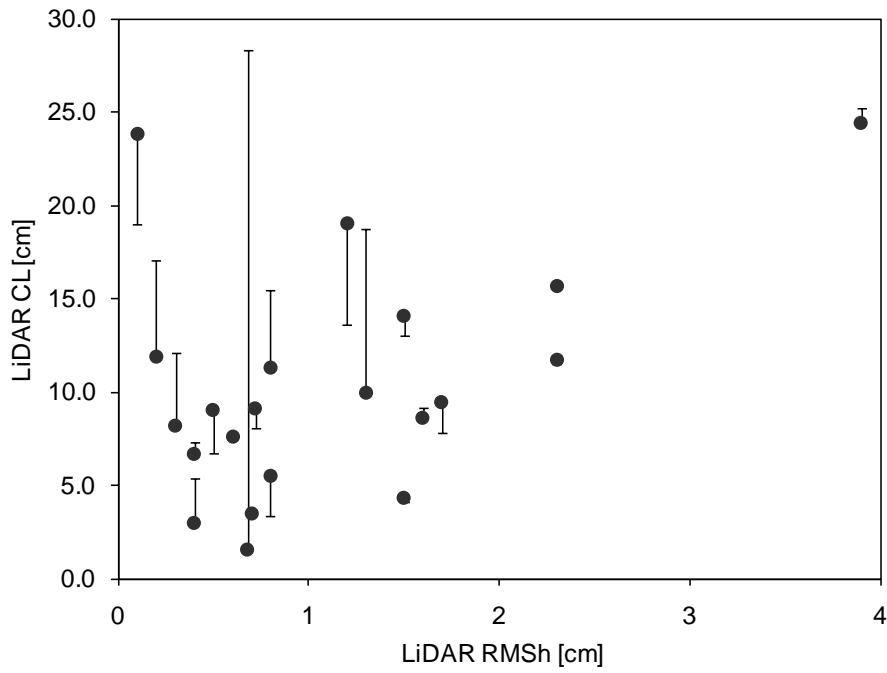


Figure 2-17. Difference between meshboard and LiDAR-derived correlation lengths of bare agricultural soils.

Solid dots represent the LiDAR-derived RMSH and correlation length, the tip of the error bar corresponds to the correlation length obtained from the meshboard.

Table 2-1. Mean difference in the exponent of generalized power law for profiles with exponential and Gaussian ACF.

| Correlation length (cm) | Exponential ACF | | | | | Gaussian ACF | | | | | |
|-------------------------|---------------------|-------|-------|-------|-------|--------------------|-------|-------|-------|-------|--|
| | Reference RMSh(cm) | | | | | Reference RMSh(cm) | | | | | |
| | 0.5 | 1 | 1.5 | 2.0 | 2.5 | 0.5 | 1 | 1.5 | 2.0 | 2.5 | |
| | Sampled every 1 mm | | | | | | | | | | |
| 2 | -0.71 | -0.25 | -0.10 | -0.06 | -0.04 | -1.06 | -0.35 | -0.13 | -0.08 | -0.06 | |
| 8 | -0.58 | -0.20 | -0.09 | -0.05 | -0.03 | -1.05 | -0.32 | -0.14 | -0.10 | -0.05 | |
| 14 | -0.60 | -0.19 | -0.11 | -0.06 | -0.04 | -1.01 | -0.38 | -0.20 | -0.13 | -0.06 | |
| 20 | -0.65 | -0.26 | -0.10 | -0.06 | -0.03 | -1.10 | -0.40 | -0.17 | -0.07 | -0.05 | |
| 26 | -0.68 | -0.22 | -0.05 | -0.06 | -0.05 | -1.11 | -0.39 | -0.15 | -0.07 | -0.07 | |
| | Sampled every 5 mm | | | | | | | | | | |
| 2 | -0.55 | -0.23 | -0.09 | -0.07 | -0.07 | -0.93 | -0.30 | -0.14 | -0.07 | -0.04 | |
| 8 | -0.55 | -0.18 | -0.07 | -0.05 | -0.03 | -1.04 | -0.31 | -0.14 | -0.10 | -0.05 | |
| 14 | -0.58 | -0.18 | -0.11 | -0.06 | -0.04 | -1.00 | -0.38 | -0.20 | -0.12 | -0.06 | |
| 20 | -0.62 | -0.27 | -0.11 | -0.06 | -0.04 | -1.10 | -0.41 | -0.18 | -0.07 | -0.05 | |
| 26 | -0.67 | -0.23 | -0.06 | -0.05 | -0.05 | -1.11 | -0.38 | -0.15 | -0.07 | -0.07 | |
| | Sampled every 10 mm | | | | | | | | | | |
| 2 | -0.41 | -0.14 | -0.13 | -0.08 | -0.07 | -0.69 | -0.19 | -0.17 | -0.02 | 0.01 | |
| 8 | -0.50 | -0.17 | -0.08 | -0.04 | -0.02 | -1.03 | -0.29 | -0.13 | -0.09 | -0.05 | |
| 14 | -0.55 | -0.16 | -0.10 | -0.07 | -0.03 | -0.99 | -0.38 | -0.20 | -0.13 | -0.05 | |
| 20 | -0.60 | -0.26 | -0.11 | -0.06 | -0.04 | -1.07 | -0.39 | -0.18 | -0.07 | -0.05 | |
| 26 | -0.65 | -0.23 | -0.05 | -0.05 | -0.05 | -1.12 | -0.39 | -0.15 | -0.08 | -0.07 | |

Table 2-2. RMSE (cm) in the estimation of RMS_h for profiles with exponential ACF.

| Correlation length (cm) | Exponential ACF | | | | | Gaussian ACF | | | | |
|-------------------------|---------------------------------|-----|-----|-----|-----|---------------------------------|-----|-----|-----|-----|
| | Reference RMS _h (cm) | | | | | Reference RMS _h (cm) | | | | |
| | 0.5 | 1 | 1.5 | 2.0 | 2.5 | 0.5 | 1 | 1.5 | 2.0 | 2.5 |
| | Sampled every 1 mm | | | | | | | | | |
| 2 | 0.3 | 0.2 | 0.1 | 0.1 | 0.1 | 0.2 | 0.1 | 0.1 | 0.1 | 0.0 |
| 8 | 0.3 | 0.1 | 0.1 | 0.1 | 0.1 | 0.2 | 0.1 | 0.1 | 0.1 | 0.1 |
| 14 | 0.3 | 0.1 | 0.1 | 0.1 | 0.1 | 0.2 | 0.1 | 0.1 | 0.1 | 0.1 |
| 20 | 0.3 | 0.2 | 0.1 | 0.1 | 0.1 | 0.3 | 0.1 | 0.1 | 0.1 | 0.1 |
| 26 | 0.3 | 0.2 | 0.1 | 0.1 | 0.1 | 0.3 | 0.1 | 0.1 | 0.1 | 0.1 |
| | Sampled every 5 mm | | | | | | | | | |
| 2 | 0.3 | 0.2 | 0.1 | 0.1 | 0.0 | 0.2 | 0.1 | 0.1 | 0.1 | 0.0 |
| 8 | 0.3 | 0.1 | 0.1 | 0.1 | 0.1 | 0.2 | 0.1 | 0.1 | 0.1 | 0.1 |
| 14 | 0.3 | 0.2 | 0.1 | 0.1 | 0.1 | 0.2 | 0.1 | 0.1 | 0.1 | 0.0 |
| 20 | 0.3 | 0.1 | 0.1 | 0.1 | 0.1 | 0.3 | 0.1 | 0.1 | 0.1 | 0.1 |
| 26 | 0.3 | 0.1 | 0.1 | 0.1 | 0.1 | 0.2 | 0.1 | 0.1 | 0.1 | 0.0 |
| | Sampled every 10 mm | | | | | | | | | |
| 2 | 0.3 | 0.2 | 0.1 | 0.1 | 0.0 | 0.2 | 0.1 | 0.1 | 0.1 | 0.0 |
| 8 | 0.3 | 0.1 | 0.1 | 0.1 | 0.1 | 0.2 | 0.1 | 0.1 | 0.1 | 0.1 |
| 14 | 0.3 | 0.1 | 0.1 | 0.1 | 0.1 | 0.2 | 0.1 | 0.1 | 0.1 | 0.0 |
| 20 | 0.3 | 0.1 | 0.1 | 0.1 | 0.1 | 0.3 | 0.1 | 0.1 | 0.1 | 0.1 |
| 26 | 0.3 | 0.2 | 0.1 | 0.1 | 0.1 | 0.2 | 0.1 | 0.1 | 0.1 | 0.0 |

Table 2-3. RMSE (cm) in the estimation of correlation length for profiles with exponential and Gaussian ACF.

| Correlation length (cm) | Exponential ACF | | | | | Gaussian ACF | | | | |
|-------------------------|---------------------|-----|------|-----|-----|--------------------|-----|-----|-----|-----|
| | Reference RMSH(cm) | | | | | Reference RMSH(cm) | | | | |
| | 0.5 | 1 | 1.5 | 2.0 | 2.5 | 0.5 | 1 | 1.5 | 2.0 | 2.5 |
| | Sampled every 1 mm | | | | | | | | | |
| 2 | 2.3 | 0.7 | 0.4 | 0.2 | 0.1 | 1.1 | 0.3 | 0.2 | 0.1 | 0.0 |
| 8 | 9.2 | 2.5 | 2.7 | 1.7 | 0.6 | 5.7 | 1.2 | 0.9 | 0.4 | 0.2 |
| 14 | 13.4 | 6.2 | 1.7 | 1.1 | 0.7 | 7.5 | 2.0 | 0.9 | 0.7 | 0.5 |
| 20 | 18.5 | 4.1 | 2.2 | 1.2 | 0.8 | 16.8 | 3.0 | 1.4 | 1.1 | 0.4 |
| 26 | 22.2 | 7.8 | 15.3 | 1.4 | 0.6 | 15.9 | 4.8 | 1.9 | 0.8 | 0.3 |
| | Sampled every 5 mm | | | | | | | | | |
| 2 | 2.1 | 0.6 | 0.4 | 0.1 | 0.1 | 1.1 | 0.2 | 0.1 | 0.1 | 0.0 |
| 8 | 8.8 | 2.8 | 2.7 | 1.7 | 0.9 | 5.7 | 1.4 | 0.9 | 0.4 | 0.4 |
| 14 | 14.6 | 7.3 | 1.5 | 0.7 | 0.8 | 8.2 | 2.3 | 0.8 | 0.6 | 0.6 |
| 20 | 23.3 | 3.4 | 2.1 | 0.8 | 0.6 | 16.4 | 2.7 | 1.1 | 1.4 | 0.5 |
| 26 | 23.7 | 6.3 | 15.5 | 1.4 | 1.0 | 16.4 | 5.2 | 1.8 | 1.0 | 0.3 |
| | Sampled every 10 mm | | | | | | | | | |
| 2 | 2.0 | 0.4 | 0.5 | 0.1 | 0.1 | 1.1 | 0.2 | 0.1 | 0.0 | 0.0 |
| 8 | 9.7 | 2.2 | 2.1 | 2.0 | 0.8 | 6.0 | 1.3 | 0.7 | 0.4 | 0.4 |
| 14 | 15.0 | 6.9 | 1.2 | 0.5 | 1.7 | 8.8 | 2.1 | 0.7 | 0.6 | 0.7 |
| 20 | 23.5 | 2.8 | 2.8 | 1.0 | 0.4 | 16.5 | 2.1 | 1.8 | 0.9 | 0.5 |
| 26 | 24.6 | 4.9 | 14.3 | 1.1 | 0.6 | 15.0 | 4.4 | 1.1 | 0.7 | 0.1 |

Table 2-4. Mean difference (cm) of correlation lengths for profiles with exponential and Gaussian ACF.

| Correlation length (cm) | Exponential ACF | | | | | Gaussian ACF | | | | |
|-------------------------|---------------------|------|------|------|------|--------------------|------|------|------|------|
| | Reference RMSH(cm) | | | | | Reference RMSH(cm) | | | | |
| | 0.5 | 1 | 1.5 | 2.0 | 2.5 | 0.5 | 1 | 1.5 | 2.0 | 2.5 |
| | Sampled every 1 mm | | | | | | | | | |
| 2 | -0.7 | -0.2 | -0.1 | -0.1 | 0.0 | -0.4 | -0.1 | 0.0 | 0.0 | 0.0 |
| 8 | -2.9 | -0.8 | -0.8 | -0.5 | -0.2 | -1.8 | -0.4 | -0.3 | -0.1 | -0.1 |
| 14 | -4.2 | -2.0 | -0.5 | -0.4 | -0.2 | -2.4 | -0.6 | -0.3 | -0.2 | -0.2 |
| 20 | -5.8 | -1.3 | -0.7 | -0.4 | -0.2 | -5.3 | -1.0 | -0.4 | -0.3 | -0.1 |
| 26 | -7.0 | -2.5 | -4.8 | -0.4 | -0.2 | -5.0 | -1.5 | -0.6 | -0.2 | -0.1 |
| | Sampled every 5 mm | | | | | | | | | |
| 2 | -0.7 | -0.2 | -0.1 | 0.0 | 0.0 | -0.4 | -0.1 | 0.0 | 0.0 | 0.0 |
| 8 | -2.8 | -0.9 | -0.9 | -0.5 | -0.3 | -1.8 | -0.4 | -0.3 | -0.1 | -0.1 |
| 14 | -4.6 | -2.3 | -0.5 | -0.2 | -0.2 | -2.6 | -0.7 | -0.3 | -0.2 | -0.2 |
| 20 | -7.4 | -1.1 | -0.7 | -0.3 | -0.2 | -5.2 | -0.8 | -0.3 | -0.4 | -0.2 |
| 26 | -7.5 | -2.0 | -4.9 | -0.4 | -0.3 | -5.2 | -1.6 | -0.6 | -0.3 | -0.1 |
| | Sampled every 10 mm | | | | | | | | | |
| 2 | -0.6 | -0.1 | -0.1 | 0.0 | 0.0 | -0.3 | -0.1 | 0.0 | 0.0 | 0.0 |
| 8 | -3.1 | -0.7 | -0.7 | -0.6 | -0.3 | -1.9 | -0.4 | -0.2 | -0.1 | -0.1 |
| 14 | -4.7 | -2.2 | -0.4 | -0.2 | -0.5 | -2.8 | -0.7 | -0.2 | -0.2 | -0.2 |
| 20 | -7.4 | -0.9 | -0.9 | -0.3 | -0.1 | -5.2 | -0.7 | -0.6 | -0.3 | -0.2 |
| 26 | -7.8 | -1.5 | -4.5 | -0.3 | -0.2 | -4.7 | -1.4 | -0.3 | -0.2 | 0.0 |

Table 2-5. Raw results obtained from the accuracy assessment experiments.

| Dataset | Reference | | Meshboard Raw | | | | Meshboard corrected | | | | LiDAR | | | |
|----------------|------------------|---------------|------------------|---------------|----------------|---------------|---------------------|---------------|----------------|---------------|------------------|---------------|-----------------------------|---------------|
| | RMS _h | CL | RMS _h | CL | R ₂ | CC | RMS _h | CL | R ₂ | CC | std _l | CL | R ₂ _l | CC |
| 9mm_1cm_ABCD | 0.0094 | 0.0059 | 0.0109 | 0.0061 | 0.8250 | 0.9097 | 0.0107 | 0.0061 | 0.8458 | 0.9206 | 0.0072 | 0.0086 | 0.4587 | 0.8261 |
| 9mm_1cm_DCBA | 0.0094 | 0.0059 | 0.0099 | 0.0062 | 0.8810 | 0.9388 | 0.0095 | 0.0060 | 0.9075 | 0.9526 | 0.0076 | 0.0078 | 0.6614 | 0.8844 |
| 10mm_1cm_ABCD | 0.0095 | 0.0062 | 0.0102 | 0.0070 | 0.9151 | 0.9568 | 0.0096 | 0.0063 | 0.9628 | 0.9813 | 0.0076 | 0.0090 | 0.5312 | 0.8416 |
| 10mm_1cm_DCBA | 0.0095 | 0.0062 | 0.0100 | 0.0072 | 0.9149 | 0.9565 | 0.0095 | 0.0065 | 0.9676 | 0.9839 | 0.0083 | 0.0089 | 0.6044 | 0.8389 |
| Average | 0.0095 | 0.0060 | 0.0103 | 0.0066 | 0.8840 | 0.9404 | 0.0098 | 0.0062 | 0.9209 | 0.9596 | 0.0077 | 0.0086 | 0.5639 | 0.8477 |
| σ | 0.0001 | 0.0002 | 0.0005 | 0.0006 | 0.0425 | 0.0222 | 0.0006 | 0.0002 | 0.0570 | 0.0296 | 0.0004 | 0.0006 | 0.0881 | 0.0254 |
| 20mm_1cm_ABCD | 0.0204 | 0.0065 | 0.0203 | 0.0067 | 0.9698 | 0.9848 | 0.0202 | 0.0066 | 0.9803 | 0.9902 | 0.0165 | 0.0081 | 0.8030 | 0.9422 |
| 20mm_1cm_BACD | 0.0204 | 0.0065 | 0.0204 | 0.0065 | 0.9685 | 0.9842 | 0.0203 | 0.0065 | 0.9804 | 0.9903 | 0.0162 | 0.0082 | 0.7714 | 0.9358 |
| 20mm_1cm_DCBA | 0.0204 | 0.0065 | 0.0210 | 0.0068 | 0.9718 | 0.9858 | 0.0205 | 0.0067 | 0.9824 | 0.9912 | 0.0165 | 0.0081 | 0.7272 | 0.9112 |
| 20mm_1cm_CDAB | 0.0204 | 0.0065 | 0.0206 | 0.0066 | 0.9546 | 0.9771 | 0.0206 | 0.0067 | 0.9638 | 0.9818 | 0.0164 | 0.0079 | 0.7664 | 0.9300 |
| Average | 0.0204 | 0.0065 | 0.0205 | 0.0066 | 0.9662 | 0.9830 | 0.0204 | 0.0066 | 0.9767 | 0.9884 | 0.0164 | 0.0081 | 0.7670 | 0.9298 |
| σ | 0.0000 | 0.0000 | 0.0003 | 0.0001 | 0.0078 | 0.0040 | 0.0002 | 0.0001 | 0.0087 | 0.0044 | 0.0002 | 0.0002 | 0.0311 | 0.0133 |
| 30mm_1cm_ABCD | 0.0297 | 0.0061 | 0.0298 | 0.0064 | 0.9508 | 0.9752 | 0.0297 | 0.0066 | 0.9601 | 0.9800 | 0.0233 | 0.0097 | 0.3174 | 0.7615 |
| 30mm_1cm_BACD | 0.0297 | 0.0061 | 0.0298 | 0.0069 | 0.9542 | 0.9768 | 0.0300 | 0.0062 | 0.9599 | 0.9798 | 0.0226 | 0.0098 | 0.2581 | 0.7543 |
| 30mm_1cm_DCBA | 0.0297 | 0.0061 | 0.0300 | 0.0064 | 0.9491 | 0.9743 | 0.0301 | 0.0069 | 0.9605 | 0.9802 | 0.0248 | 0.0084 | 0.6197 | 0.8576 |
| 30mm_1cm_CDAB | 0.0297 | 0.0061 | 0.0302 | 0.0071 | 0.9542 | 0.9769 | 0.0302 | 0.0064 | 0.9591 | 0.9794 | 0.0262 | 0.0082 | 0.5625 | 0.8151 |
| Average | 0.0297 | 0.0061 | 0.0299 | 0.0067 | 0.9521 | 0.9758 | 0.0300 | 0.0065 | 0.9599 | 0.9798 | 0.0242 | 0.0090 | 0.4394 | 0.7971 |
| σ | 0.0000 | 0.0000 | 0.0002 | 0.0004 | 0.0025 | 0.0012 | 0.0002 | 0.0003 | 0.0006 | 0.0003 | 0.0016 | 0.0008 | 0.1783 | 0.0486 |
| 38mm_1cm_ABCD | 0.0378 | 0.0060 | 0.0392 | 0.0060 | 0.9906 | 0.9958 | 0.0387 | 0.0061 | 0.9913 | 0.9962 | 0.0284 | 0.0078 | 0.6353 | 0.9041 |
| 38mm_1cm_DCBA | 0.0378 | 0.0060 | 0.0392 | 0.0060 | 0.9866 | 0.9940 | 0.0395 | 0.0063 | 0.9874 | 0.9945 | 0.0294 | 0.0084 | 0.4580 | 0.8213 |
| 38mm_1cm_ABDC | 0.0377 | 0.0062 | 0.0377 | 0.0068 | 0.9700 | 0.9849 | 0.0384 | 0.0064 | 0.9704 | 0.9851 | 0.0308 | 0.0072 | 0.6628 | 0.8833 |
| 38mm_1cm_CDAB | 0.0377 | 0.0062 | 0.0375 | 0.0064 | 0.9917 | 0.9958 | 0.0359 | 0.0065 | 0.9929 | 0.9965 | 0.0312 | 0.0068 | 0.8146 | 0.9412 |
| Average | 0.0378 | 0.0061 | 0.0384 | 0.0063 | 0.9847 | 0.9926 | 0.0381 | 0.0063 | 0.9855 | 0.9930 | 0.0299 | 0.0075 | 0.6427 | 0.8875 |
| σ | 0.0000 | 0.0001 | 0.0010 | 0.0004 | 0.0101 | 0.0052 | 0.0016 | 0.0002 | 0.0103 | 0.0054 | 0.0013 | 0.0007 | 0.1462 | 0.0502 |

Table 2-5. Continued. Raw results obtained from the accuracy assessment experiments.

| Dataset | Reference | | Meshboard Raw | | | | Meshboard corrected | | | | LiDAR | | | |
|----------------------------|---------------|---------------|---------------|---------------|---------------|---------------|---------------------|---------------|---------------|---------------|---------------|---------------|---------------|---------------|
| | RMSH | CL | RMSH | CL | R2 | CC | RMSH | CL | R2 | CC | std_l | CL | R2_l | CC |
| 0mm_inf_A | 0.0000 | NaN | 0.0022 | 0.2718 | 0.0000 | NaN | 0.0012 | 0.2583 | 0.0000 | NaN | 0.0049 | 0.0070 | 0.0000 | NaN |
| 0mm_inf_B | 0.0000 | NaN | 0.0026 | 0.2779 | 0.0000 | NaN | 0.0015 | 0.2680 | 0.0000 | NaN | 0.0040 | 0.0068 | 0.0000 | NaN |
| 0mm_inf_C | 0.0000 | NaN | 0.0025 | 0.2543 | 0.0000 | NaN | 0.0015 | 0.2348 | 0.0000 | NaN | 0.0035 | 0.0065 | 0.0000 | NaN |
| 0mm_inf_D | 0.0000 | NaN | 0.0027 | 0.2730 | 0.0000 | NaN | 0.0017 | 0.2645 | 0.0000 | NaN | 0.0047 | 0.0079 | 0.0000 | NaN |
| Average | 0.0000 | NaN | 0.0025 | 0.2692 | 0.0000 | NaN | 0.0015 | 0.2564 | 0.0000 | NaN | 0.0043 | 0.0070 | 0.0000 | NaN |
| σ | 0.0000 | NaN | 0.0002 | 0.0103 | 0.0000 | NaN | 0.0002 | 0.0149 | 0.0000 | NaN | 0.0007 | 0.0006 | 0.0000 | NaN |
| 9mm_18cm_ABCD | 0.0092 | 0.1768 | 0.0099 | 0.1992 | 0.9700 | 0.9869 | 0.0094 | 0.1851 | 0.9855 | 0.9928 | 0.0086 | 0.1682 | 0.8914 | 0.9510 |
| 9mm_18cm_DCBA | 0.0092 | 0.1768 | 0.0102 | 0.1996 | 0.9641 | 0.9860 | 0.0100 | 0.1980 | 0.9754 | 0.9900 | 0.0087 | 0.1641 | 0.8635 | 0.9365 |
| Average | 0.0092 | 0.1768 | 0.0101 | 0.1994 | 0.9670 | 0.9865 | 0.0097 | 0.1915 | 0.9804 | 0.9914 | 0.0087 | 0.1661 | 0.8775 | 0.9437 |
| σ | 0.0000 | 0.0000 | 0.0002 | 0.0003 | 0.0042 | 0.0006 | 0.0004 | 0.0091 | 0.0072 | 0.0020 | 0.0001 | 0.0029 | 0.0197 | 0.0103 |
| 16mm_18cm_ABCD | 0.0160 | 0.1795 | 0.0154 | 0.1786 | 0.9775 | 0.9897 | 0.0162 | 0.1816 | 0.9955 | 0.9978 | 0.0162 | 0.1820 | 0.9704 | 0.9851 |
| 16mm_18cm_DCBA | 0.0160 | 0.1795 | 0.0157 | 0.1776 | 0.9788 | 0.9899 | 0.0165 | 0.1775 | 0.9951 | 0.9978 | 0.0162 | 0.1807 | 0.9728 | 0.9863 |
| Average | 0.0160 | 0.1795 | 0.0155 | 0.1781 | 0.9782 | 0.9898 | 0.0163 | 0.1796 | 0.9953 | 0.9978 | 0.0162 | 0.1813 | 0.9716 | 0.9857 |
| σ | 0.0000 | 0.0000 | 0.0002 | 0.0007 | 0.0009 | 0.0002 | 0.0002 | 0.0029 | 0.0003 | 0.0000 | 0.0000 | 0.0009 | 0.0017 | 0.0009 |
| 37mm_33cm_ABCD | 0.0369 | 0.3271 | 0.0350 | 0.3236 | 0.9943 | 0.9991 | 0.0364 | 0.3284 | 0.9989 | 0.9996 | 0.0358 | 0.3304 | 0.9943 | 0.9977 |
| 37mm_33cm_DCBA | 0.0369 | 0.3271 | 0.0359 | 0.3105 | 0.9959 | 0.9990 | 0.0373 | 0.3158 | 0.9993 | 0.9997 | 0.0367 | 0.3358 | 0.9913 | 0.9957 |
| Average | 0.0369 | 0.3271 | 0.0355 | 0.3170 | 0.9951 | 0.9991 | 0.0369 | 0.3221 | 0.9991 | 0.9996 | 0.0362 | 0.3331 | 0.9928 | 0.9967 |
| σ | 0.0000 | 0.0000 | 0.0006 | 0.0093 | 0.0011 | 0.0001 | 0.0006 | 0.0089 | 0.0003 | 0.0000 | 0.0007 | 0.0039 | 0.0021 | 0.0014 |
| 37mm_33cm_BACD | 0.0369 | 0.3062 | 0.0393 | 0.3165 | 0.9956 | 0.9995 | 0.0377 | 0.3105 | 0.9987 | 0.9994 | 0.0381 | 0.2747 | 0.8683 | 0.9325 |
| 27mm_32cm_ABCD | 0.0267 | 0.3174 | 0.0258 | 0.3222 | 0.9951 | 0.9983 | 0.0268 | 0.3217 | 0.9972 | 0.9986 | 0.0260 | 0.3258 | 0.9816 | 0.9913 |
| 27mm_32cm_DCBA | 0.0267 | 0.3174 | 0.0252 | 0.3176 | 0.9922 | 0.9980 | 0.0258 | 0.3147 | 0.9960 | 0.9986 | 0.0262 | 0.3213 | 0.9877 | 0.9941 |
| Average | 0.0267 | 0.3174 | 0.0255 | 0.3199 | 0.9937 | 0.9981 | 0.0263 | 0.3182 | 0.9966 | 0.9986 | 0.0261 | 0.3236 | 0.9847 | 0.9927 |
| σ | 0.0000 | 0.0000 | 0.0004 | 0.0033 | 0.0021 | 0.0002 | 0.0007 | 0.0050 | 0.0009 | 0.0000 | 0.0001 | 0.0032 | 0.0042 | 0.0020 |

Table 2-6. Summary of results obtained from the accuracy assessment experiments.

| Values from roughness references | | | | | | | | | |
|--|-------|-------|-------|-------|----------|-------|-------|-------|-------|
| Height RMS (s) [m] | 0.009 | 0.020 | 0.030 | 0.038 | 0.000 | 0.009 | 0.016 | 0.027 | 0.037 |
| Correlation length (l) [m] | 0.006 | 0.006 | 0.006 | 0.006 | ∞ | 0.177 | 0.180 | 0.317 | 0.327 |
| # Samples | 4 | 4 | 4 | 4 | 4 | 2 | 2 | 2 | 2 |
| Values from meshboard derived data | | | | | | | | | |
| Profile correlation coefficient | 0.960 | 0.988 | 0.980 | 0.993 | - | 0.991 | 0.998 | 0.999 | 1.000 |
| Profile R ² | 0.921 | 0.977 | 0.960 | 0.986 | - | 0.980 | 0.995 | 0.997 | 0.999 |
| Height RMS " s " [m] | 0.010 | 0.020 | 0.030 | 0.039 | 0.001 | 0.010 | 0.016 | 0.026 | 0.037 |
| σ Height RMS " s " [m] | 0.001 | 0.000 | 0.000 | 0.001 | 0.000 | 0.000 | 0.000 | 0.001 | 0.000 |
| Correlation length " l " [m] | 0.006 | 0.007 | 0.007 | 0.006 | 0.256 | 0.192 | 0.180 | 0.318 | 0.322 |
| σ Correlation length " l " [m] | 0.000 | 0.000 | 0.000 | 0.000 | 0.015 | 0.009 | 0.003 | 0.005 | 0.009 |
| Values from ground-based scanning LiDAR data | | | | | | | | | |
| Profile correlation coefficient | 0.848 | 0.930 | 0.797 | 0.887 | - | 0.944 | 0.986 | 0.993 | 0.997 |
| Profile R ² | 0.564 | 0.767 | 0.439 | 0.643 | - | 0.877 | 0.972 | 0.985 | 0.993 |
| Height RMS " s " [m] | 0.008 | 0.016 | 0.024 | 0.030 | 0.004 | 0.009 | 0.016 | 0.026 | 0.036 |
| σ Height RMS " s " [m] | 0.000 | 0.000 | 0.002 | 0.001 | 0.001 | 0.000 | 0.000 | 0.000 | 0.001 |
| Correlation length " l " [m] | 0.009 | 0.008 | 0.009 | 0.008 | 0.007 | 0.166 | 0.181 | 0.324 | 0.333 |
| σ Correlation length " l " [m] | 0.001 | 0.000 | 0.001 | 0.001 | 0.001 | 0.003 | 0.001 | 0.003 | 0.004 |

Table 2-7. Roughness parameter values obtained from agricultural soils using meshboard and LiDAR.

| Dataset | Meshboard | | | | | | | | | LiDAR | | | | | | | | |
|-----------------|-----------|-------|----------|---------|-------|-------|-------|-------|-------|-------|-------|----------|---------|-------|-------|-------|-------|-------|
| | RMSH | CL | PSL n | R2 E | G | P | E-cl | G-cl | P-cl | RMSH | CL | PSL n | R2 E | G | P | E-cl | G-cl | P-cl |
| 20060308 | 0.008 | 0.155 | 1.43 | 0.501 | 0.598 | 0.585 | 0.870 | 0.884 | 0.981 | 0.007 | 0.113 | 1.52 | 0.532 | 0.627 | 0.616 | 0.843 | 0.929 | 0.988 |
| 20060310A | 0.007 | 0.081 | 1.17 | 0.739 | 0.763 | 0.763 | 0.982 | 0.827 | 0.994 | 0.007 | 0.091 | 1.25 | 0.517 | 0.601 | 0.577 | 0.965 | 0.858 | 0.990 |
| 20060310B | 0.004 | 0.053 | 0.94 | 0.555 | 0.517 | 0.555 | 0.985 | 0.695 | 0.984 | 0.004 | 0.030 | 1.13 | 0.480 | 0.453 | 0.484 | 0.991 | 0.865 | 0.998 |
| 2009_MB&Ltest01 | 0.012 | 0.136 | 0.99 | 0.502 | 0.465 | 0.503 | 0.997 | 0.597 | 0.996 | 0.012 | 0.190 | 0.77 | 0.454 | 0.466 | 0.357 | 0.934 | 0.212 | 0.990 |
| 2009_MB&Ltest02 | 0.008 | 0.034 | 1.47 | 0.523 | 0.535 | 0.542 | 0.951 | 0.966 | 1.000 | 0.009 | 0.055 | 1.30 | 0.465 | 0.442 | 0.462 | 0.966 | 0.905 | 1.000 |
| 2009_MB&Ltest03 | 0.023 | 0.156 | 1.17 | 0.497 | 0.580 | 0.542 | 0.980 | 0.767 | 0.998 | 0.018 | 0.157 | 1.01 | 0.459 | 0.533 | 0.462 | 0.998 | 0.601 | 0.998 |
| 2009_MB&Ltest04 | 0.023 | 0.115 | 1.57 | 0.388 | 0.494 | 0.481 | 0.857 | 0.953 | 0.991 | 0.025 | 0.117 | 1.51 | 0.358 | 0.481 | 0.458 | 0.875 | 0.934 | 0.992 |
| 2009_MB&Ltest05 | 0.001 | 0.190 | 1.14 | 0.349 | 0.480 | 0.399 | 0.864 | 0.564 | 0.870 | 0.003 | 0.238 | 0.43 | 0.367 | 0.402 | -0.21 | 0.003 | -2.24 | 0.885 |
| 2009_MB&Ltest06 | 0.002 | 0.170 | 1.01 | 0.451 | 0.515 | 0.455 | 0.992 | 0.628 | 0.991 | 0.003 | 0.119 | 0.75 | 0.478 | 0.392 | 0.450 | 0.917 | 0.214 | 0.980 |
| 2009_MB&Ltest07 | 0.005 | 0.067 | 1.81 | 0.559 | 0.665 | 0.662 | 0.810 | 0.992 | 0.999 | 0.008 | 0.090 | 1.52 | 0.497 | 0.563 | 0.556 | 0.908 | 0.954 | 0.996 |
| 2009_MB&Ltest08 | 0.004 | 0.073 | 1.62 | 0.658 | 0.708 | 0.708 | 0.884 | 0.975 | 0.999 | 0.005 | 0.067 | 1.57 | 0.397 | 0.481 | 0.473 | 0.872 | 0.949 | 0.981 |
| 2009_MB&Ltest09 | 0.006 | 0.078 | 2.16 | 0.132 | 0.217 | 0.222 | 0.666 | 0.995 | 0.996 | 0.008 | 0.076 | 0.86 | 0.225 | 0.290 | 0.202 | 0.942 | 0.466 | 0.948 |
| 2009_MB&Ltest10 | 0.013 | 0.187 | 1.35 | 0.515 | 0.561 | 0.564 | 0.931 | 0.884 | 0.999 | 0.013 | 0.099 | 1.53 | 0.617 | 0.653 | 0.655 | 0.871 | 0.950 | 0.998 |
| 2009_MB&Ltest11 | 0.015 | 0.130 | 1.72 | 0.588 | 0.683 | 0.678 | 0.824 | 0.986 | 0.999 | 0.014 | 0.141 | 1.52 | 0.567 | 0.662 | 0.647 | 0.886 | 0.947 | 0.997 |
| 2009_MB&Ltest12 | 0.016 | 0.092 | 1.60 | 0.601 | 0.622 | 0.625 | 0.879 | 0.972 | 0.999 | 0.015 | 0.086 | 1.72 | 0.577 | 0.641 | 0.638 | 0.827 | 0.981 | 0.996 |
| 2009_MB&Ltest13 | 0.007 | 0.034 | 1.87 | 0.541 | 0.560 | 0.561 | 0.891 | 0.995 | 0.998 | 0.007 | 0.035 | 1.38 | 0.489 | 0.490 | 0.499 | 0.958 | 0.951 | 0.999 |
| 2009_MB&Ltest16 | 0.015 | 0.041 | 2.36 | 0.090 | 0.132 | 0.136 | 0.850 | 0.996 | 0.991 | 0.011 | 0.043 | 1.72 | 0.123 | 0.162 | 0.161 | 0.925 | 0.970 | 0.989 |
| 2009_MB&Ltest17 | 0.003 | 0.121 | 1.38 | 0.436 | 0.541 | 0.510 | 0.923 | 0.900 | 0.988 | 0.005 | 0.082 | 0.75 | 0.381 | 0.423 | 0.293 | 0.910 | 0.310 | 0.963 |
| 2009_MB&Ltest18 | 0.007 | 0.283 | 1.06 | 0.401 | 0.524 | 0.427 | 0.992 | 0.629 | 0.995 | 0.005 | 0.016 | 0.57 | 0.541 | 0.459 | 0.619 | 0.997 | 0.892 | 0.980 |
| 2009_MB&Ltest19 | 0.017 | 0.078 | 1.62 | 0.542 | 0.660 | 0.649 | 0.858 | 0.971 | 0.999 | 0.018 | 0.095 | 1.34 | 0.427 | 0.547 | 0.514 | 0.947 | 0.897 | 1.000 |
| 2009_MB&Ltest20 | 0.039 | 0.252 | 1.48 | 0.423 | 0.534 | 0.517 | 0.885 | 0.933 | 1.000 | 0.044 | 0.244 | 1.62 | 0.445 | 0.545 | 0.538 | 0.825 | 0.967 | 1.000 |

Table 2-8. Comparison of roughness parameter values of agricultural soils obtained from LiDAR and meshboard data.

| | Meshboard | LiDAR |
|--|-----------|--------------|
| Correlation coefficient of “ <i>s</i> ”, (R^2) | | 0.97, (0.95) |
| Correlation coefficient “ <i>l</i> ”, (R^2) | | 0.50, (0.25) |
| R^2 exponential and real ACF | 0.48±0.15 | 0.45±0.12 |
| R^2 Gaussian and real ACF | 0.54±0.15 | 0.49±0.12 |
| R^2 exponential and real ACF to “ <i>l</i> ” | 0.90±0.08 | 0.87±0.21 |
| R^2 Gaussian and real ACF to “ <i>l</i> ” | 0.86±0.15 | 0.78±0.27 |
| Exponent power law spectrum | 1.47±0.38 | 1.23±0.40 |

CHAPTER 3

TESTING ROUGHNESS CHARACTERIZATION ASSUMPTIONS USING A DATABASE OF 2D PROFILES OBTAINED WITH GROUND-BASED LIDAR

Once it was demonstrated that measurements from the ground-based LiDAR yield precise and accurate values of roughness parameters, the next step was to test some of the current assumptions of surface roughness characterization in two dimensions (2D). These assumptions include: the single-scale nature of roughness, possible correlation between roughness parameter values, and if the Gaussian or exponential models adequately describe the ACFs agricultural soils. This is an intermediate step toward the characterization of three-dimensional (3D) roughness of agricultural soils, which is covered in the next chapter. To validate the current assumptions of 2D roughness characterization, a large database of agricultural surface transect data was collected. This chapter describes how this database was collected and how it was used to test traditional characterization assumptions.

Instrumentation and Datasets

Mobile Terrestrial Laser Scanner (M-TLS)

Data was collected utilizing the University of Florida mobile terrestrial laser scanning (M-TLS) system, which is shown in Figure 3-1. The M-TLS is a unique tool that enables UF geosensing engineering and mapping (GEM) researchers to acquire high-density LiDAR point clouds from an elevated viewing point. The core of the M-TLS is an Optech ILRIS 3D, commercial 2-axis time-of-flight ground-based laser scanner. The ILRIS is integrated to a mobile telescoping, rotating, and tilting platform that provides up to 6 degrees of freedom for performing scanning operations. The platform, which can be elevated to a height of 10 meters above the surface, is mounted on the bed of a heavy-duty 4x4 truck. From an elevated position and employing the rotating

base, the M-TLS can quickly generate 3D maps of agricultural surfaces of areas of hundreds of square meters with millimeter level resolution and precision. The specifications and description of operation of the M-TLS are covered extensively in [19].

Data Collection and Preprocessing

The M-TLS was used to obtain 3D point clouds of the soil surface from a height of 5 to 7 meters with a sample spacing that ranged from 5 mm to 3 cm. Most datasets were collected at the University of Florida/Institute of Food and Agricultural Sciences (UF/IFAS) Plant Science Research and Education Unit (PSREU), located 20 miles south of Gainesville, at 2556 West Highway 318, Citra, Florida. Since 2003, PSREU has been the location of the seasonal Microwave Water and Energy Balance Experiment (MicroWEX), MicroWEX is carried out by the Center for Remote Sensing of the Agricultural and Biological Engineering Department at UF. Soil roughness measurements were collected as part of MicroWEX-4 in the spring of 2005 using the meshboard [35] and [36]. Concurrent meshboard and ground-based LiDAR observations were collected for MicroWEX-5 in the spring of 2006 [37], MicroWEX-7 in the spring of 2007, and MicroWEX-8 in the summer of 2009. In addition to the roughness measurements collected as part of the MicroWEX seasonal experiments, several other datasets were acquired at PSREU. And additional bare surface datasets were collected at St. Augustine and Hastings, Florida; along the shore of the Great Salt Lake in Utah, and Houston, Texas. A total of 112 ground-based LiDAR scans of natural surfaces were collected over a four year period.

Raw LiDAR data from the M-TLS are irregular point clouds with an arbitrary reference frame determined by the orientation of the ILRIS instrument at the moment of data collection. When mapping from a height of 5 to 7 meters, the ILRIS instrument is

tilted downward. As a result, the raw point cloud will appear to be tilted upward as shown in Figure 3-2A. These tilted point clouds require rectification. Because surface roughness metrics are computed with relative high variations and not absolute values, it is not crucial that the point cloud be leveled according to the local gravity vector at the moment of collection. A decimated sample of the point cloud first fits to a plane using a least squares regression following the model:

$$Z = aX + bY + c, \tag{3-1}$$

where X, Y, Z are the observed 3D coordinates of each point of the plane, and a, b, c are the parameters defining the plane. Those parameters also define the normal vector to the plane as [a, b, -1]. From this normal vector, the rotation angles around the X (R_x) and Y (R_y) axes, which are required to level the plane, are determined using:

$$R_x = \tan^{-1}(-b), \tag{3-2}$$

$$R_y = -\tan^{-1}(-a). \tag{3-3}$$

If the surface presented spatial structure, such as that arising from agricultural rows or linear features, the point cloud was also rotated about the Z axis such that these features were aligned to the Y axis. The rotations were performed using a TerraScan 3D rotate and translate transformation module. From the leveled and oriented point cloud, square regions of interest with dimensions that ranged from 3 to 6.75 meters to a side (9 to 45.65 m²) were cropped. Finally, the coordinates of the cropped point cloud were modified by a simple arithmetic transformation, such that the lower left coordinates corresponded to the origin (x = 0, y = 0), and the average of the Z components was zero. Figure 3-2 shows renderings of a raw point cloud, along with the processed (rotated and cropped) point cloud.

To facilitate the mathematical manipulation of the data, the irregular point clouds were transformed into digital elevation models (DEMs) also known as grids. A DEM is essentially a matrix composed of equally spaced elements called cells, organized in rows and columns. Each cell has three attributes, two correspond to a unique horizontal position (i.e. easting, northing or latitude, longitude) and the third to an elevation value representative of the entire cell. To create a DEM, the first step is to establish a regular mesh using the horizontal position (x, y) information. Cell height is obtained by interpolating height information from the irregular point cloud to the grid nodes. For this study, DEMs with a cell spacing of 1 cm were created by applying a triangulation with linear interpolation method.

A total of 21 agricultural surfaces with different roughness conditions ranging from smooth to very rough were selected for the analyses presented in this and the following chapter. The details pertaining to the collection dates and locations, the surface conditions, and the square lateral dimensions in meters for these 21 surfaces are presented in Table 3-1. Figure 3-3 shows four samples of the studied agricultural surfaces in photographs and, to each sample's right its ground-based LiDAR derived DEM.

2D Profile Database

To test the assumptions used in the characterization of surface roughness, a large database of 2D profiles was created. This was done by extracting all the profiles along the row and column directions of the 3D DEMs obtained for the 21 study surfaces. A total of 20,072 profiles with lengths that ranged from 3 to 6.75 meters were obtained, totaling 100.4 km of height variation data. These profiles were detrended using the linear, quadratic, and FFT filter models. Several analyses were performed with this

database of surface roughness information. These analyses included the sensitivity of the roughness parameters to the detrending method, the existence of a correlation between RMS_h and correlation length, and how well the theoretical exponential and Gaussian ACF models described the ACF of agricultural and natural surfaces. The results of these analyses are described next.

Testing Roughness Characterization Assumptions

Value Ranges for Roughness Parameters

Because the different microwave emission and scattering models are valid over different roughness domains, significant effort has been put into determining value ranges for the roughness parameters. In [38] a plan was described to establish global joint statistics for both RMS_h and correlation length for bare agricultural soils over a variety of tillage conditions based on a database of roughly 1,500 1-meter profiles obtained in 6 European countries. The researchers found that the RMS_h can vary between 6 mm for seedbed soils to 2.7 cm for plowed surfaces, with a mean value of 1.6 ± 1.1 cm [38]. A survey of similar studies revealed that the RMS_h for agricultural soils varies in the range from 2.5 mm for sown fields to 4.1 cm for plowed fields [7]. With respect to the correlation length, it has been extremely difficult to obtain consistent range of correlation lengths. In [38] it was found that the typical value for correlation lengths was 4.8 ± 1.8 cm. A compilation from recent studies yields values in a range between 2 and 20 cm [7].

The minimum, maximum, mean, and standard deviation of the roughness parameters obtained from the profile database for the three different detrending methods are summarized in Table 3-2. It can be seen that the RMS_h values obtained from the first order detrending are consistent with the reported values. A significant

difference arises with respect to the correlation length, where the maximum correlation length obtained was 81 cm, roughly four times the maximum reported in previous studies. This can be attributed to the fact that longer profiles are available in this database than those previously used. As shown in [2], longer profiles yield larger and more accurate values of the correlation length. It can also be demonstrated that when applying Equation 1-6 the maximum observable correlation length is close to 0.62 of the measured profile length. Consequently, short profiles will limit the value that can be determined for the correlation length.

Sensitivity of Roughness Parameters to the Detrending Procedure

To assess the sensitivity of roughness parameters to the detrending procedure, the coefficient of determination (R^2) for the fit of the profile data to the modeled trend was computed using Equation 1-13. All the profiles were detrended according to the 3 earlier models described and the R^2 of fit was determined for each, then the difference between the R^2 of the first and second order trends, as well as the difference between the first and FFT filter trend, were computed. In the same fashion, the differences between the values of the associated roughness parameters were determined.

Figure 3-4 shows the results from this analysis. It was found that as the R^2 of the trend increases, the values of RMS_h and correlation length decrease. If the first and second order detrending methods are considered, the correlation coefficient between the differences in R^2 and the differences in RMS_h was -0.809, and the correlation coefficient between the differences in R^2 with respect to the differences in correlation length was -0.786. Considering the linear and the FFT filter detrending methods, the correlation coefficient between the differences in R^2 and the differences in RMS_h was -0.786, and the correlation coefficient between the differences in R^2 with respect to the

differences in correlation length -0.57. These results demonstrate the high sensitivity of the roughness parameters values to the detrending method, the multi-scale nature of agricultural and natural soils, and the need to establish the proper detrending technique to characterize roughness at a given scale.

Correlation between RMS_h and Correlation Lengths

Several studies have attempted to derive models that relate the correlation length to the RMS [38], or to perform empirical or semi-empirical calibrations of the IEM by adjusting measured correlation lengths [27] and [28]. This is done to reduce the parameterization of surface roughness for its use in microwave emission or scattering models. It is also done to circumvent the problem of obtaining precise and repeatable values of correlation lengths. A dispersion plot, shown in Figure 3-5, was generated from the extracted profiles database and shows the correlation between the RMS_h and correlation lengths obtained from the different detrending methods. In contrast to the previously cited publications, where good correlation between RMS_h and correlation lengths were found, this result indicated a large spread between values of both roughness parameters. However, it can also be seen that the spread is reduced when second order and FFT filter detrending is applied. The correlation coefficient between RMS_h and correlation lengths was found to be 0.1 for first order detrending, 0.132 for second order detrending, and 0.355 for FFT filtering detrending. An additional observation only considering the spread for the FFT filter detrended data is that there is a probable correlation between the RMS_h and the maximum attainable correlation length. This is a negative correlation, i.e., as the RMS_h increases the maximum observable correlation length decreases.

Exponential or Gaussian ACF Models

Because the results of soil moisture inversion using the Integral Equation Model vary strongly between the Gaussian and Exponential ACF models [7], the shape of the autocorrelation function is an essential descriptor of the soil surface roughness. To explore this issue, the least squares method described with Equation 2-5 was used to determine the exponent “n” of the generalized power law spectrum that best fits the ACF obtained for the random height component. The R^2 was used as a metric to determine how well the observed ACF matched the modeled exponential, Gaussian, and generalized power law spectrum ACF. The R^2 was computed twice, once considering the entire lag range, then again only considering the range from the zero lag to the correlation length. The results from this analysis are summarized in Table 3-3 and in Figures 3-6 and 3-7.

The first conclusion that can be drawn from these results is that more profiles follow exponential than Gaussian ACFs, adding validity to the assumption that soil surfaces can be better explained with exponential ACFs. However, the vast majority of profiles follow ACFs somewhere between the theoretical Gaussian ($n = 2$) and exponential ($n = 1$) models. Also, the detrending method affects the shape of the autocorrelation function, and it can be seen from the histograms in Figure 3-6 that for higher order detrending methods there is a relatively higher number of profiles with ACFs with exponents closer to the Gaussian model ($n = 2$). Figure 3-7 shows histograms with the R^2 values for the fit between the observed ACF and the theoretical exponential or Gaussian ACF forms considering the entire lag range. These histograms show that the theoretical ACF does not represent well the real ACF for the entire lag

range. This is also evidence of the multi-scale nature of agricultural and natural surfaces.

Chapter Conclusions

The main conclusion that can be drawn from the analyses of 2D roughness presented in this chapter is that natural and agricultural surfaces have roughness components at different scales. This is in contradiction to the main assumption of roughness characterization, where roughness is considered a stationary single-scale process. However, with high resolution, large extent data obtained from ground-based LiDAR and proper detrending techniques, making it possible to characterize roughness at different scales. The question that still remains to be answered by the microwave remote sensing community is: What are the relevant scales that need to be considered? The theoretical Gaussian and exponential ACF models are just two specific cases of an entire universe of ACF that can be characteristic of agricultural and natural surfaces. Also, they do not explain the structural correlation of random components observed at lags longer than the correlation length.



Figure 3-1. The M-TLS system performing agricultural surface scanning operations.

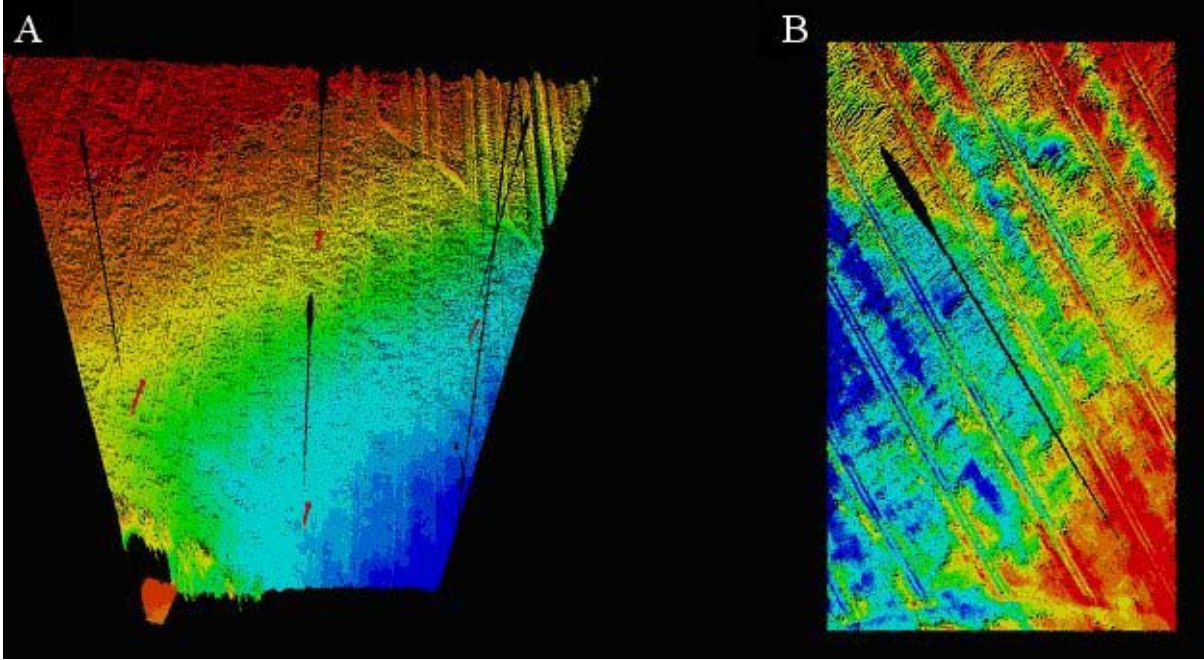


Figure 3-2. Point cloud renderings of a ground-based LiDAR dataset at different processing steps, A) raw and B) rectified..

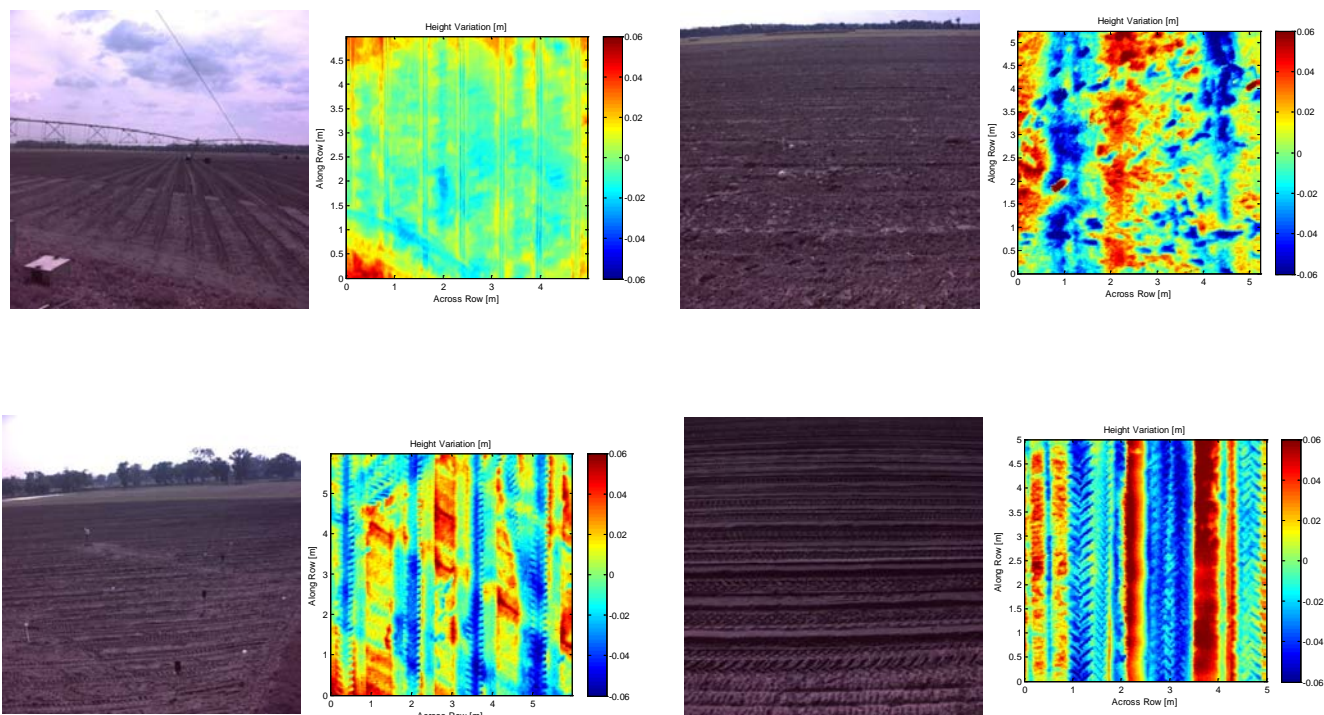


Figure 3-3. Samples of studied soil surface and their ground-based LiDAR derived 3D DEMs.

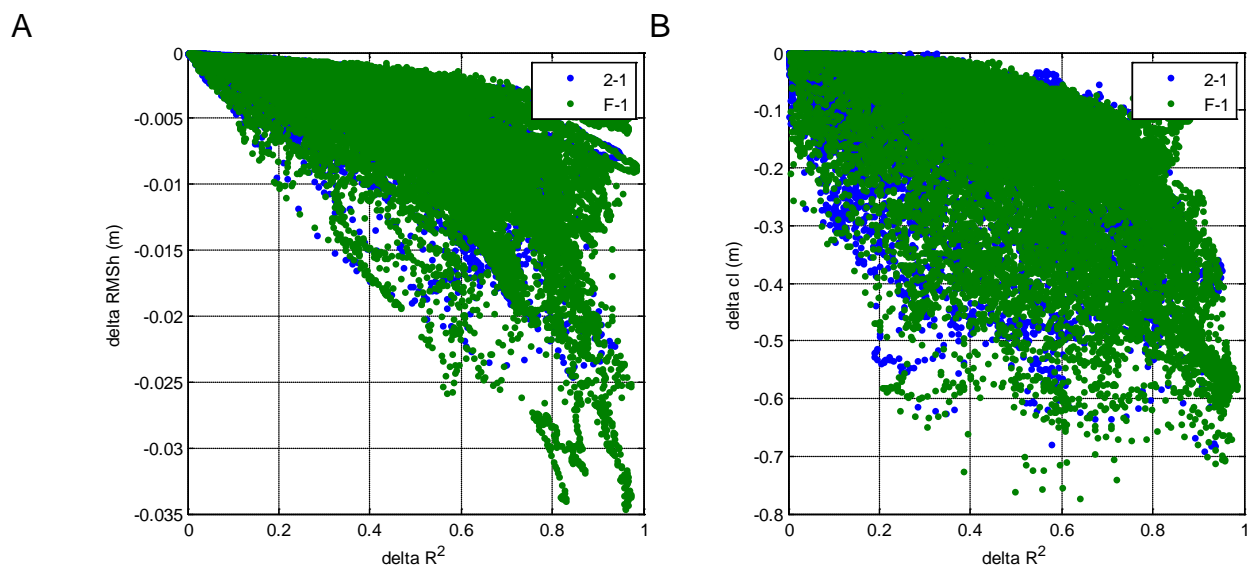


Figure 3-4. Effects of detrending on the derived roughness parameters. A) RMS. B) correlation lengths.

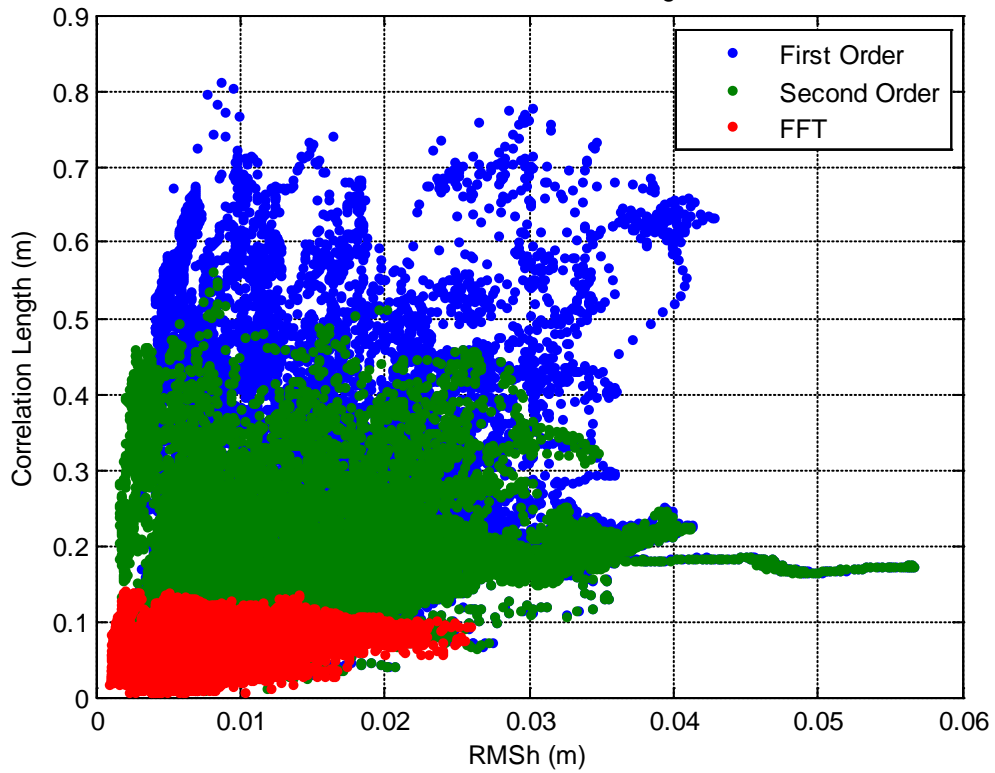


Figure 3-5. Dispersion plots of the random height component derived correlation lengths and RMSh for the different detrending methods.

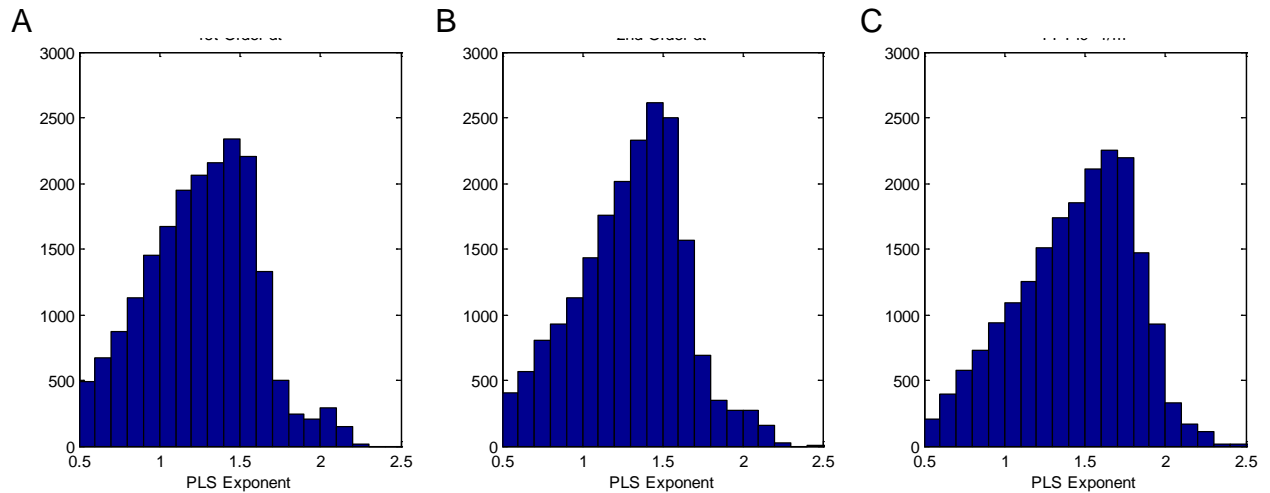


Figure 3-6. Histograms of the exponent values for the Power Law Spectrum ACF model obtained from the soil profiles.

A) First order detrending. B) Second order detrending. C) Third order detrending.

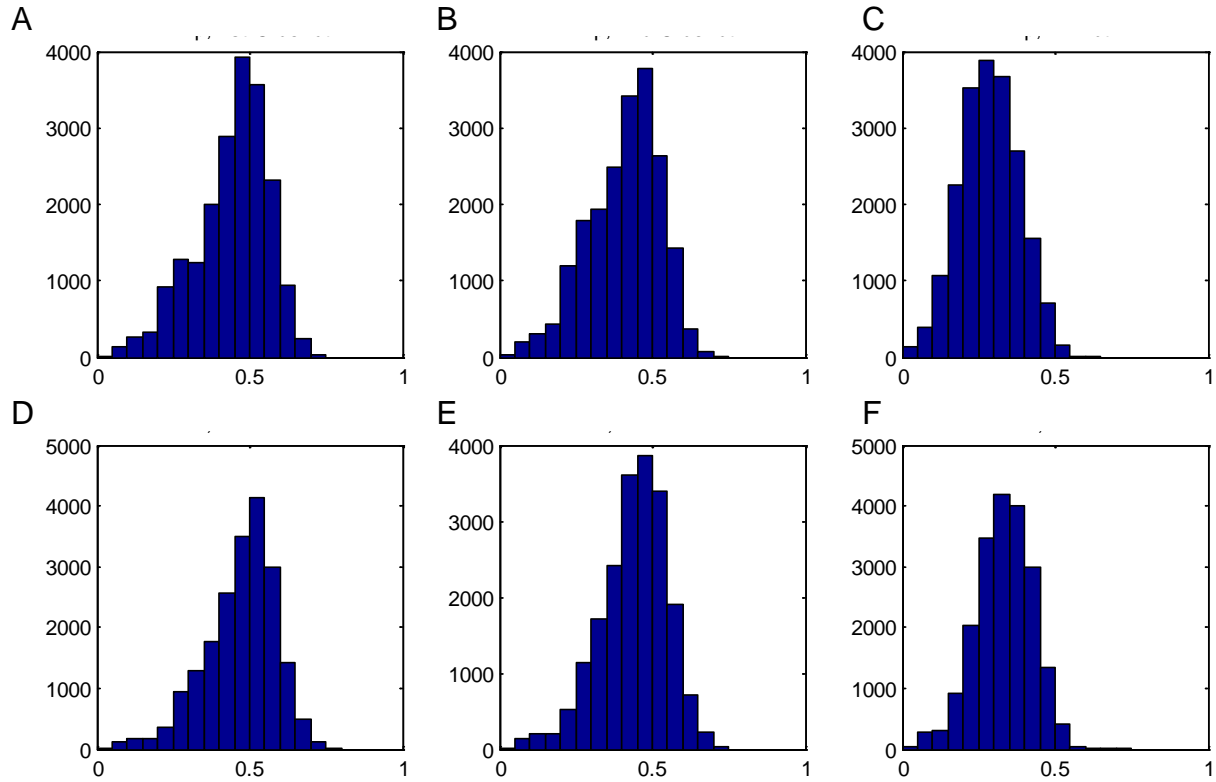


Figure 3-7. Histograms of the R^2 values of the fit of the observed ACF model with respect to the theoretical models.

A) Exponential, first order detrending. B) Exponential, second order detrending. C) Exponential, FFT detrending. D) Gaussian, first order detrending. E) Gaussian, second order detrending. F) Gaussian, FFT detrending.

Table 3-1. 3D digital elevation models derived from LiDAR for the study.

| # | Lateral dimensions | Date | Location | Surface condition |
|----|--------------------|-----------|-------------------|---------------------|
| 1 | 6.00 | 18-Mar-08 | St. Augustine, FL | Natural smooth |
| 2 | 4.37 | 8-Mar-06 | PSREU Citra, FL | Harrowed smooth |
| 3 | 4.50 | 21-Jun-10 | Houston, TX | Natural smooth |
| 4 | 5.00 | 10-Mar-06 | PSREU Citra, FL | Rolled |
| 5 | 5.00 | 10-Mar-06 | PSREU Citra, FL | Rolled |
| 6 | 3.50 | 11-Nov-07 | Salt Lake, UT | Natural clay soil |
| 7 | 4.25 | 18-Nov-09 | PSREU Citra, FL | Harrowed |
| 8 | 3.02 | 18-Nov-09 | PSREU Citra, FL | Harrowed |
| 9 | 5.38 | 18-Nov-09 | PSREU Citra, FL | Natural |
| 10 | 4.50 | 3-Sep-10 | PSREU Citra, FL | Plowed |
| 11 | 6.00 | 29-Apr-07 | PSREU Citra, FL | Plowed |
| 12 | 3.23 | 18-Nov-09 | PSREU Citra, FL | Gravel bed |
| 13 | 5.00 | 3-Sep-10 | PSREU Citra, FL | Harrowed |
| 14 | 5.72 | 18-Nov-09 | PSREU Citra, FL | Harrowed |
| 15 | 5.24 | 18-Nov-09 | PSREU Citra, FL | Harrowed |
| 16 | 5.00 | 3-Sep-10 | PSREU Citra, FL | Plowed |
| 17 | 6.00 | 29-Apr-07 | PSREU Citra, FL | Plowed |
| 18 | 3.10 | 24-Jun-09 | PSREU Citra, FL | Furrowed sandy soil |
| 19 | 5.01 | 8-Dec-09 | PSREU Citra, FL | Furrowed sandy soil |
| 20 | 6.75 | 8-Dec-09 | PSREU Citra, FL | Furrowed sandy soil |
| 21 | 4.00 | 28-Oct-06 | Hasting, FL | Ridged sandy soil |

Table 3-2. Roughness parameter values in cm, derived from 20,072 profiles of agricultural soils.

| | 1st order | 2nd order | FFT filter |
|---|-------------|------------|------------|
| RMS _h , minimum / maximum | 0.3 - 4.3 | 0.2 - 3.6 | 0.1 - 2.6 |
| RMS _h , mean ± standard deviation | 1.4 ± 0.7 | 1.2 ± 0.7 | 0.8 ± 0.4 |
| Correlation length min/max | 0.9 - 81.1 | 0.8 - 56.2 | 0.6 - 14.2 |
| Correlation length, mean ± standard deviation | 24.6 ± 15.8 | 17.3 ± 9.6 | 6.7 ± 2.3 |

Table 3-3. Mean parameter and fit metric values for different ACF models.

| Mean | 1st order | 2nd order | FFT filter |
|--|-----------|-----------|------------|
| PLS exponent | 1.2463 | 1.2913 | 1.4258 |
| R ² Exponential | 0.4427 | 0.4076 | 0.2853 |
| R ² Gaussian | 0.4709 | 0.4398 | 0.3318 |
| R ² PLS | 0.4461 | 0.4175 | 0.3161 |
| R ² exponential to the correlation length | 0.8758 | 0.8813 | 0.8943 |
| R ² Gaussian to the correlation length | 0.6117 | 0.6818 | 0.8356 |
| R ² PLS to the correlation length | 0.9852 | 0.9865 | 0.9935 |

CHAPTER 4 DERIVING THREE DIMENSIONAL (3D) ROUGHNESS METRICS FROM GROUND- BASED LIDAR DIGITAL ELEVATION MODELS (DEMS)

As mentioned in Chapter 1 of this dissertation, some of the current challenges in the characterization of surface roughness arise from the approach of using two-dimensional (2D) profiles to try to deduce 3D characteristics. This approach is not adequate because profiles do not contain enough information to properly separate the random component from the surface trend, and it is unlikely that a single profile will record the extremes of a surface. These two aspects affect the accuracy of roughness parameters. As has been shown in the previous chapters, the values of the parameters vary significantly depending on how the random component was extracted, and not recording the extremes of the surface will cause an underestimation of the parameters [7]. Finally, profiling presents very limited information on the directional characteristics of the surface roughness.

The characterization of 3D roughness of agricultural and natural surfaces for application in microwave modeling is virtually unexplored. This is due in part because until recently technology that allows for the recording of fine-scale 3D height variation of large areas has not been readily available. Two alternatives are stereoscopic imagers as described in [12] and [16], or LiDAR scanners [15] and [22]. Stereoscopic imagers have the advantage of producing 3D digital elevation models with high resolution and high accuracy, but of a very small area ($\sim 1 \text{ m}^2$). LiDAR scanners have comparable resolution and are able to digitize larger areas ($\sim 10\text{s m}^2$), but with somewhat lower accuracy. To date, there has been very little research on the characterization of 3D soil roughness using these digitization instruments. Most research [12], [16], [39] limits the 3D information obtained to extract 2D profiles and derive roughness parameters based

on the traditional transect methodology. Little has been determined about how the results obtained with the traditional 2D techniques compare to the ones obtained from 3D characterizations.

In the previous chapter, the assumptions used for the characterization of surface roughness from 2D profiles were tested. Also, value ranges for the parameters were obtained using the traditional 2D formulation. This chapter extends the traditional 2D characterization by exploring alternatives to characterize 3D roughness from ground-based LiDAR-derived DEMs. It begins with a description of the methodology used to detrended 3D DEMs from which roughness parameters will be computed. A comparison between the roughness parameter values obtained from the traditional 2D methodology versus the 3D formulation is also performed. This is followed by an analysis of the impact in the modeled microwave emission and scattering due to difference in the 2D versus 3D parameterization of roughness. Finally, the advantage that 3D brings to the characterization of roughness is illustrated by a case of quasi-periodic agricultural surfaces.

Datasets and Preprocessing

The 3D DEMs from the 21 surfaces that were used in the previous chapter to build the database of 2D profiles, are used in this chapter to perform the 3D roughness characterization. To derive roughness parameters from the 3D DEMs two main approaches were followed. The first approach consists of extracting all the profiles along the rows and columns of the DEM, detrending them individually, computing the roughness parameters, then averaging all the obtained values. The second approach consists of extending the 2D profile formulation to a 3D surface formulation and applying these to a detrended 3D DEM. Here is where the first difference between 2D

and 3D roughness characterization arises, because the trend obtained from individual transects may not represent the overall trend of the surface.

Optimal detrending of a 3D DEM can be done by FFT filtering, high order polynomials, and moving average filters, as described in [2]. For the computation of 3D roughness parameters, the 21 DEMs were detrended using 3D linear and quadratic models, and by applying a 3D FFT-based filter that removes the spectral components with spatial wavelengths longer than a meter. The first and second order 3D models applied for the purpose of detrending the DEMs are:

$$Z = aX + bY + c, \quad (4-1)$$

$$Z = aX^2 + bY^2 + cXY + dX + eY + f, \quad (4-2)$$

where X, Y, and Z are the coordinates of the observed points, and a, b, c, d, e, and f are the coefficients of the models. These coefficients are determined via a linear least squares process. The 2D Fast Fourier Transform applied to a matrix of M rows and N columns is:

$$F(u, v) = \sum_{x=1}^M \sum_{y=1}^N f(x, y) e^{-j2\pi \left(\frac{ux}{M} + \frac{vy}{N} \right)}. \quad (4-3)$$

The resulting FFT is also a matrix of M rows and N columns, but with complex elements. The detrending is achieved by setting to zero the elements of the FFT that correspond to a spatial wavelength larger than 1 meter. The modified FFT ($F'(u, v)$) is then transformed back to the space domain using the inverse FFT:

$$f'(x, y) = \sum_{x=1}^M \sum_{y=1}^N F'(u, v) e^{j2\pi \left(\frac{ux}{M} + \frac{vy}{N} \right)} \quad (4-4)$$

where $f'(x, y)$ is the detrended DEM, a matrix of the same dimensions M x N with real value elements. Figure 4-1 shows an original DEM, its trend according to the first and

second order models, the FFT-based trend, and their respective detrended random component DEMs.

Averaging Parameter Values Obtained From 2D Profiles

Averaging RMS_h values can be done by considering all the extracted profiles from the grid's rows and columns, or separating the profiles extracted from rows from those extracted columns and calculating the average for each group. This latter approach has the advantage that it yields information on the directional properties of the roughness, i.e., the isotropy of the surface. In [39] a ratio between the averaged RMS_h along the columns and the rows is proposed as a measure of the directionality of the surface roughness, is as follows:

$$I_{RMS_h} = \frac{mean(RMS_{h_{col}})}{mean(RMS_{h_{row}})} \quad (4-5)$$

If I_{RMS_h} is equal to 1, then the surface can be considered an absolute isotropic scatterer or emitter.

With regard to obtaining average values of correlation lengths, there are two ways described in literature. The first consists of averaging values of the correlation lengths for individual profiles; and the second consists of averaging the measured autocorrelation functions from which the correlation length is then determined. For the 21 surfaces in this study both ways for determining correlation lengths were tested. The correlation coefficient and the RMSE between the obtained values of correlation lengths are summarized in Table 4-1. Results indicate that despite high correlation coefficients between values, the root mean square difference between the values is close to 3 cm for first order detrending, and between 1 and 2 cm for second order detrending. These are significant differences between the values obtained from the two methods. For the

FFT filter-based detrending, however, the correlation length values agree to better than 5 mm. This indicates that, for determining single-scale correlation lengths, either method is equally valid. For the comparisons presented in the next sections, the method of averaging the correlation length values of individual profiles is used.

Extending 2D Formulations to 3D

Equation 1-5, used to compute RMS_h, is applicable to data extracted from both 2D profiles and 3D surface models. If this formulation is applied to the DEM, it provides an RMS_h value truly representative of the entire surface. However, there is the disadvantage that it does not provide information of the roughness directional properties. An alternative to derive directional roughness from a detrended DEM consist of extracting 2D radial profiles starting at the center and extending to the edge of the DEM at a given angular separation (Δang) from each other. For a square DEM with M rows, N = M columns and a cell spacing of Δc , the horizontal grid coordinates for each point “j” in the radial profile “r” are given by:

$$(Row\#, Col\#) = \left(\frac{M}{2} + \sin(r \times \Delta ang) \times (j \times \Delta c), \frac{M}{2} + \cos(r \times \Delta ang) \times (j \times \Delta c) \right). \quad (4-6)$$

For $r = 1, 2, \dots, 360 / \Delta ang$, and $j = 0, 1, \dots, M/2 - 1$. The height $h(r, j)$ for each point is then obtained by using nearest neighbor or bilinear interpolation from the DEM cell values. The RMS_h for each radial profile is then computed using Equation 1-5. Figure 4-2 A shows a first order detrended DEM and Figure 4-2 B shows its directional RMS_h as a function of the horizontal angle. This horizontal angle is measured with the vertex at the center of the grid, and with respect to a horizontal axis. This methodology provides a description of the roughness anisotropy of the surface. A quantitative measurement of this anisotropy is the eccentricity of the RMS_h given by:

$$e_{RMS_h} = \sqrt{1 - \frac{\min(RMS_h)^2}{\max(RMS_h)^2}} . \quad (4-7)$$

An eccentricity value of zero indicates a perfect isotropic surface.

To determine the correlation length from a full surface model with M rows and N columns, the normalized autocorrelation function for displacements in two directions h_x and h_y is computed by:

$$\rho(h_x, h_y) = \rho(j\Delta x, k\Delta y) = \frac{\sum_{a=1}^{N-j} \sum_{b=1}^{M-k} (z_{a,b} \times z_{a+j, b+k})}{\sum_{a=1}^N \sum_{b=1}^M (z_{a,b})^2} . \quad (4-8)$$

This is a 3D ACF, with two dimensions being the lags in the x and y directions, and the third dimension being the normalized autocorrelation. Figure 4-3 A shows the 3D autocorrelation function from the detrended DEM shown in Figure 4-2 A. In the profile formulation, the correlation length is uniquely defined as the lag for which the ACF value is 1/e. For the 3D formulation, the correlation length is not an unique value. Instead it is a set of values defined as the distance from the (0,0) lag point to each point (h_x, h_y) that defines the contour that has a normalized correlation value of 1/e. Figure 4-3 B shows the 1/e contour extracted from the 3D ACF in part A. From the 1/e contour, the correlation length at a direction θ_i is:

$$\ell(\theta_i) = \sqrt{h_{x_i}^2 + h_{y_i}^2} , \quad (4-9)$$

where the angle θ_i is given by:

$$\theta_i = \tan^{-1} \left(\frac{h_{y_i}}{h_{x_i}} \right) . \quad (4-10)$$

Figure 4-4 illustrates the correlation length derived from the 3D formulation as a function of the angle θ measured from the x lags axis.

An important lesson learned with respect to the computation of correlation lengths using the 3D formulation, has to do with those surfaces that presented linear features as arising from the agricultural row structures. Figure 4-5 A shows the detrended DEM of a surface exhibiting such linear characteristics. In Figure 4-5 B, a histogram with the distributions of the correlation length values obtained from the traditional 2D formulation is presented. The distribution contains correlation lengths within the values of 4 and 24 cm. Figure 4-5 C shows the 1/e contour extracted from the 3D autocorrelation function and Figure 4-5 D presents the 3D correlation length as a function of the horizontal angle. From Figure 4-5 C and Figure 4-5 D it can be seen that the normalized autocorrelation is extremely elongated in the Y direction, and the correlation length reaches a value of almost 1.8 meters, more than nine times the average value obtained from the 2D formulation. This elongation of the correlation lengths is due to the row structure, as the height variations will be highly correlated in the row direction compared to the across-row direction. To eliminate this elongation effect and to obtain coherent values of correlation lengths, it is necessary to apply an additional detrending procedure that removes the row structure. To do this, a simple Matlab routine was coded. For each column on the DEM, the routine determines the difference between the average height value of the column and the average height value of the entire DEM. The script then removes this vertical difference (bias) on a column-by-column basis. Figure 4-6 A shows the resultant DEM after applying the derow procedure to the DEM of Figure 4-5 A. Figure 4-6 C and Figure 4-6D show the 1/e contour for the 3D ACF of the new DEM

and the correlation length as a function of the horizontal angle. It can be seen that the values of correlation length derived from the 3D formulation are within the same order of magnitude as the ones derived from the 2D formulation.

Comparison between 2D and 3D Roughness Parameter Values

Several analyses were performed to compare roughness parameter values of a surface considering profiles extracted from the DEMS and the DEMs as a whole. The procedure proposed in [15], which states that, to obtain a representative value of RMS_h that accounts for the heterogeneity of the surface, a minimum of 20 3-m transects should be acquired, was used as the baseline of the conventional profiling approach.

The following comparisons were performed:

- Oriented roughness, obtained by averaging values computed from all profiles extracted along the row or column directions with the values obtained from 20 random extracted profiles 3 m in length for the row or column directions.
- Full surface roughness, obtained by averaging values computed from all profiles extracted from the DEM with the values obtained from 20 random extracted profiles 3 m in length (10 extracted from the rows and 10 from the column direction).
- Full surface roughness, obtained by applying the 3D formulation from the DEMs with values obtained by averaging values computed from all profiles extracted, and from 20 random profiles 3-m in length (10 extracted from the rows and 10 from the columns direction).

Oriented roughness parameters were obtained by averaging values computed from profiles extracted along the rows and columns and detrending them with first order, second order, and FFT methods. These values are summarized in Table 4-2. The correlation coefficient and root mean square error (RMSE) comparing parameter values from a sample of 20 profiles with respect to all the profiles along the row or column directions are also presented at the bottom of Table 4-2. Results indicate a relatively good agreement between RMS_h values obtained from the sample and all extracted

profiles, with correlation coefficients higher than 0.89. The RMSE in the estimation of RMS_h using this sampling method was determined to be 3 mm for first order detrending, 2 mm for the second order detrending and 1 mm for the FFT-based detrending. In terms of correlation lengths, the correlation coefficients ranged from 0 to 0.89. The RMSE was 10–11.5 cm for first order detrending, 5.5–6.6 cm for second order detrending, and 1–2.4 cm for the FFT based detrending. This fairly large spread is due to the high sensitivity of the correlation length to the detrending procedure and the inherent high statistical variation observed for correlation lengths. It can be concluded that the sampling method proposed in [15] works well to produce a representative estimate of RMS_h values, but not so well for correlation lengths.

Values of 3D roughness parameters obtained by averaging results from 2D profiles and from the 3D formulation are summarized in Table 4-3, and results from their comparisons are presented in Table 4-4. When comparing averaged roughness parameter values derived from all the profiles with those obtained from 20 random profiles, results are similar to those obtained from the oriented roughness comparison described before. The correlation coefficients of RMS_h values were 0.94, 0.97, and 0.98 with a RMSE of 3, 2, and 1 mm for the first order, second order, and FFT based detrending method, respectively. The RMSE in the estimation of correlation lengths from the sample of 20 transects is 10.2, 6.0, and 1.4 cm for the different detrending methods. These results demonstrate the importance of applying the proper detrending method to obtain consistent values of correlation lengths.

Significant differences were found in the results of the third comparison, where parameter values derived from the 3D formulation and those obtained from averaging

values from 2D profiles were compared. Table 4-4 presents correlation coefficients, RMSE and percentage differences of the roughness parameters obtained from 2D and 3D formulations. Figure 4-7 shows dispersion plots for the RMS_h derived from the 3D model and that derived by averaging the values obtained from all the profiles and from a sample of 20 random profiles. Figure 4-8 shows dispersion plots of the derived correlation lengths from 3D and 2D formulations. It is evident that RMS_h values derived from profiles are significantly lower than the ones obtained from the 3D formulation. It was determined that if all the profiles extracted from the DEM were considered the RMS_h is underestimated on average by 27.5% independent of the detrending method used. The correlation length is also underestimated by between 27 and 35%.

The most important comparison is the one that considers the difference between digitizing the full surface and taking a sample of a few transects, as is the current practice for traditional field methods. From this comparison, it was found a considerable underestimation of the surface roughness parameters. Deriving RMS_h from profiles underestimates the surface RMS_h by: 15 to 63% with a mean of 37% for the first order detrending; 25 to 47% with a mean of 35% for second order detrending; and 10 to 36% with a mean of 25% for the FFT-based detrending. Differences were also found when comparing the mean correlation length obtained from the 3D formulation with respect to the averaged values obtained from profiles, especially for those obtained from the limited sample of 20 profiles. On average the correlation length can be underestimated by 64% if obtained from all the possible transects extracted from the 3D model and by 50% if obtained from a sample of 20 profiles detrended using first and second order detrending. If the sample profiles are detrended using the FFT-based filter, the

underestimation of the correlation lengths is on average 33%. Part of this difference can be attributed to the fact that the first and second order detrending models do not completely remove the trend and thus higher values of correlation lengths are obtained. Although it is larger than the underestimation of RMS_h, the underestimation of the correlation lengths has less impact than the error related to RMS_h. This is because sensitivity studies of the integral equation model (IEM) have shown that soil moisture retrieval is more sensitive to error in the parameterization of RMS_h than the correlation length by a factor of 10 [25]. The impact of the underestimation of the roughness parameters on microwave observations modeled with IEM is discussed in the next section.

Impact of Roughness Underestimation on Microwave Observables

The Integral Equation Model (IEM) [40] and the Advanced Integral Equation Model (A-IEM) [41] provide estimates of the backscattering coefficient and emissivity from a randomly rough dielectric surface. These models take as inputs the dielectric constant, RMS_h, correlation length, and correlation function of the surface; and microwave sensor parameters such as frequency, polarization and angle of incidence. For the mapping of soil moisture (dielectric constant) from microwave instrument signatures, these models are inverted using a variety of methods which include look-up tables, neural networks, least squares and iteration [25]. Performing a full sensitivity study of the inversion of IEM models to errors in roughness parameterization is extremely complicated because of the great number of combinations of input and output parameters. While this is beyond the scope of this research, the impact of roughness underestimation on scattering coefficient and brightness temperatures was modeled for a few scenarios. These scenarios were the combinations of three roughness states (3D RMS_h = 0.5, 1.5,

2.5 cm), two levels of volumetric soil moisture (7% and 20%), two frequencies (1.2 and 5.3 GHz), with four microwave observables (T_bH , T_bV , σ^0_{HH} and σ^0_{VV}), considering surfaces with exponential ACFs and an incidence angle of 40 degrees. Table 4-5 summarizes the differences in the microwave observables values due to errors in the parameterization of roughness from 2D profiles with respect to 3D DEMs.

The results indicate that the sensor configurations that are more sensitive to errors in roughness parameterization are the radiometers that observe the surface in horizontal polarization irrespective of their band of operation, and radars that operate in L-band that transmit and receive in horizontal polarization. Differences in brightness temperature in the horizontal polarization of up to 4.2 kelvin can be observed due to roughness underestimation under conditions of low soil moisture (7% by volume) and of up to 7 kelvin for high soil moisture levels (20%). In terms of scattering coefficients, the largest difference was observed for the HH polarization in the L band of 4.77 dB for low soil moisture and 4.58 dB for high soil moisture. Differences in the modeled brightness temperature in the vertical polarization also becomes significant at high roughness and high soil moisture conditions.

Advanced Detrending and Scale Separation Methods for 3D DEMs

In [42], microwave scattering and emission models for three types of surfaces are covered: purely random, purely periodic, and random superimposed over a periodic pattern. However, it is possible to encounter surfaces that exhibit random components superimposed over a quasi-periodic or non-stationary surface. The key problem is how to separate the random and reference components of such a surface. When traditional profiling methods are used, the approach is to only take transects along the row direction and consider this the random roughness, and the roughness component

across the rows is referred as the oriented roughness [43]. For deriving roughness parameters from 3D models of quasi-periodic surfaces, three approaches were tried:

- Extracting all the along-row profiles from the DEM, and processing each individually, then averaging the results
- Generating a new DEM by extracting every profile along the column direction of the DEM and removing its vertical bias with respect to the entire surface mean height.
- Generating a new DEM using a five stage wavelet bank to decompose the DEM in vertical, horizontal, and diagonal detail at different scales, then synthesizing a new DEM by removing the vertical detail at scales comparable to the row structure.

Wavelets are the foundation of multi-resolution analysis, which is an extension of Fourier analysis. Fourier analysis only provides spectral information from temporal or spatial information while wavelet analysis provides spectral and temporal or spectral and spatial information simultaneously [54]. Wavelets decompose a signal into approximation and detail components at multiple scales. Figure 4-9 illustrates a two stage 2D wavelet decomposition bank used to decompose a 3D DEM. At the top of the figure is the original DEM. This original dataset is considered to be at scale 0. The data at scale 0 is then decomposed into four components: the level 1 approximation and the horizontal, vertical, and diagonal details. Each component is $\frac{1}{4}$ the size of the original scale. To obtain the components at the second scale, the approximation at scale 1 is again decomposed into the four elements. This decomposition process can be repeated until the components of the last scale have only 1 pixel. After decomposition, a new DEM at the original scale can be synthesized by inverting the process starting from the large scales and modifying or removing particular components at specific scales. To extract the 3D random component of quasi-periodic surfaces, the random component

DEM was synthesized by removing the vertical detail at scales comparable to the row structure.

Figure 4-10 shows an example of detrending a quasi-periodic surface using the vertical bias removal and the wavelet method. Values of roughness parameters obtained from the random component that was extracted using the different quasi-periodic detrending methods are presented in Table 4-6. It can be seen that the resulting RMS_h are comparable to each other independent of the detrending method, not so for the correlation lengths where the traditional method and the vertical bias removal closely agree, but the wavelet detrending method produces lower correlation values.

Chapter Conclusions

The most important conclusion derived from the analyses presented in this chapter is that characterizing roughness from 3D datasets provides a much better description than those obtained with the traditional 2D profiling methods. The multi-scale nature of agricultural soils and natural surfaces becomes much more evident from 3D data, thus it is important to apply advanced detrending methods to characterize roughness at a particular scale. 3D models have the resolution and extent necessary to properly separate the height random component from the reference surface using such advanced detrending techniques as FFT filters or wavelet decomposition. 3D models also allow for the characterization of roughness heterogeneity and directional properties.

This study demonstrated that roughness parameters obtained from a limited number of transects underestimates the roughness of the full surface. On average, RMS_h is underestimated by 25% and correlation lengths by 30%. This is due mainly to

2 reasons: it is unlikely that a single profile will record the extremes of the surface, and trends derived from a single profile might not be representative of the general surface trend. Simulations using IEM indicate that these errors in parameterization can cause errors in modeled scattering coefficients of up to 4.77 dB for the HH polarization, and in the modeled brightness temperatures of up to 7 kelvin for the H polarization.

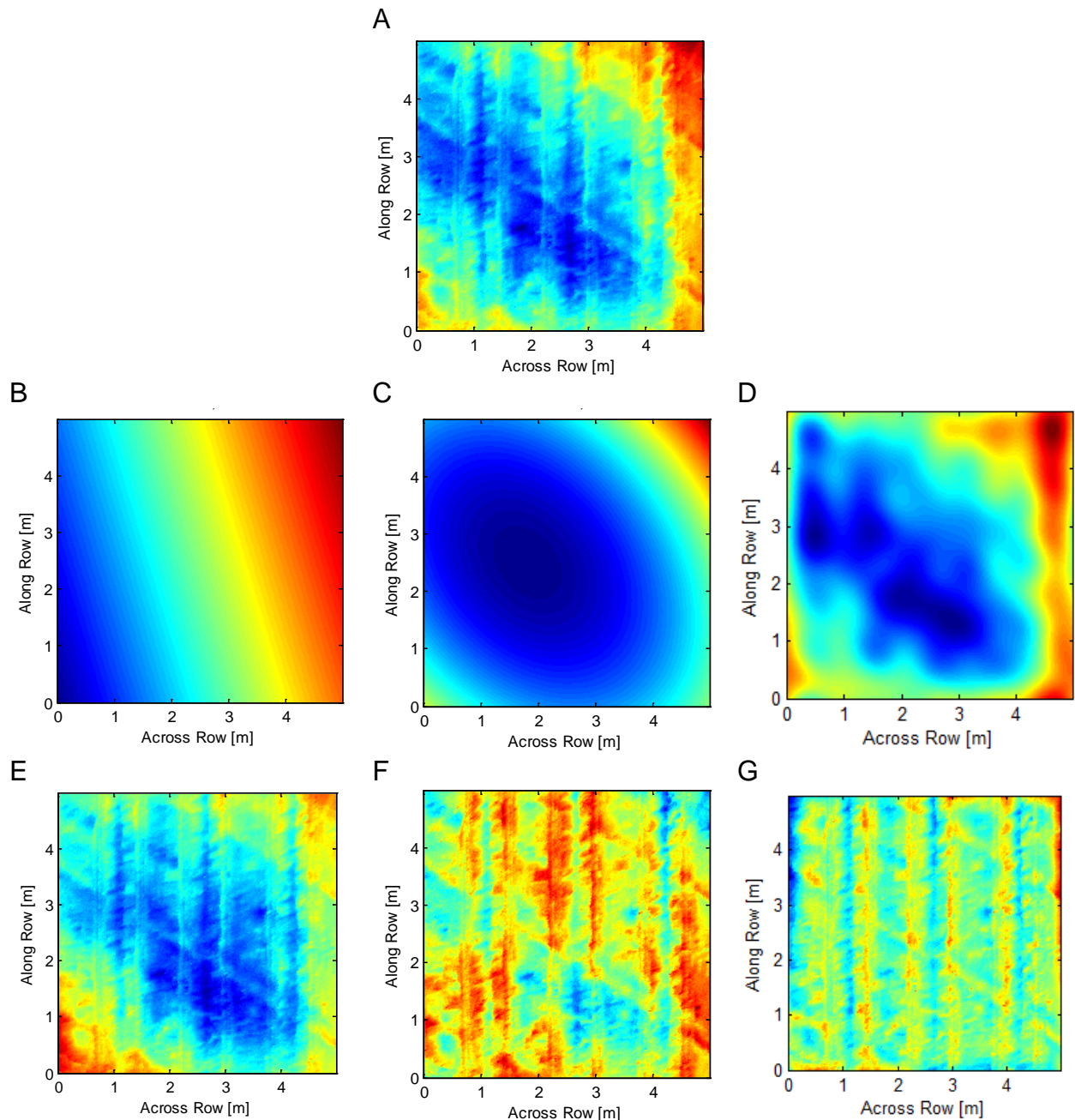


Figure 4-1. Detrending a 3D DEM with linear, quadratic models and a FFT low pass filter.

A) Original DEM. B) Linear trend, $R^2 = 0.2755$. C) Quadratic trend, $R^2 = 0.8108$. D) FFT trend, $R^2 = 0.8685$. E) Random height component after linear detrending, RMS_h = 1.8 cm. F) Random height component after quadratic detrending, RMS_h = 0.08 cm. G) Random height component after FFT based filtering, RMS_h = 0.07 cm.

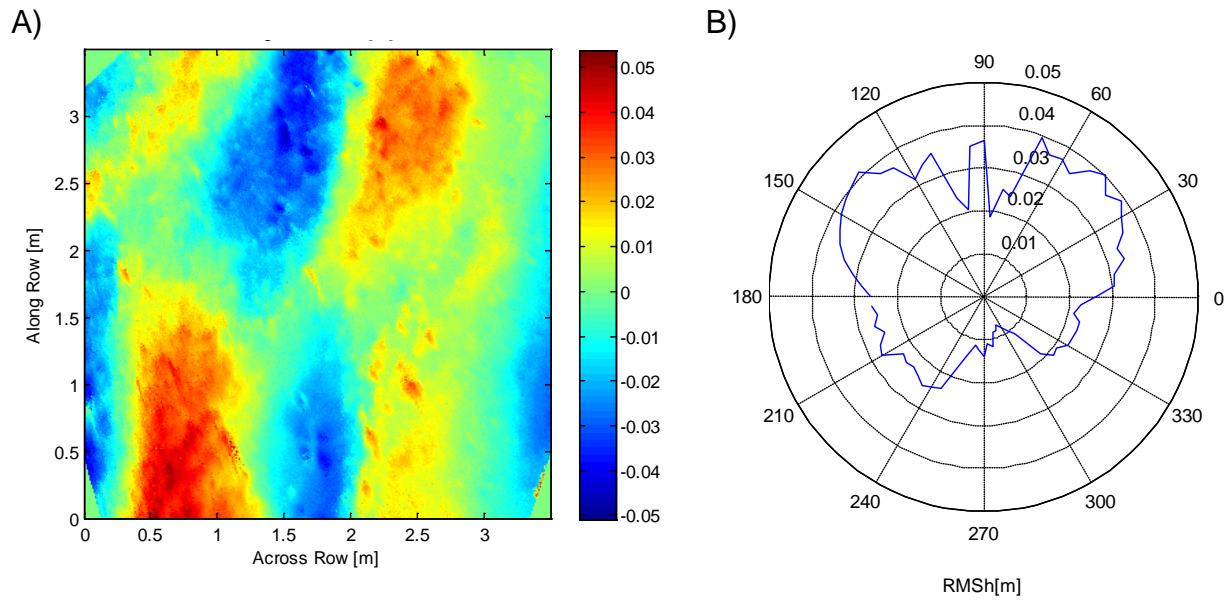


Figure 4-2. Directional roughness.

A) First order detrended DEM. B) RMSh as a function of the angle from a horizontal axis with origin at the center of the grid.

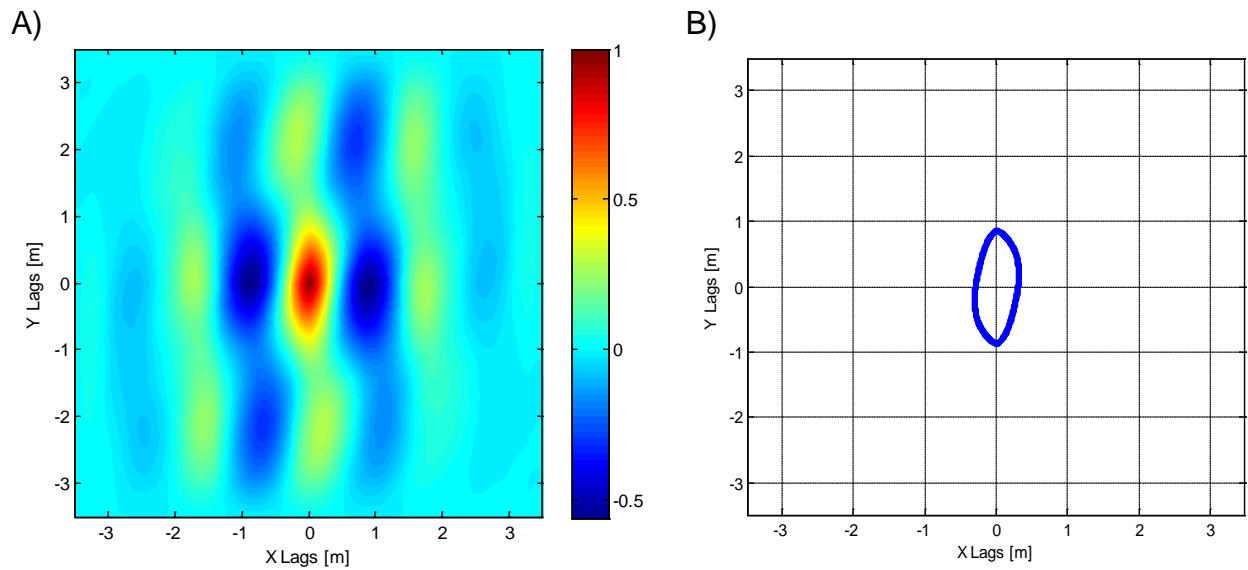


Figure 4-3. Deriving 3D correlation length A) 3D ACF from DEM in Figure 4-2 A. B) The extracted 1/e contour from the 3D autocorrelation function.

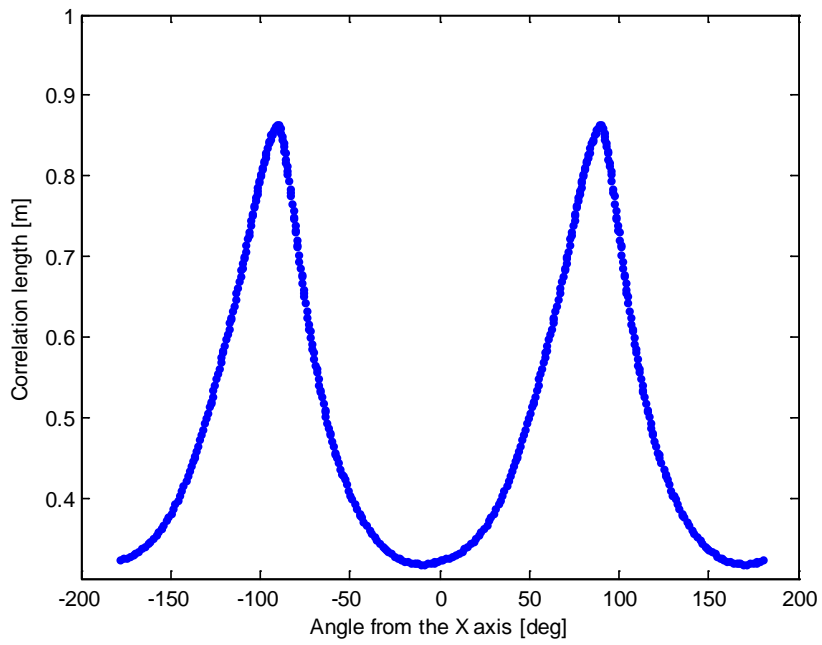


Figure 4-4. 3D correlation length as a function of the horizontal angle.

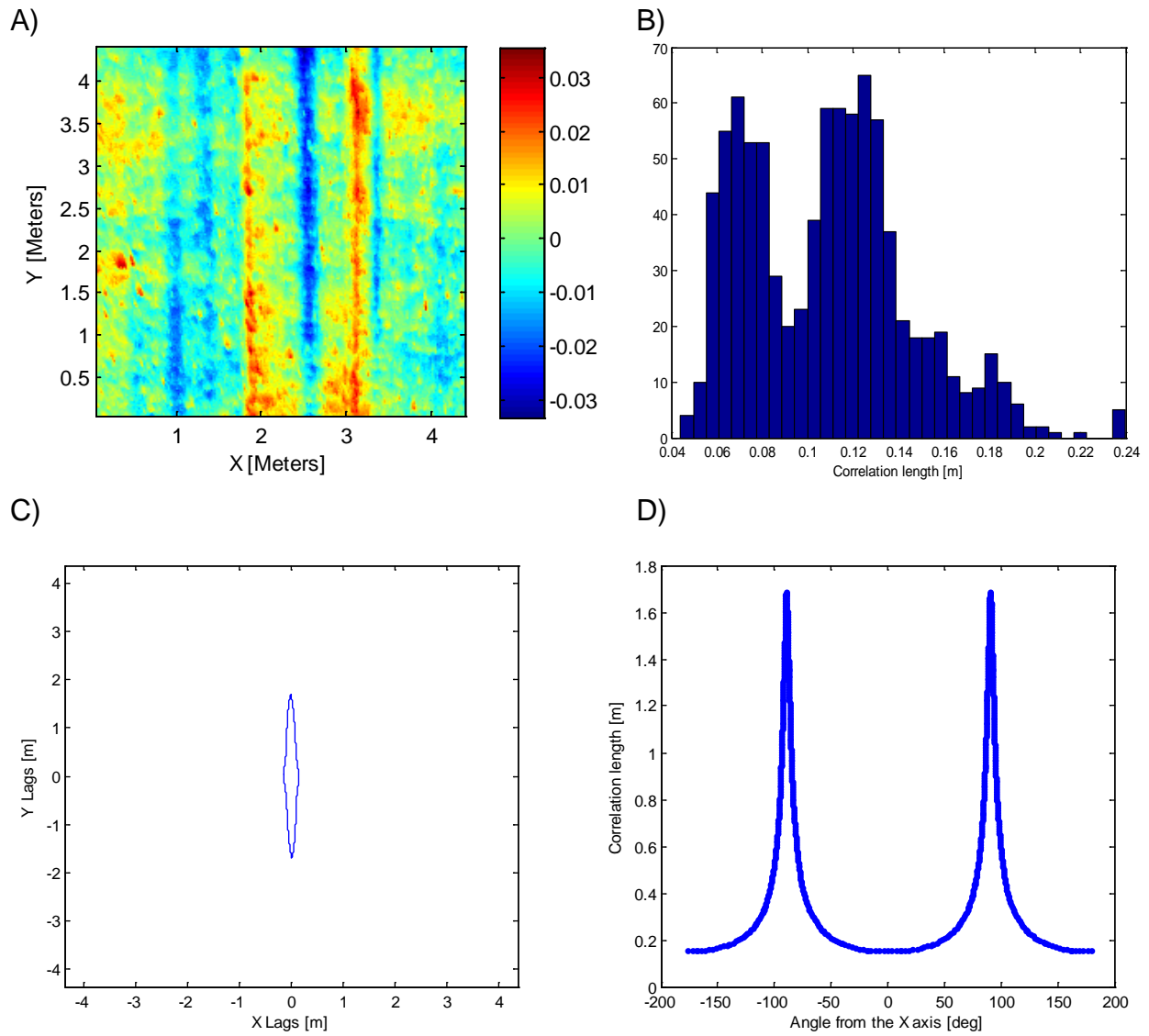


Figure 4-5. 3D Correlation length of a DEM with linear features.

A) Detrended DEM. B) Distribution of correlation lengths obtained from the 2D formulation. C) The extracted 1/e contour from the 3D ACF. D) 3D correlation length as a function of the horizontal angle.

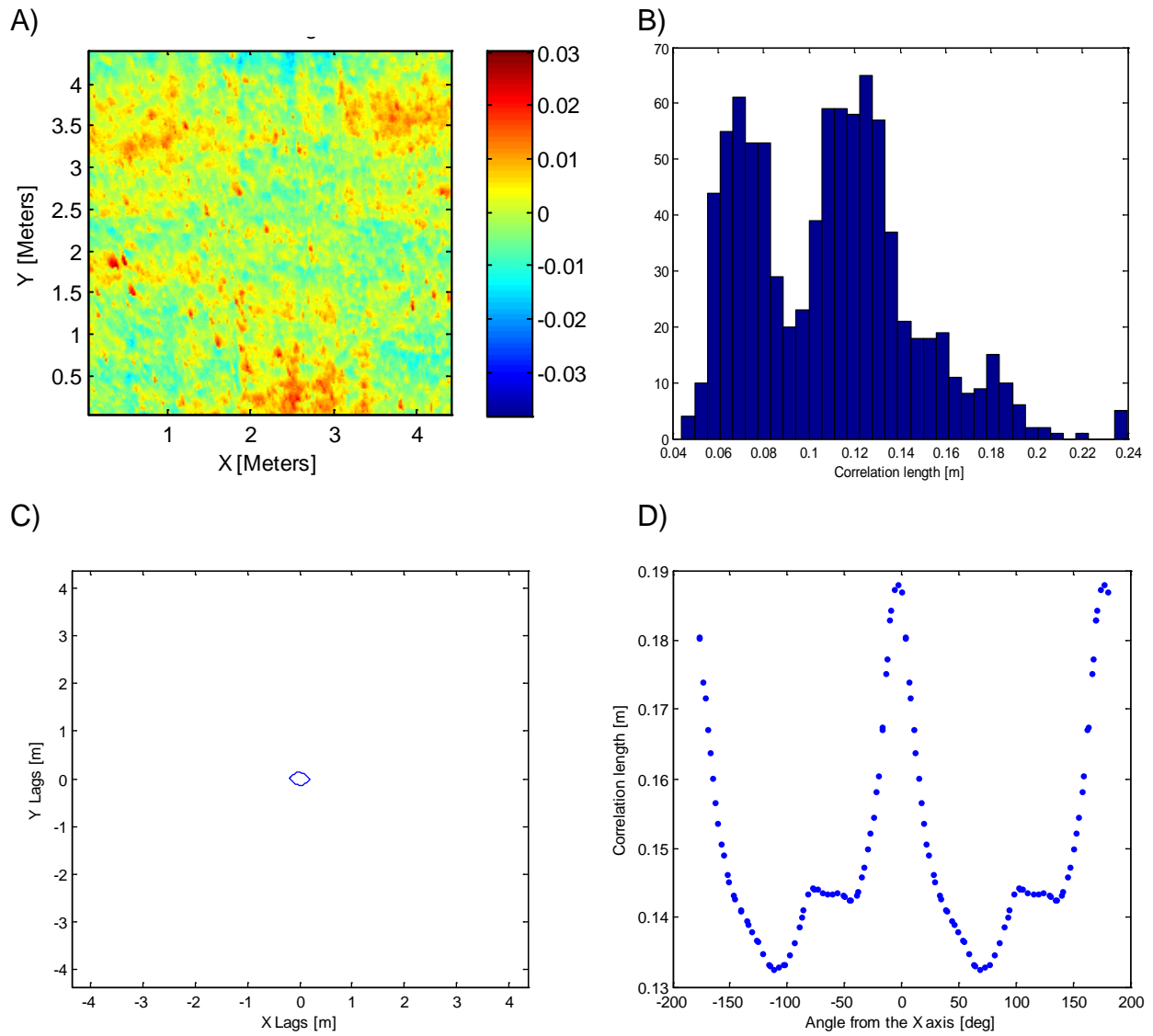


Figure 4-6. 3D Correlation length of a DEM after removing the linear features.

A) Detrended and de-rowsed DEM. B) Distribution of correlation lengths obtained from the 2D formulation. C) The extracted 1/e contour from the 3D ACF. D) 3D correlation length as a function of the horizontal angle.

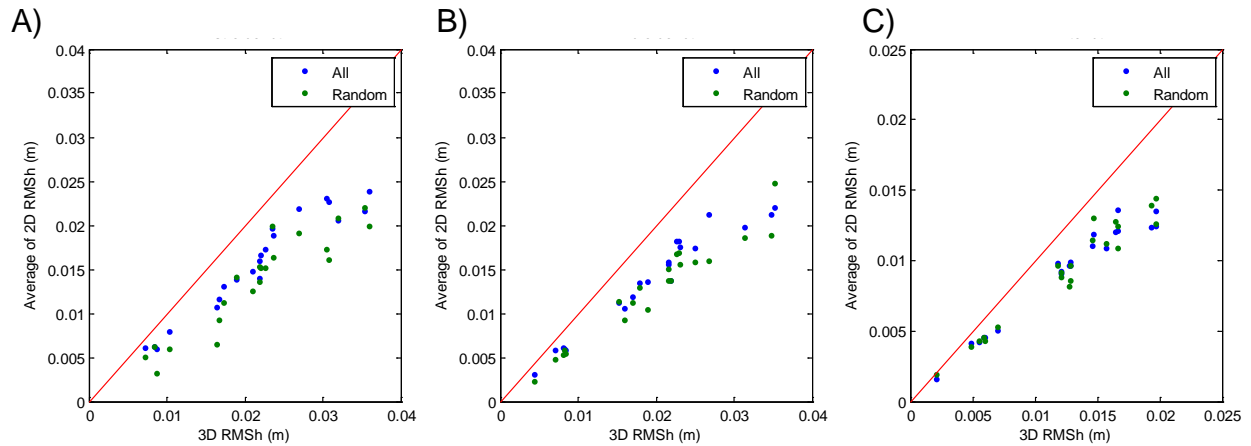


Figure 4-7. Dispersion plots of the 3D RMSh and the averaged values of RMSh derived from profiles

A) First order detrending, B) second order detrending, and C) FFT filter detrending.

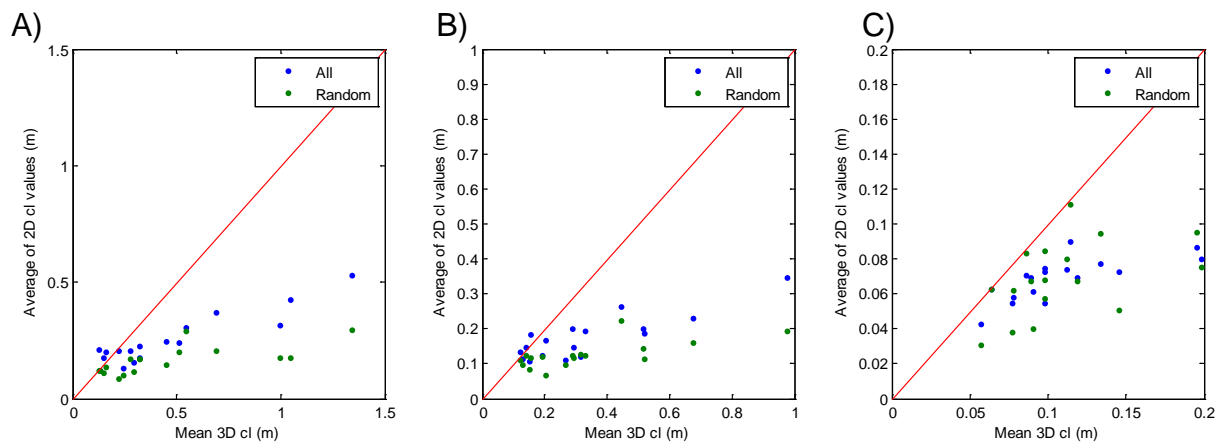


Figure 4-8. Dispersion plots of the averaged 3D correlation lengths and the averaged from profiles

A) First order detrending, B) second order detrending, and C) FFT filter detrending.

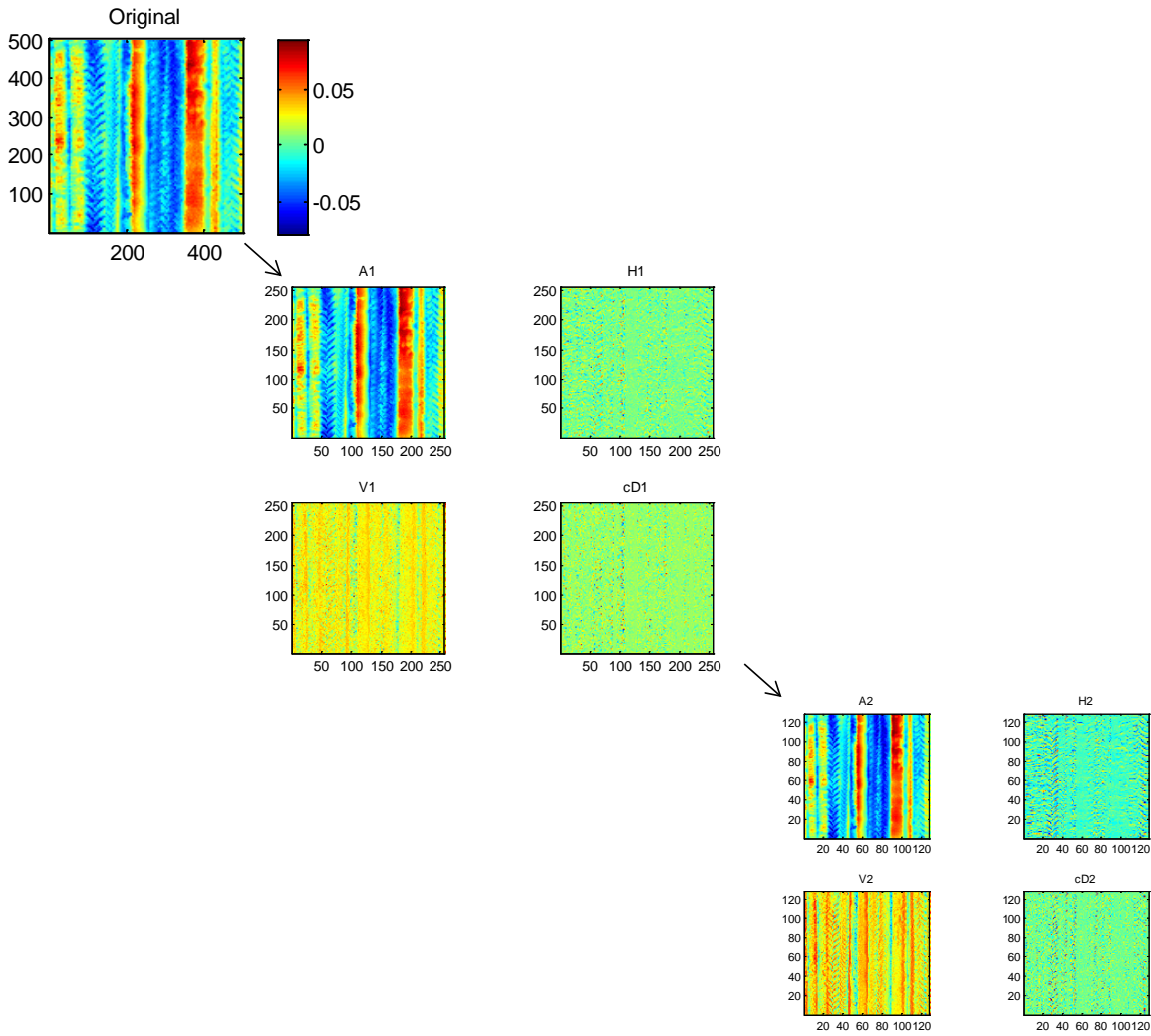


Figure 4-9. Two stage wavelet bank used to decompose a 3D DEM.

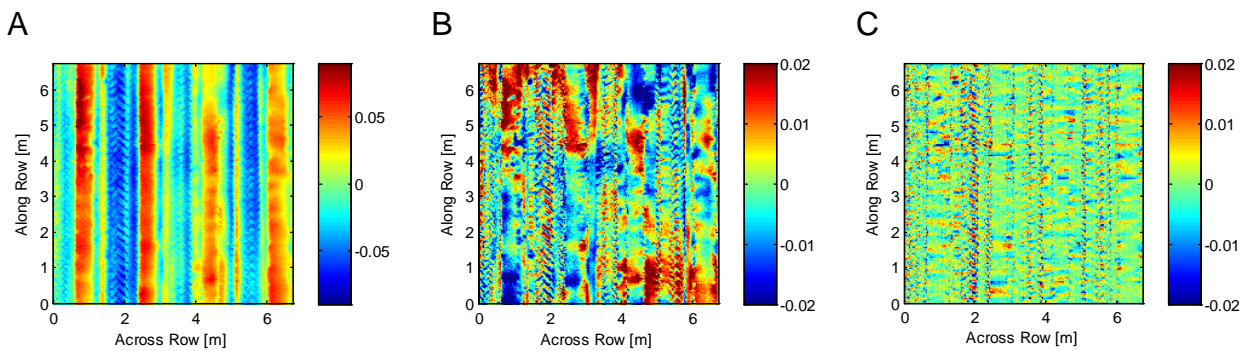


Figure 4-10. Detrending of a quasi-periodic surface (#20). A) Original DEM. B) Random component extracted using vertical bias removal. C) Random component extracted using wavelets.

Table 4- 1. Correlation coefficient and RMSE in meters between correlation length values derived by averaging profile values and averaging the ACFs.

| | First order | | Second order | | FFT Filter | |
|---------|-------------|-------|--------------|-------|------------|-------|
| | Cc | RMSE | cc | RMSE | cc | RMSE |
| Rows | 0.976 | 0.029 | 0.992 | 0.011 | 0.995 | 0.002 |
| Columns | 0.990 | 0.028 | 0.985 | 0.021 | 0.973 | 0.005 |

Table 4-2. Averaged oriented roughness parameter values obtained from 2D profiles extracted from the DEMs.

| First order detrending | | | | | | | | | |
|------------------------|--------|--------------------|--------|---------|--------------------|-------|--------|-------|-------|
| DEM # | Rows | | | Columns | | | | | |
| | RMSH | Correlation length | | RMSH | Correlation length | | IRMSH | | |
| | All | Rand | All | Rand | All | Rand | All | Rand | |
| 1 | 0.007 | 0.005 | 0.228 | 0.112 | 0.006 | 0.005 | 0.181 | 0.124 | 0.853 |
| 2 | 0.008 | 0.008 | 0.148 | 0.124 | 0.005 | 0.004 | 0.113 | 0.071 | 0.578 |
| 3 | 0.007 | 0.003 | 0.516 | 0.275 | 0.005 | 0.004 | 0.543 | 0.323 | 0.818 |
| 4 | 0.008 | 0.007 | 0.173 | 0.093 | 0.008 | 0.005 | 0.316 | 0.161 | 0.958 |
| 5 | 0.012 | 0.007 | 0.365 | 0.148 | 0.010 | 0.005 | 0.491 | 0.178 | 0.861 |
| 6 | 0.015 | 0.015 | 0.282 | 0.299 | 0.008 | 0.006 | 0.327 | 0.291 | 0.511 |
| 7 | 0.014 | 0.014 | 0.185 | 0.167 | 0.012 | 0.009 | 0.126 | 0.064 | 0.819 |
| 8 | 0.017 | 0.016 | 0.163 | 0.115 | 0.011 | 0.011 | 0.192 | 0.223 | 0.676 |
| 9 | 0.020 | 0.014 | 0.321 | 0.150 | 0.009 | 0.008 | 0.099 | 0.081 | 0.459 |
| 10 | 0.021 | 0.022 | 0.150 | 0.148 | 0.010 | 0.010 | 0.090 | 0.082 | 0.489 |
| 11 | 0.021 | 0.018 | 0.190 | 0.145 | 0.013 | 0.010 | 0.268 | 0.171 | 0.625 |
| 12 | 0.019 | 0.018 | 0.218 | 0.184 | 0.016 | 0.015 | 0.200 | 0.163 | 0.817 |
| 13 | 0.022 | 0.024 | 0.201 | 0.185 | 0.017 | 0.012 | 0.281 | 0.181 | 0.752 |
| 14 | 0.023 | 0.018 | 0.230 | 0.152 | 0.015 | 0.015 | 0.127 | 0.123 | 0.679 |
| 15 | 0.026 | 0.021 | 0.278 | 0.198 | 0.018 | 0.018 | 0.130 | 0.109 | 0.710 |
| 16 | 0.029 | 0.022 | 0.421 | 0.237 | 0.017 | 0.015 | 0.317 | 0.225 | 0.597 |
| 17 | 0.023 | 0.022 | 0.197 | 0.152 | 0.023 | 0.013 | 0.440 | 0.208 | 0.986 |
| 18 | 0.022 | 0.022 | 0.084 | 0.084 | 0.006 | 0.006 | 0.109 | 0.116 | 0.295 |
| 19 | 0.032 | 0.032 | 0.189 | 0.181 | 0.010 | 0.009 | 0.095 | 0.085 | 0.303 |
| 20 | 0.035 | 0.034 | 0.216 | 0.182 | 0.008 | 0.007 | 0.210 | 0.132 | 0.241 |
| 21 | 0.032 | 0.033 | 0.174 | 0.170 | 0.016 | 0.014 | 0.359 | 0.273 | 0.505 |
| Cc | 0.962 | | 0.677 | | 0.891 | | 0.816 | | |
| RMSE | 0.003 | | 0.100 | | 0.003 | | 0.115 | | |
| $\Delta\%$ | -0.114 | | -0.241 | | -0.157 | | -0.263 | | |

Table 4-2. Continued

| Second order detrending | | | | | | | | | |
|-------------------------|--------|-------|--------------------|-------|---------|-------|--------------------|-------|-------|
| DEM # | Rows | | | | Columns | | | | IRMSh |
| | RMSh | | Correlation length | | RMSh | | Correlation length | | |
| | All | Rand | All | Rand | All | Rand | All | Rand | |
| 1 | 0.006 | 0.005 | 0.192 | 0.065 | 0.005 | 0.005 | 0.146 | 0.077 | 0.843 |
| 2 | 0.008 | 0.008 | 0.132 | 0.121 | 0.004 | 0.004 | 0.085 | 0.066 | 0.561 |
| 3 | 0.003 | 0.002 | 0.323 | 0.192 | 0.004 | 0.002 | 0.370 | 0.195 | 1.312 |
| 4 | 0.007 | 0.006 | 0.108 | 0.072 | 0.005 | 0.004 | 0.186 | 0.117 | 0.807 |
| 5 | 0.007 | 0.006 | 0.153 | 0.114 | 0.005 | 0.004 | 0.224 | 0.135 | 0.805 |
| 6 | 0.015 | 0.013 | 0.288 | 0.274 | 0.006 | 0.005 | 0.238 | 0.173 | 0.422 |
| 7 | 0.014 | 0.013 | 0.157 | 0.128 | 0.010 | 0.008 | 0.066 | 0.045 | 0.713 |
| 8 | 0.012 | 0.012 | 0.073 | 0.072 | 0.011 | 0.011 | 0.168 | 0.174 | 0.885 |
| 9 | 0.018 | 0.012 | 0.179 | 0.122 | 0.009 | 0.009 | 0.088 | 0.079 | 0.491 |
| 10 | 0.021 | 0.021 | 0.146 | 0.139 | 0.010 | 0.010 | 0.082 | 0.067 | 0.485 |
| 11 | 0.020 | 0.019 | 0.183 | 0.175 | 0.012 | 0.009 | 0.216 | 0.133 | 0.580 |
| 12 | 0.015 | 0.015 | 0.141 | 0.153 | 0.012 | 0.011 | 0.111 | 0.109 | 0.771 |
| 13 | 0.022 | 0.023 | 0.191 | 0.176 | 0.015 | 0.011 | 0.212 | 0.132 | 0.687 |
| 14 | 0.021 | 0.016 | 0.184 | 0.125 | 0.015 | 0.013 | 0.113 | 0.099 | 0.699 |
| 15 | 0.025 | 0.019 | 0.249 | 0.147 | 0.018 | 0.018 | 0.119 | 0.098 | 0.706 |
| 16 | 0.020 | 0.017 | 0.232 | 0.161 | 0.015 | 0.011 | 0.232 | 0.153 | 0.732 |
| 17 | 0.022 | 0.022 | 0.179 | 0.156 | 0.013 | 0.010 | 0.212 | 0.122 | 0.593 |
| 18 | 0.022 | 0.021 | 0.083 | 0.083 | 0.006 | 0.005 | 0.074 | 0.089 | 0.274 |
| 19 | 0.031 | 0.032 | 0.183 | 0.174 | 0.009 | 0.009 | 0.062 | 0.060 | 0.281 |
| 20 | 0.035 | 0.034 | 0.211 | 0.175 | 0.008 | 0.006 | 0.160 | 0.111 | 0.225 |
| 21 | 0.031 | 0.031 | 0.168 | 0.165 | 0.013 | 0.011 | 0.254 | 0.175 | 0.401 |
| Cc | 0.970 | | 0.737 | | 0.951 | | 0.893 | | |
| RMSE | 0.002 | | 0.054 | | 0.002 | | 0.066 | | |
| Δ% | -0.084 | | -0.182 | | -0.151 | | -0.241 | | |

Table 4-2. Continued

| FFT filter detrending | | | | | | | | | |
|-----------------------|--------|-------|--------------------|-------|---------|-------|--------------------|-------|-------|
| DEM # | Rows | | | | Columns | | | | IRMSH |
| | RMSH | | Correlation length | | RMSH | | Correlation length | | |
| | All | Rand | All | Rand | All | Rand | All | Rand | |
| 1 | 0.004 | 0.004 | 0.041 | 0.040 | 0.004 | 0.004 | 0.045 | 0.027 | 0.919 |
| 2 | 0.006 | 0.005 | 0.071 | 0.062 | 0.004 | 0.003 | 0.055 | 0.055 | 0.661 |
| 3 | 0.002 | 0.002 | 0.085 | 0.073 | 0.001 | 0.002 | 0.070 | 0.054 | 0.690 |
| 4 | 0.005 | 0.006 | 0.049 | 0.053 | 0.004 | 0.004 | 0.074 | 0.048 | 0.693 |
| 5 | 0.006 | 0.005 | 0.104 | 0.070 | 0.004 | 0.004 | 0.076 | 0.079 | 0.599 |
| 6 | 0.005 | 0.005 | 0.080 | 0.069 | 0.004 | 0.004 | 0.068 | 0.091 | 0.748 |
| 7 | 0.010 | 0.009 | 0.065 | 0.065 | 0.009 | 0.008 | 0.045 | 0.067 | 0.879 |
| 8 | 0.011 | 0.011 | 0.062 | 0.063 | 0.007 | 0.008 | 0.055 | 0.058 | 0.682 |
| 9 | 0.011 | 0.009 | 0.083 | 0.075 | 0.008 | 0.009 | 0.067 | 0.059 | 0.698 |
| 10 | 0.015 | 0.015 | 0.088 | 0.083 | 0.009 | 0.009 | 0.055 | 0.056 | 0.571 |
| 11 | 0.012 | 0.012 | 0.073 | 0.065 | 0.008 | 0.008 | 0.066 | 0.060 | 0.643 |
| 12 | 0.011 | 0.011 | 0.053 | 0.060 | 0.009 | 0.008 | 0.056 | 0.069 | 0.839 |
| 13 | 0.013 | 0.013 | 0.075 | 0.069 | 0.009 | 0.009 | 0.085 | 0.064 | 0.687 |
| 14 | 0.012 | 0.012 | 0.081 | 0.079 | 0.012 | 0.011 | 0.057 | 0.091 | 0.954 |
| 15 | 0.013 | 0.013 | 0.079 | 0.072 | 0.014 | 0.014 | 0.067 | 0.050 | 1.013 |
| 16 | 0.012 | 0.011 | 0.096 | 0.089 | 0.008 | 0.009 | 0.078 | 0.088 | 0.700 |
| 17 | 0.015 | 0.015 | 0.079 | 0.074 | 0.009 | 0.009 | 0.067 | 0.094 | 0.612 |
| 18 | 0.020 | 0.020 | 0.074 | 0.074 | 0.005 | 0.006 | 0.038 | 0.078 | 0.273 |
| 19 | 0.019 | 0.020 | 0.088 | 0.092 | 0.008 | 0.007 | 0.039 | 0.097 | 0.399 |
| 20 | 0.019 | 0.021 | 0.088 | 0.085 | 0.006 | 0.006 | 0.046 | 0.090 | 0.299 |
| 21 | 0.014 | 0.012 | 0.075 | 0.067 | 0.008 | 0.008 | 0.074 | 0.054 | 0.560 |
| Cc | 0.986 | | 0.836 | | 0.983 | | -0.087 | | |
| RMSE | 0.001 | | 0.010 | | 0.001 | | 0.024 | | |
| Δ% | -0.040 | | -0.059 | | -0.008 | | - | | |

Table 4-3. 3D roughness parameters values obtained from the full DEM and averaging values obtained from 2D profiles.

| First order detrending | | | | | | | | | |
|-------------------------|----------------------|-------|--------|-------|--------|------------------------|--------|-------|--------|
| # | RMS _h [m] | | | | Eccent | Correlation length [m] | | | |
| | 3D | All | Random | m Dir | | 3D min | 3Dmean | All | Random |
| 1 | 0.007 | 0.006 | 0.005 | 0.006 | 0.940 | 0.294 | 0.223 | 0.205 | 0.087 |
| 2 | 0.008 | 0.006 | 0.006 | 0.008 | 0.944 | 0.158 | 0.242 | 0.131 | 0.103 |
| 3 | 0.009 | 0.006 | 0.003 | 0.007 | 0.949 | 0.678 | 1.339 | 0.530 | 0.298 |
| 4 | 0.010 | 0.008 | 0.006 | 0.007 | 0.938 | 0.289 | 0.450 | 0.245 | 0.147 |
| 5 | 0.016 | 0.011 | 0.007 | 0.011 | 0.967 | 0.686 | 1.046 | 0.428 | 0.177 |
| 6 | 0.017 | 0.012 | 0.009 | 0.009 | 0.984 | 0.318 | 0.541 | 0.305 | 0.293 |
| 7 | 0.017 | 0.013 | 0.011 | 0.014 | 0.938 | 0.175 | 0.292 | 0.156 | 0.119 |
| 8 | 0.019 | 0.014 | 0.014 | 0.015 | 0.950 | 0.190 | 0.322 | 0.177 | 0.170 |
| 9 | 0.021 | 0.015 | 0.013 | 0.016 | 0.977 | 0.305 | 0.127 | 0.210 | 0.123 |
| 10 | 0.022 | 0.016 | 0.015 | 0.019 | 0.977 | 0.152 | 0.130 | 0.120 | 0.123 |
| 11 | 0.022 | 0.017 | 0.015 | 0.020 | 0.931 | 0.219 | 0.318 | 0.229 | 0.174 |
| 12 | 0.023 | 0.017 | 0.015 | 0.017 | 0.970 | 0.310 | 0.277 | 0.209 | 0.172 |
| 13 | 0.024 | 0.020 | 0.020 | 0.020 | 0.976 | 0.207 | 0.509 | 0.241 | 0.200 |
| 14 | 0.024 | 0.019 | 0.016 | 0.022 | 0.968 | 0.235 | 0.149 | 0.178 | 0.114 |
| 15 | 0.027 | 0.022 | 0.019 | 0.022 | 0.938 | 0.288 | 0.158 | 0.204 | 0.135 |
| 16 | 0.030 | 0.023 | 0.017 | 0.025 | 0.971 | 0.473 | 0.691 | 0.369 | 0.206 |
| 17 | 0.031 | 0.023 | 0.016 | 0.024 | 0.912 | 0.391 | 0.993 | 0.319 | 0.178 |
| 18 | 0.022 | 0.014 | 0.014 | 0.022 | 0.988 | 0.085 | 0.130 | 0.097 | 0.090 |
| 19 | 0.032 | 0.021 | 0.021 | 0.029 | 0.988 | 0.191 | 0.081 | 0.142 | 0.125 |
| 20 | 0.035 | 0.022 | 0.022 | 0.032 | 0.988 | 0.220 | 0.251 | 0.213 | 0.150 |
| 21 | 0.036 | 0.024 | 0.020 | 0.027 | 0.981 | 0.185 | 0.361 | 0.267 | 0.210 |
| Second order detrending | | | | | | | | | |
| # | RMS _h [m] | | | | Eccent | Correlation length [m] | | | |
| | 3D | All | Random | m Dir | | 3D min | 3Dmean | All | Random |
| 1 | 0.007 | 0.006 | 0.005 | 0.006 | 0.934 | 0.288 | 0.203 | 0.169 | 0.069 |
| 2 | 0.008 | 0.006 | 0.006 | 0.008 | 0.961 | 0.153 | 0.151 | 0.109 | 0.086 |
| 3 | 0.004 | 0.003 | 0.002 | 0.003 | 0.982 | 0.438 | 0.975 | 0.347 | 0.193 |
| 4 | 0.008 | 0.006 | 0.005 | 0.006 | 0.948 | 0.165 | 0.290 | 0.147 | 0.118 |
| 5 | 0.008 | 0.006 | 0.005 | 0.006 | 0.914 | 0.226 | 0.519 | 0.188 | 0.116 |
| 6 | 0.016 | 0.011 | 0.009 | 0.009 | 0.988 | 0.296 | 0.446 | 0.263 | 0.225 |
| 7 | 0.017 | 0.012 | 0.011 | 0.014 | 0.932 | 0.169 | 0.267 | 0.111 | 0.097 |
| 8 | 0.015 | 0.011 | 0.011 | 0.014 | 0.959 | 0.113 | 0.314 | 0.120 | 0.129 |
| 9 | 0.019 | 0.014 | 0.011 | 0.015 | 0.977 | 0.180 | 0.119 | 0.133 | 0.110 |
| 10 | 0.022 | 0.016 | 0.015 | 0.019 | 0.976 | 0.151 | 0.127 | 0.114 | 0.099 |
| 11 | 0.022 | 0.016 | 0.014 | 0.020 | 0.930 | 0.207 | 0.290 | 0.200 | 0.123 |
| 12 | 0.018 | 0.013 | 0.013 | 0.016 | 0.948 | 0.202 | 0.190 | 0.126 | 0.121 |
| 13 | 0.023 | 0.018 | 0.017 | 0.020 | 0.974 | 0.196 | 0.515 | 0.202 | 0.145 |
| 14 | 0.023 | 0.018 | 0.017 | 0.020 | 0.961 | 0.197 | 0.140 | 0.148 | 0.123 |
| 15 | 0.027 | 0.021 | 0.016 | 0.022 | 0.939 | 0.271 | 0.154 | 0.184 | 0.119 |
| 16 | 0.023 | 0.018 | 0.016 | 0.021 | 0.955 | 0.259 | 0.674 | 0.232 | 0.162 |
| 17 | 0.025 | 0.017 | 0.016 | 0.023 | 0.914 | 0.222 | 0.328 | 0.195 | 0.125 |
| 18 | 0.022 | 0.014 | 0.014 | 0.022 | 0.991 | 0.084 | 0.127 | 0.079 | 0.082 |
| 19 | 0.031 | 0.020 | 0.019 | 0.029 | 0.988 | 0.185 | 0.077 | 0.122 | 0.101 |
| 20 | 0.035 | 0.021 | 0.019 | 0.032 | 0.991 | 0.212 | 0.187 | 0.185 | 0.108 |
| 21 | 0.035 | 0.022 | 0.025 | 0.027 | 0.985 | 0.179 | 0.357 | 0.211 | 0.171 |

Table 4.3 Continued

| FFT based filter | | | | | | | | | |
|------------------|----------------------|-------|--------|-------|--------|------------------------|--------|-------|--------|
| # | RMS _h [m] | | | | Eccent | Correlation length [m] | | | |
| | 3D | All | Random | m Dir | | 3D min | 3Dmean | All | Random |
| 1 | 0.005 | 0.004 | 0.004 | 0.007 | 0.891 | 0.060 | 0.057 | 0.043 | 0.031 |
| 2 | 0.006 | 0.005 | 0.005 | 0.008 | 0.938 | 0.081 | 0.063 | 0.063 | 0.063 |
| 3 | 0.002 | 0.002 | 0.002 | 0.003 | 0.944 | 0.131 | 0.134 | 0.077 | 0.095 |
| 4 | 0.006 | 0.005 | 0.004 | 0.008 | 0.884 | 0.074 | 0.090 | 0.061 | 0.040 |
| 5 | 0.007 | 0.005 | 0.005 | 0.008 | 0.923 | 0.123 | 0.114 | 0.090 | 0.112 |
| 6 | 0.006 | 0.004 | 0.004 | 0.007 | 0.948 | 0.099 | 0.112 | 0.074 | 0.080 |
| 7 | 0.012 | 0.009 | 0.009 | 0.015 | 0.889 | 0.082 | 0.098 | 0.055 | 0.057 |
| 8 | 0.012 | 0.009 | 0.009 | 0.020 | 0.953 | 0.073 | 0.078 | 0.058 | 0.062 |
| 9 | 0.013 | 0.010 | 0.008 | 0.020 | 0.957 | 0.097 | 0.098 | 0.075 | 0.085 |
| 10 | 0.016 | 0.012 | 0.013 | 0.027 | 0.970 | 0.096 | 0.086 | 0.071 | 0.084 |
| 11 | 0.013 | 0.010 | 0.010 | 0.018 | 0.886 | 0.084 | 0.119 | 0.070 | 0.068 |
| 12 | 0.012 | 0.010 | 0.010 | 0.018 | 0.933 | 0.069 | 0.077 | 0.055 | 0.038 |
| 13 | 0.015 | 0.011 | 0.012 | 0.021 | 0.960 | 0.089 | 0.198 | 0.080 | 0.075 |
| 14 | 0.015 | 0.012 | 0.013 | 0.026 | 0.955 | 0.090 | 0.089 | 0.069 | 0.068 |
| 15 | 0.017 | 0.014 | 0.013 | 0.023 | 0.897 | 0.088 | 0.098 | 0.073 | 0.068 |
| 16 | 0.013 | 0.010 | 0.009 | 0.018 | 0.915 | 0.096 | 0.196 | 0.087 | 0.095 |
| 17 | 0.017 | 0.012 | 0.011 | 0.021 | 0.890 | 0.096 | 0.145 | 0.073 | 0.051 |
| 18 | 0.020 | 0.012 | 0.013 | 0.033 | 0.988 | 0.074 | 0.073 | 0.056 | 0.074 |
| 19 | 0.020 | 0.014 | 0.014 | 0.025 | 0.979 | 0.090 | 0.052 | 0.063 | 0.093 |
| 20 | 0.019 | 0.012 | 0.014 | 0.028 | 0.982 | 0.090 | 0.067 | 0.067 | 0.084 |
| 21 | 0.016 | 0.011 | 0.011 | 0.019 | 0.933 | 0.088 | 0.184 | 0.075 | 0.074 |

Table 4-4. Comparison of 3D roughness parameter values obtained from different approaches.

| | First order detrending | | | Second order detrending | | | FFT based detrending | | |
|-----------------------------|------------------------|-------|---------|-------------------------|-------|---------|----------------------|-------|---------|
| | CC | RMSE | Mean %Δ | CC | RMSE | mean %Δ | cc | RMSE | mean %D |
| RMSh, all profiles – 20 rnd | 0.94 | 0.003 | -14.0 | 0.97 | 0.002 | -9.1 | 0.98 | 0.001 | 0.4 |
| l, all profiles - 20 random | 0.78 | 0.102 | -27.5 | 0.80 | 0.060 | -23.6 | 0.76 | 0.014 | 3.2 |
| RMSh, 3D - all profiles | 0.97 | 0.007 | -26.8 | 0.97 | 0.007 | -28.0 | 0.98 | 0.004 | -25.0 |
| l, 3D - all profiles | 0.93 | 0.329 | -27.4 | 0.85 | 0.236 | -34.5 | 0.72 | 0.051 | -32.1 |
| RMSh, 3D - 20 random | 0.93 | 0.009 | -37.0 | 0.97 | 0.008 | -34.8 | 0.97 | 0.004 | -24.8 |
| l, 3D - 20 random | 0.70 | 0.428 | -49.4 | 0.69 | 0.288 | -50.9 | 0.48 | 0.053 | -33.3 |
| RMSh, 3D - mean directional | 0.97 | 0.004 | -18.2 | 0.98 | 0.003 | -14.8 | 0.98 | 0.001 | -10.0 |
| RMSh, 3D - max directional | 0.95 | 0.008 | 30.3 | 0.96 | 0.008 | 36.0 | 0.96 | 0.007 | 42.1 |

Table 4-5. Difference in microwave observables due to errors in roughness parameterization.

| | 3D | | 2D | | Low Soil Moisture: 7% by volume | | | | High soil moisture: 20% by volume | | | |
|---|------|----|------|---|---------------------------------|-------------|--------------------|--------------------|-----------------------------------|-------------|--------------------|--------------------|
| | RMSh | l | RMSh | l | $T_b h$ [k] | $T_b v$ [k] | $\sigma_0 hh$ [dB] | $\sigma_0 vv$ [dB] | $T_b h$ [k] | $T_b v$ [k] | $\sigma_0 hh$ [dB] | $\sigma_0 vv$ [dB] |
| L | 0.5 | 10 | 0.4 | 7 | -0.02 | 0.18 | -0.49 | -0.95 | -0.06 | 0.25 | -1.55 | -0.95 |
| | 1.5 | 10 | 1.1 | 7 | -2.92 | 0.07 | -4.77 | -1.60 | -4.77 | -0.99 | -4.58 | -1.62 |
| | 2.5 | 10 | 1.9 | 7 | -4.26 | -1.79 | -4.05 | -1.14 | -7.18 | -4.39 | -4.20 | -1.17 |
| C | 0.5 | 10 | 0.4 | 7 | -0.02 | 0.18 | -2.09 | -0.39 | -0.06 | 0.25 | -2.10 | -0.42 |
| | 1.5 | 10 | 1.1 | 7 | -2.89 | 0.08 | -2.27 | -2.02 | -4.73 | -0.96 | -2.31 | -1.26 |
| | 2.5 | 10 | 1.9 | 7 | -4.22 | -1.76 | 0.07 | 0.07 | -7.12 | -4.32 | 0.04 | 0.22 |

Table 4-6. Roughness Parameters derived from 3D models of quasi-periodic surfaces.

| # | RMS _h (m) | | | Correlation Length (m) | | |
|----|----------------------|---------|---------|------------------------|---------|---------|
| | Cols | -V Bias | Wavelet | Cols | -V Bias | Wavelet |
| 21 | 0.016 | 0.024 | 0.006 | 0.359 | 0.361 | 0.060 |
| 18 | 0.006 | 0.008 | 0.005 | 0.109 | 0.130 | 0.028 |
| 19 | 0.009 | 0.011 | 0.007 | 0.095 | 0.081 | 0.037 |
| 20 | 0.008 | 0.010 | 0.006 | 0.21 | 0.251 | 0.035 |

CHAPTER 5 THE APPLICATION OF AIRBORNE LIDAR TO MAP SURFACE ROUGHNESS OF LARGE AREAS

As demonstrated in the previous chapters, ground-based LiDAR is a convenient and accurate tool to characterize millimeter-scale roughness. It is limited, however, to map areas that cover a few hundred square meters. Some applications require the characterization of surface roughness over much larger areas, such as the mapping of soil moisture at the watershed, regional, and global levels. To date, obtaining a good agreement between soil moisture measurements and results obtained from the inversion of physical-based models that use spaceborne microwave sensor observations and roughness measurements has been challenging [27], [28]. This may be due to the scaling of roughness measurements. These measurements are made *in situ* and cover a relatively small area, whereas the microwave sensor footprint can be up to several square kilometers in area.

The roughness measurements are scaled up under the assumption that roughness is isotropic and homogenous over the area of study. These sparse roughness datasets, in both the spatial and temporal domains, limit the applicability of inversion algorithms based on physical models, such as the IEM to retrieve soil moisture from microwave signatures using observations at satellite scales [26].

Airborne LiDAR observations have the potential to provide surface roughness characterization for large areas, as described in preliminary studies by Davenport et al. [20], [21]. These early experiments on the application of airborne LiDAR for surface roughness characterization were limited because of the decimeter accuracy of airborne LiDAR data, and the sparse sample densities obtainable by the technology of the late 1990s and early 2000s of one or two points per square meter. Since then, sensors and

algorithms have undergone exponential development and it is now possible to obtain sampling densities of tens of points per m^2 with sub-decimeter accuracy [30], [31].

Current capabilities of airborne LiDAR systems still do not allow for the fine sampling resolution required to determine cm-level correlation lengths. However, it is possible to derive RMS_h and studies, such as [27] and [38], have been aimed at deriving relationships between RMS_h and correlation lengths. This chapter explores methods to derive RMS_h maps of large areas using airborne LiDAR data.

Airborne LiDAR Instrumentation and Datasets

To properly describe some of the methods proposed in this chapter it is important to cover some basic aspects of the geometry of airborne LiDAR scanning. There are several airborne laser scanning mechanisms, the most common being an oscillating mirror. As illustrated in Figure 5-1, scanning from an airborne platform is performed in two dimensions. The first is accomplished by employing the forward motion of aircraft and the second is obtained using an oscillating mirror. The mirror steers the laser beam in a direction perpendicular to the line of flight. This mechanism distributes the laser pulses over the ground in a sawtooth pattern. The scanning angle and platform flight height determines the swath width. The scanning frequency in conjunction with PRF determines the across-track resolution. The aircraft ground speed and the scan frequency determines the down-track resolution. A survey is designed to meet specifications in terms of resolution, point density, and accuracy. This is achieved by modifying the PRF, scanning angle range and frequency, platform ground speed, and flying height. For a more detailed description of the basics of airborne LiDAR technology and terminology used in the following sections, the reader is referred to the papers by

Baltsavias [45] or Wehr and Lohr [46]. For descriptions of current capabilities and future technological developments the reader may refer to [30] and [31].

Data for this work was collected on September 2nd, 2010, employing an Optech Gemini Airborne LiDAR Terrain Mapper (ALTM) equipped with a waveform digitizer, owned and operated by the National Center for Airborne Laser Mapping (NCALM). The Gemini system is capable of pulse repetition rates of up to 166 kHz and can operate in multiple pulse mode which means that the system is able to fire a second laser pulse while still waiting for the return of the first. The Gemini uses a constant fraction discriminator to obtain up to four discrete returns for each outgoing pulse. An additional capability of the Gemini system is that it is possible to select between two beam divergence modes, a narrow divergence mode with full angle aperture of 0.25 mrad and the wide divergence mode with an aperture of 0.80 mrad. An add-on signal digitizer and computer allows for the sampling and recording of full waveform data. The ALTM detector output voltage is sampled at 1 GHz (every 1 nanosecond) and is quantized on an 8-bit scale between 0 and 1 volts. Detailed specifications for the Gemini ALTM and the waveform digitizer are presented in Tables 5-1 and 5-2; photographs of the full airborne system are shown in Figure 5-2.

The airborne LiDAR data collection was conducted over the grounds of the University of Florida Plant Science Research and Education Unit (PSREU), located near Citra, Florida. The general area that was mapped is shown in Figure 5-3A. This area was selected because of its heterogeneous composition which includes a variety of bare surfaces, vegetation with different characteristics, buildings, roads, and other manmade structures. Data collection was performed at a PRF of 70 kHz, which is the

maximum rate at which the waveform digitizer can operate, recording waveform information for every fired pulse. A single flight line was collected three times from a flying height of 600 meters above ground level varying the scan angle and beam divergence to test the effects of these adjustable sensor parameters on the ability to map small-scale roughness.

A summary of the main configuration parameters used for each line collection is presented in Table 5-3. One line was collected with a scan angle of $\pm 14^\circ$, a scan frequency of 60 Hz, and using narrow divergence mode. With these parameters, the swath width was 298.75 m, with a point density of 3.6 points/m², the cross-track resolution is 0.513 m, and the down-track resolution is 0.542 m. Two lines were collected with a scan angle of $\pm 5^\circ$ and a scan frequency of 65 Hz, one with narrow divergence and the second one in the wide beam mode. For these lines, the swath width was 104.56 m, with a point density of 10.26 points/m², the cross-track resolution was 0.195 m and the down-track resolution was 0.5 m. From a flying height of 600 m, at nadir, the laser footprint in the narrow divergence mode is 15 cm and using the wide divergence mode is 48 cm. Figure 5-3B shows a rendering from the swath collected from 600 meters AGL with $\pm 14^\circ$ scan angle. The rendering is color coded by elevation, with cool colors for low elevations and warm colors for high elevations. The luminance of the color is modulated by the intensity of the return signal.

Two data products were produced by NCALM from the airborne survey. The first processed data product from the ALTM is the point cloud that contains the UTM coordinates (easting northing and ellipsoid height), intensity, echo type, range scan angle, and GPS time for each collected return. The point clouds were delivered in two

formats, the binary ASPRS .LAS format and an ASCII multi-column text format. The second data product was the recorded raw binary waveform in the Optech proprietary NDF format. This raw waveform data consists of 8 bit-scaled signal voltage sampled every nanosecond for the outgoing pulse and the return waveform. Both of these data products were used to develop the roughness maps.

To create roughness maps, three different methods based on two approaches were proposed. The first approach is thematic mapping, which consists of attributing a roughness value (RMS_h) to each element in the point cloud. This approach was used on the first two methods: profiling from a single scan line and the footprint scale roughness from return waveform analysis. The second approach consists of creating an array with pixel elements that cover a given area, then grouping the individual points to a corresponding pixel element and computing the RMS_h for the group. Each method and its respective results is described next.

Profiles from a Single Scan Line

Davenport et al. in [20] and [21] demonstrated that despite the decimeter accuracy obtained from airborne LiDAR due to navigation uncertainties, the precision of sequential returns is significantly higher and can be used to automatically distinguish between different surface preparations. Also, because roughness parameters are based on relative height variations, rather than absolute height values, it is possible to compute RMS_h for transects generated from sequential points along a single scan line. Thus this method produces directional roughness maps in an orientation nearly perpendicular to the flight line. To test this method, the swath collected with a scan angle of $\pm 5^\circ$, scan frequency of 65 Hz, and narrow divergence was employed. With these parameters and at the flying height of 600 meters, the points in the line are

separated by 19.5 cm with a beam footprint of 15 cm. This is almost a continuous sampling of elevations along the scan line. Flying at a ground speed of 60 m/s, the points at nadir between two successive scan lines are separated by 50 cm.

This method was implemented fusing the ASCII multi column text format, which provides a time tag, easting, northing, height, intensity, range, and scan angle for each return point. The timing and/or scan angle information can be used to separate the individual scan lines. Then, for each point in the line, the neighboring points that are within a given distance on either side are identified. Profiles 3 m in length were considered, following the recommendation in [15]. From these points, a profile is built by determining the horizontal distance between the points and the height of each point. The resulting profile is then detrended and its RMS_h is computed. Next the RMS_h is attached to each point as the roughness attribute. The roughness maps can then be created in the same way elevation maps are rendered from the raw point clouds, but using the RMS_h attribute instead of the height. Figure 5-3C shows the created RMS_h map from the entire swath. Figure 5-4A shows the RMS_h map derived with this method from the section of bare soil delineated with a yellow dashed rectangle, as shown in Figure. 5-3B. The RMS_h map shown in Figure 5-4A is rendered using a color scale between 0 and 3 cm, which demonstrates that it is possible to derive fine scale roughness maps from airborne LiDAR data. It also demonstrates the heterogeneity of surface roughness of this 160 m x 40 m area.

Footprint Scale Roughness from Return Waveform Analysis

The return from each laser shot is treated as the reflection from a point source, even though the beam footprint on the ground has some extent. The LiDAR footprint size depends on the flying height above the ground and the beam divergence. For a

flying height of 600 m above ground level, the beam footprint diameter is 15 cm for the narrow divergence mode and 48 cm for the wide divergence mode. Also, LiDAR systems emit laser pulses that have an extent in the time domain. The pulse amplitude-time profile or waveform is usually Gaussian in shape, characterized by a pulse width (FWHM) or by its time variance or standard deviation. This outgoing pulse waveform is modified as the signal is reflected off the target. If the target has a smooth surface oriented normal to the laser beam, the return waveform will be a perfect mirror image of the outgoing waveform. For imperfect reflectors, the return waveform will be distorted through a convolution process, making it possible to deduce geometric properties of the surface illuminated by analyzing the return waveform. One such geometric property is the surface roughness. The advantage of this method is that roughness can be determined for each individual laser shot and, in principle, is immune to the positioning and navigation errors that degrade LiDAR accuracy. The methodology developed in [47] to map surface roughness on Mars from satellite laser altimetry was adapted to map surface roughness using airborne LiDAR.

This approach is based on the principle that the pulse width of a reflection from a rough surface will be longer than the original emitted pulse width, as described by:

$$\sigma_r^2 = \sigma_t^2 + \sigma_l^2 + \sigma_{ir}^2, \quad (5-1)$$

where σ_r^2 is the variance of the received waveform, σ_t^2 is the terrain height variation for the footprint, σ_l^2 is the emitted laser pulse variance and σ_{ir}^2 is the variance due to the detector impulse response. Using the speed of light in the proper medium these time variances can be converted into spatial variances; and by taking into account the beam

divergence, surface slope, and incidence angle, the surface variance or $RMS h^2$ for the footprint is given by:

$$\sigma_s^2 = RMS h^2 = \sigma_i^2 - \frac{4R^2}{c^2} [\tan^2(\gamma) \tan^2(\theta)], \quad (5-2)$$

where R is the one-way laser range, c is the speed of light in the proper medium, γ is the beam divergence, and θ is the incidence angle with respect to the surface local normal.

To implement this method, both discrete and digitized waveform data were used. The data collected with a scan angle of $\pm 5^\circ$, scan frequency of 65 Hz, and wide divergence. With these parameters and at a flying height of 600 m, the points in the line scan line are separated by 19.5 cm. Flying at a ground speed of 60 m/s, the points at nadir between two successive scan lines are separated by 50 cm. Operating the system in wide divergence mode from 600 m AGL yields a beam footprint of 48 cm. The combination of along-track and across-track resolution, plus the footprint size, allows for an overlapping and complete illumination of the surface.

The digitizer data provides 8-bit amplitudes of the outgoing and return waveforms sampled at 1 nanosecond intervals. To obtain the values of σ_r^2 and σ_i^2 an iterative least squares Gaussian fit is applied following the model:

$$wf_{\text{mod}}(t) = A \times \exp\left(-\frac{(t-T)^2}{2\sigma^2}\right), \quad (5-3)$$

where $wf_{\text{mod}}(t)$ is the modeled Gaussian waveform as a function of time (t), with parameters amplitude (A), time for the maximum amplitude (T), and pulse time variance (σ_0^2). The linearized iterative least square model is:

$$\begin{bmatrix} e^{-\frac{(t_1-T_0)^2}{2\sigma_0^2}} & \frac{A_0(t_1-T_0)}{\sigma_0^2} e^{-\frac{(t_1-T_0)^2}{2\sigma_0^2}} & \frac{A_0(t_1-T_0)^2}{\sigma_0^3} e^{-\frac{(t_1-T_0)^2}{2\sigma_0^2}} \\ \vdots & \vdots & \vdots \\ e^{-\frac{(t_n-T_0)^2}{2\sigma_0^2}} & \frac{A_0(t_n-T_0)}{\sigma_0^2} e^{-\frac{(t_n-T_0)^2}{2\sigma_0^2}} & \frac{A_0(t_n-T_0)^2}{\sigma_0^3} e^{-\frac{(t_n-T_0)^2}{2\sigma_0^2}} \end{bmatrix} \times \begin{bmatrix} \frac{\partial A}{\partial T} \\ \frac{\partial \sigma}{\partial T} \end{bmatrix} = \begin{bmatrix} wf_1 - A_0 e^{-\frac{(t_1-T_0)^2}{2\sigma_0^2}} + v_1 \\ \vdots \\ wf_n - A_0 e^{-\frac{(t_n-T_0)^2}{2\sigma_0^2}} + v_n \end{bmatrix}, \quad (5-4)$$

where n is the number of waveform samples obtained, t_n is the time for sample n , wf_n is the digitized amplitude value of sample n . A_0 , T_0 , σ_0 are the approximation of the Gaussian parameters for the current iteration, and ∂A , ∂T , σ_0 are the correction factors for the parameter approximations to be determined for every iteration.

For each laser shot fired, the time variance of the outgoing and return pulse waveforms were determined. This yields two of the variable values used in Equation 5-1. To estimate the time variance due to the system's impulse response a smooth flat area was selected for which it is assumed that $\sigma_i^2 = 0$. From 5032 observations it was determined that σ_{ir}^2 is 2.72 nanoseconds². With this, the σ_i^2 for each emitted pulse was computed. Then Equation 5-2 is applied, and the footprint scale RMSh can be obtained. The RMSh is then attached to each element of the LiDAR point cloud as an additional attribute. The roughness map can then be generated using a point cloud rendering software in the same fashion as the last method. Figure 5-3D shows the RMSh map rendered from the entire swath and Figure 5-4B for the bare soil surface. By comparing Figures 5-3C and 5-3D it can be seen that this method provides finer spatial detail, but, it is also very sensitive to digitizer noise that can affect the correct determination of the fit parameters.

Point Cloud Binning

A final method to create RMSH maps from high density point clouds consists of creating an array or grid of square surface elements (cells or bins) of a given area. Each bin has well-defined boundaries. Then the individual points are assigned to a given bin based on its horizontal coordinates. Once all the points are segregated into their respective bins, the point's coordinates are used to determine the 3D trend. After separating the random height component, the RMSH is computed and this value is assigned to the respective bin. Repeating the process for all the bins, a raster map is generated. To test this method, the swath collected with a scan angle of $\pm 5^\circ$, scan frequency of 65 Hz, and narrow divergence was employed. With these parameters, a flying height of 600 m and a ground speed of 60 m/s, the nominal point density is 10.26 points/m². Figure 5-3E shows an RMSH map derived from this data using a bin size of 1x1 m. Figure 5-4C shows the RMSH map for the bare soil surface.

Validation of Airborne Roughness Maps

To validate the RMSH maps obtained from the airborne data, a ground-based LiDAR was employed to digitize two samples of a bare soil surface. These surface samples are delineated by black squares in Figure 5-4A. Figure 5-5 shows photos of the validation areas and DEMs derived from the ground-based LiDAR. To validate the RMSH obtained from airborne data using the profiling method, transects were extracted from the ground-based DEM in the north-to-south direction LiDAR. These transects were then detrended and the RMSH computed for each one. Figure 5-6 shows a histogram of RMSH values obtained from the profiling method from airborne and ground-based data. Values derived from airborne data have a larger spread, but, their

means differed by only 1mm. The mean RMS_h derived from ground-based measurements is 2.2 cm and from airborne is 2.1 cm.

RMS_h results obtained by applying the binning method to ground-based and airborne data are also shown in Figure 5-6. Similar to the results from the profiling method, the airborne derived RMS_h values have a larger spread but their means also only differ by 1 mm. The mean RMS_h from ground-based data was determined to be 1.8cm and from airborne data it was found to be 1.7 cm. To validate the RMS_h results obtained through the return waveform analysis method, the ground-based data was analyzed using the binning method considering a bin size of 0.43 meters, which comprises an area equivalent to the footprint area with a diameter of 48 cm. The average RMS_h obtained from the ground-based data following this approach was 1.4 cm. However, it was not possible to obtain a coherent set of RMS_h values from the waveform analysis for the validation areas. In fact, to obtain RMS_h values below 3 cm using this method requires the determination of the time variances with an accuracy better than 0.1 nanoseconds. In the current implementation of the waveform digitizer, this level of accuracy cannot be reached. However, technology will continue to improve and in the near future the capability to determine fine-scale RMS_h from waveform data will be reached. It is also worth noting that this method is applicable to characterizing vegetation structure, especially low grasses and shrubs that are not fully characterized using discrete LiDAR data.

A cross validation between RMS_h results obtained from the profiling and binning methods from airborne data was performed. To have a consistent comparison, RMS_h obtained from the profiling method considering transects 3 m in length was compared to

the values obtained for bins 3 m x 3 m in area. A histogram of the obtained RMS_h from both methods is presented in Figure 5-6. The average RMS_h of the entire bare soil surface obtained with the profiling methods is 2.1 cm, while the average value obtained by applying the binning method is 2.7 cm. This result is consistent with the results obtained in Chapter 4, where RMS_h values obtained from 2D profiles is lower by 25% on average than the values derived from 3D data.

Finally, it is worth mentioning that the airborne data was collected in a way that ensures consistency between the three proposed methods and to record the waveform of every fired pulse. The digitizer limited the sampling capabilities of the ALTM by half. Operating the ALTM at its maximum PRF (166 kHz), would have yielded sampling densities more than twice the density of those collected, improving the results obtained with the profiling from a single scan line and the point cloud binning methods. The technology that was employed to collect this airborne dataset is a generation old. The current generation of ALTM includes a system that integrates three scanning mechanisms into a single unit, and it is capable of PRFs of 400 kHz. Faster digitizers are also available as electronic modules that have a sampling speed of 2 GHz, or twice the current digitizing capabilities, thus improving the sensitivity of footprint scale roughness by a factor of 2.

Chapter Conclusions

Data from ground-based LiDAR is useful to characterize mm-level surface roughness of areas that can encompass a few hundred square meters. For the characterization of roughness of larger areas, high resolution airborne LiDAR is a viable option. It was demonstrated that there are several ways to derive accurate mm level roughness maps for surfaces with RMS_h higher than 1 cm. These include directional

roughness derived from transects extracted from a single scan line and full surface roughness derived from data collected over a given area. Unfortunately current technology, does not allow for the determination of LiDAR footprint-scale roughness below the 10 cm RMS_h level.

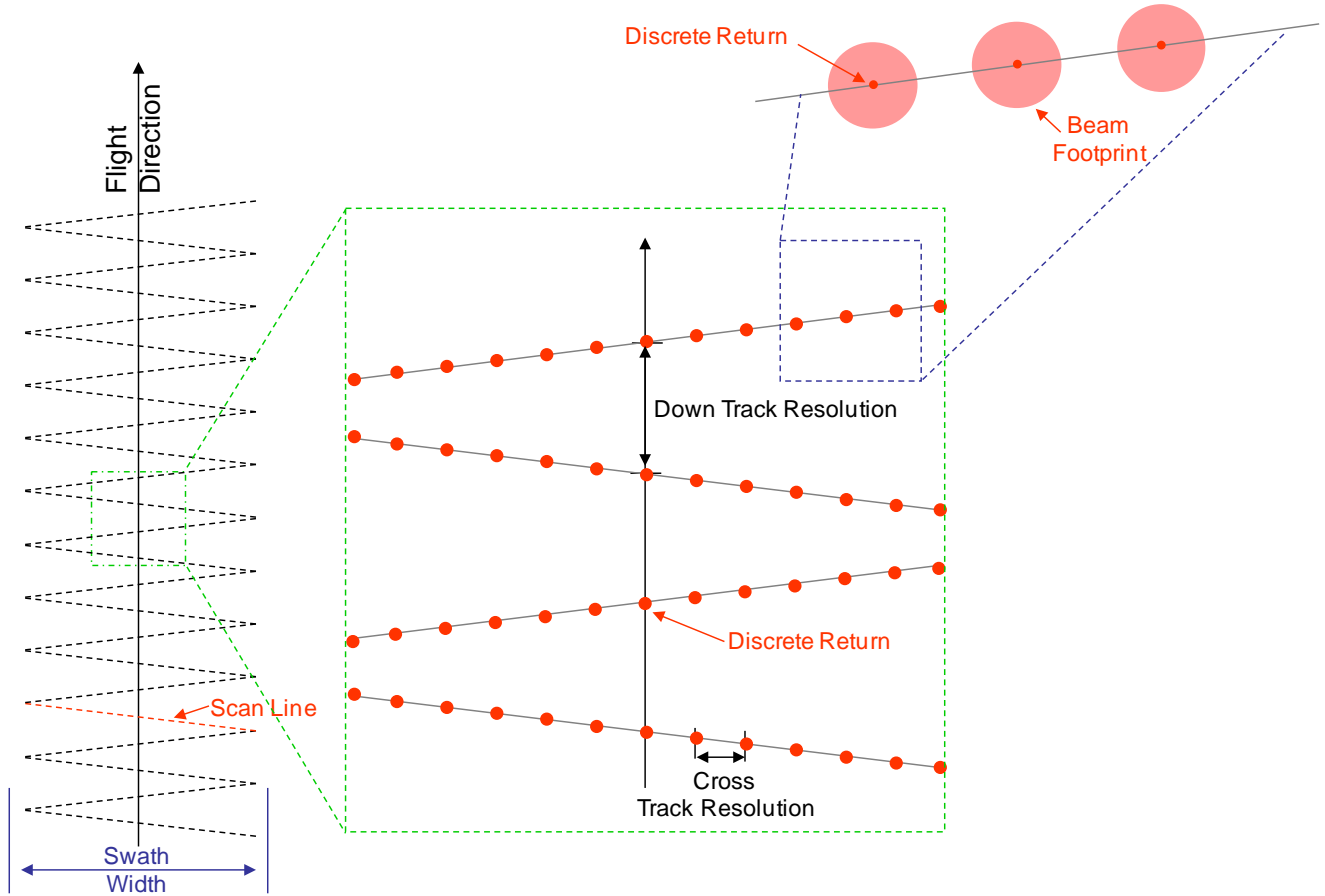


Figure 5-1. Geometry of airborne scanning LiDAR data collection.

A



B



Figure 5-2. The National Center for Airborne Laser Mapping (NCALM) Gemini ALTM and waveform digitizer.

A) Front side of the control and electronics rack and digitizer computer. B) Rear side of the racks and later side of the sensor head.

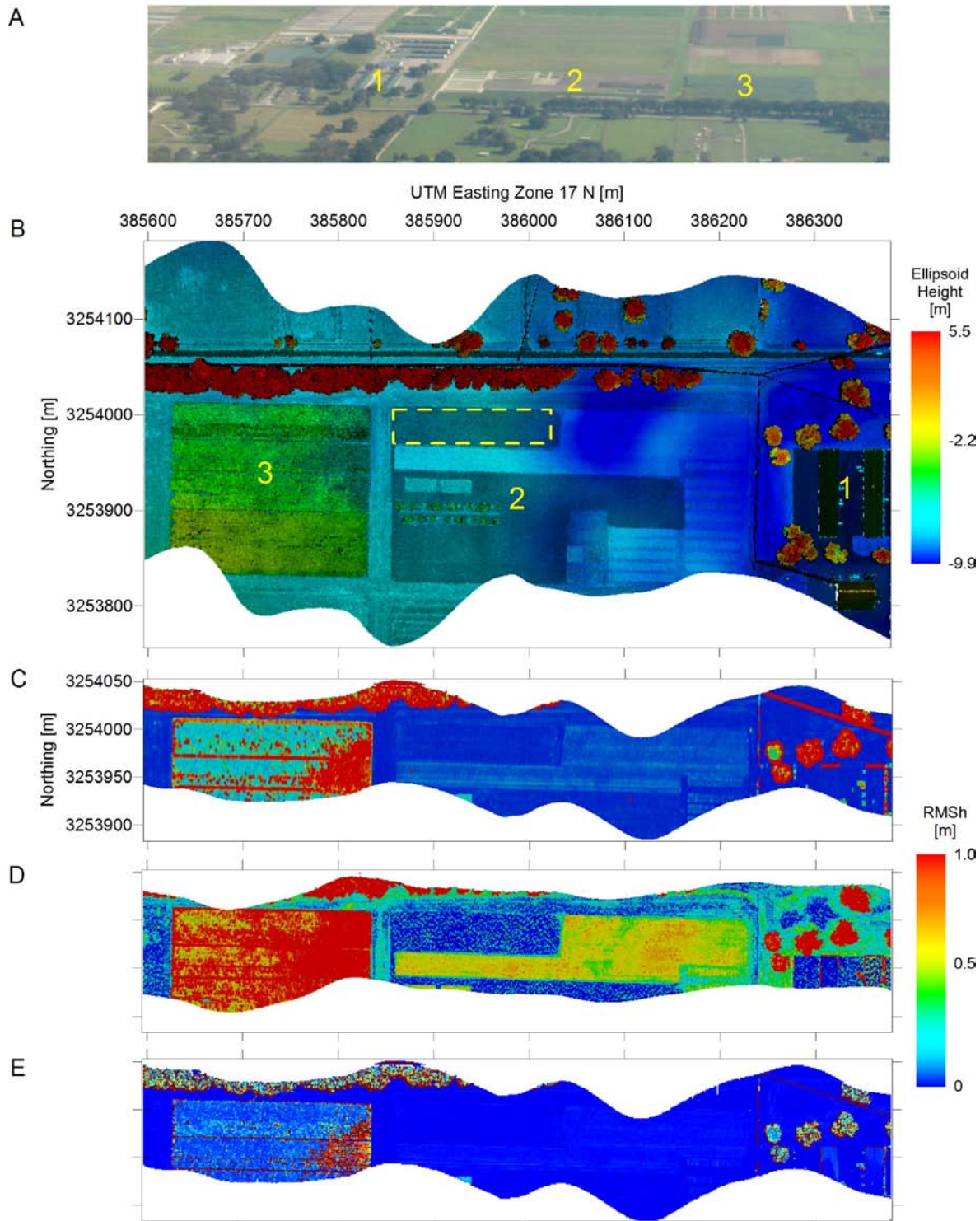


Figure 5-3. Airborne LiDAR roughness maps. A) Photo of the general area of PSREU that was surveyed with the airborne LiDAR, the orientation of the photo is east to the right, west to the left. B) Point cloud rendering from a swath $\pm 14^\circ$ from 600m AGL. C) RMSH map using the profile along a single scan line method. D) Footprint scale RMSH map from analysis of the return waveforms. E) RMSH map from airborne LiDAR using point cloud binning method.

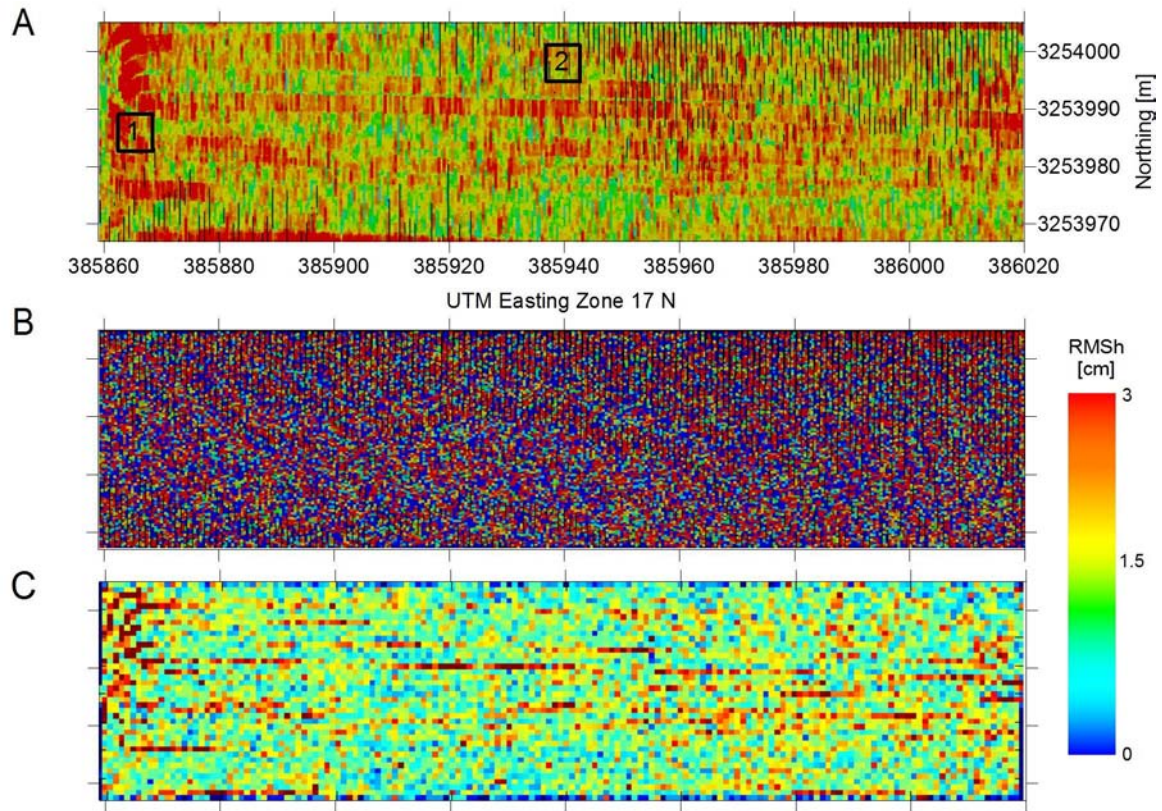


Figure 5-4. Surface roughness map of a bare soil area marked as a yellow dashed rectangle in Figure 5-3. A) From profiles from single scan line method. B) Footprint scale roughness RMSh from return waveform analysis. C) From the point cloud binning method.

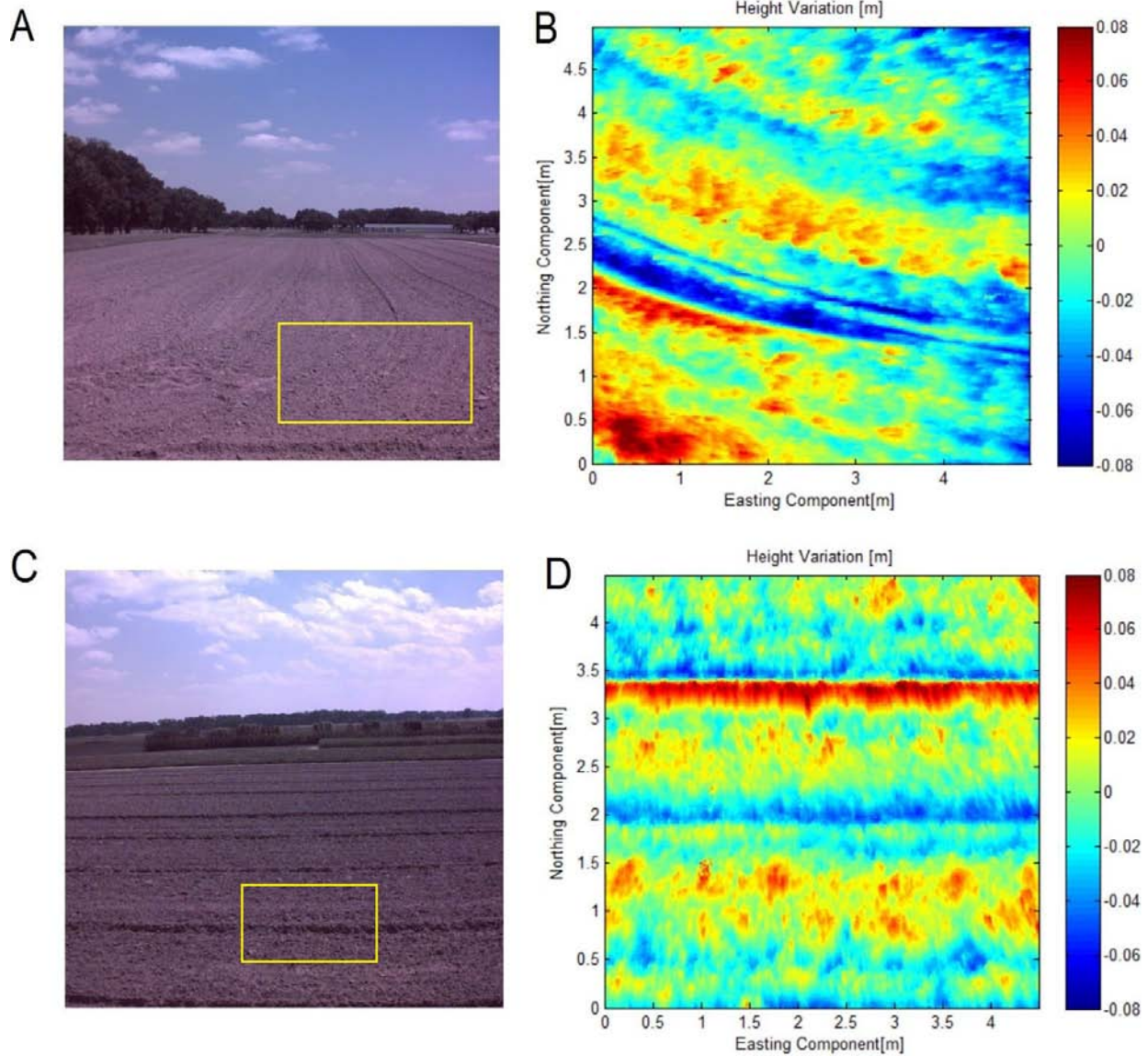


Figure 5-5. Validation areas for the airborne derived roughness maps marked as squares 1 and 2 in Figure 5-3 A.

The yellow rectangles represent the areas from which the DEMs were created. A) Photo of validation area 1, looking east. B) Ground-based LiDAR derived DEM of validation area 1. C) Photo of validation area 2, looking south. D) Ground-based LiDAR derived DEM of validation area 2.

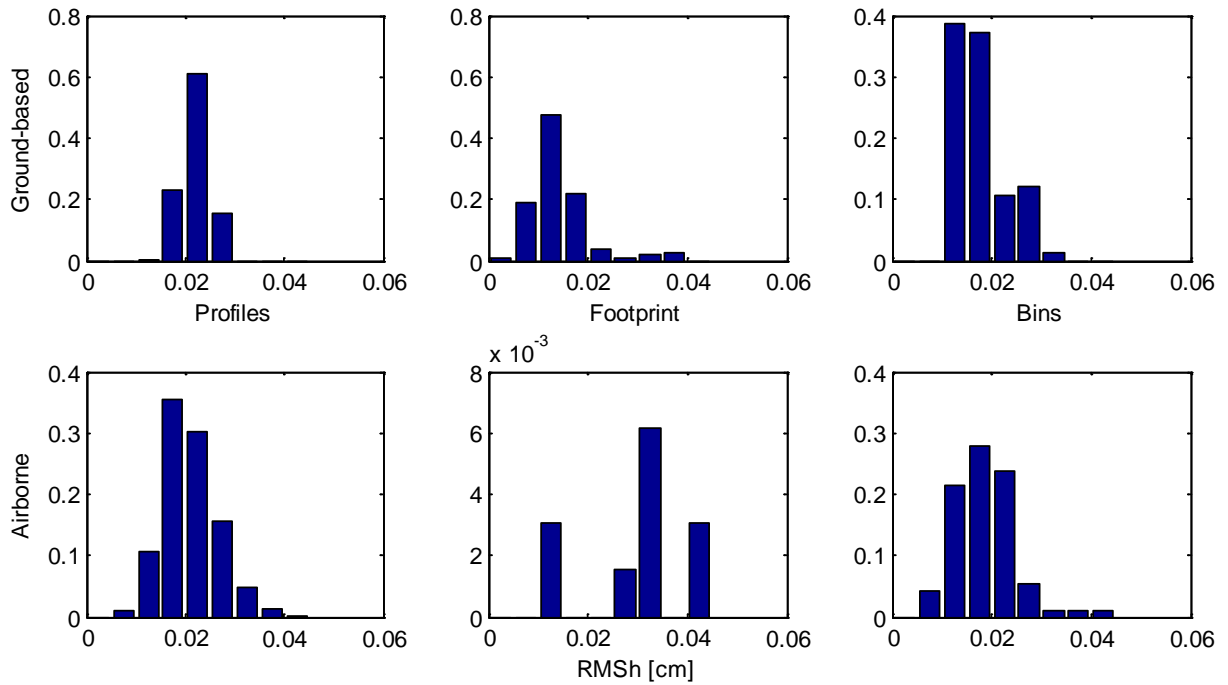


Figure 5-6. Validation of the airborne derived RMSh from the three proposed methods compared to RMSh values derived from ground-based LiDAR data through similar processing.

Table 5-1. Optech GEMINI Airborne Laser Terrain Mapper (ALTM) specifications

| Parameter | Specified Value |
|---------------------------------------|--|
| Operating altitude | 150 - 4000 m, nominal |
| Horizontal accuracy | 1/5,500 x altitude (m AGL); 1 sigma |
| Elevation accuracy | 5 - 30 cm; 1 sigma |
| Range capture | Up to 4 range measurements, including 1 st , 2 nd , 3 rd , last returns |
| Intensity capture | 12-bit dynamic range for all recorded returns, including last returns |
| Scan FOV | 0 - 50 degrees; Programmable in increments of ± 1 degree |
| Scan frequency | 0 – 70 Hz |
| Scanner product | Up to Scan angle x Scan frequency = 1000 |
| Roll compensation | ± 5 degrees at full FOV – more under reduced FOV |
| Pulse rate frequency | 33 - 167 kHz |
| Position orientation system | Applanix POS/AV 510 OEM includes embedded BD950 12-channel 10Hz GPS receiver |
| Laser wavelength/class | 1047 nanometers / Class IV (FDA 21 CFR) |
| Beam divergence nominal (full angle) | Dual Divergence 0.25 mrad (1/e) or 0.80 mrad (1/e) |

Table 5-2. Optech waveform digitizer specifications

| Parameter | Specified Value |
|--|----------------------|
| Amplitude resolution | 8 bits (0 -255) |
| Sample interval | 1 nanosecond |
| Maximum acquisition and recording rate | 70 kHz |
| T0 record length | 40 samples / 40 ns |
| Return waveform record length | 440 samples / 440 ns |
| Full scale input range | 0-1 V |

Table 5-3. Airborne LiDAR datasets

| Strip | m AGL | Scan angle | Scan frequency | Divergence | Points |
|---------------------|-------|----------------|----------------|------------|-----------|
| S1C1_Field_245b_008 | 600 | $\pm 14^\circ$ | 60 Hz | Narrow | 2,411,841 |
| S1C1_Field_245b_009 | 600 | $\pm 5^\circ$ | 65 Hz | Narrow | 2,319,168 |
| S1C1_Field_245b_011 | 600 | $\pm 5^\circ$ | 65 Hz | Wide | 2,099,178 |

CHAPTER 6 CONCLUSIONS AND RECOMMENDATIONS

Conclusions

The work presented in this dissertation was performed as a multi-step approach to address the current limitations and challenges of the characterization of surface roughness for its application to microwave emission and scattering models applied to the problem of soil moisture mapping. The first step in the process was to characterize instrument errors and perform an accuracy assessment of the roughness parameters derived from measurements obtained from these instruments (meshboard and ground-based LiDAR). Once the accuracy of these instruments and the comparative baseline between the roughness parameters obtained from their measurements was established, ground-based LiDAR was used to collect an extensive database of 3D bare soil surface measurements. This database was used to test the validity of current assumptions that surface roughness is a single-scale random process that could be characterized from its standard deviation, correlation length, and the shape of its autocorrelation function. The 3D information was also used to determine the impact on roughness parameter values obtained from 2D profiles with respect to the values obtained from full surface digitization. As a final step, the issue of assuming homogeneity of roughness characteristics used when scaling a limited number of *in situ* roughness measurements from a large area was addressed with airborne LiDAR.

As referred to in several chapters of this dissertation, there has been much discussion of the characterization of surface roughness as a single-scale process when results of many studies indicate multi-scale characteristics. The data collected and analyzed for this work indicate that, in fact, natural and agricultural surfaces have height

variations at different scales. However, if 3D information with sufficient resolution and extent is collected it is possible to separate the height variations at any particular scale. The question that remains is at what scale or scales does roughness have to be characterized to be an accurate input to the current single-scale microwave emission or scattering models? An alternative is to use multiple-contribution models that consider the effects of roughness in two or more scales.

It was also determined from results of the experiments that roughness characteristics of agricultural soils are not isotropic and homogenous, as has been assumed for microwave modeling. In addition, it was observed that the autocorrelation functions of agricultural soils are not fully explained by the theoretical exponential or Gaussian ACFs. Microwave emission and scattering models need to be improved to account for generalized power law spectrum ACF and for the anisotropy and heterogeneity of agricultural and natural surfaces.

Roughness parameter values are very sensitive to instrument errors, especially the autocorrelation function and its correlation function. To accurately determine the parameter values it is necessary to remove all systematic errors from the height variation measurements. It is also necessary to properly characterize the instrument random errors. The raw height variation measurements obtained with any instrument is the result of the addition of two random processes: the surface roughness and the instrument random noise. Accurate estimation of the surface roughness parameters depends on compensating for the effects of the instrument noise.

Due to the anisotropic and heterogeneous characteristics of natural and agricultural surfaces, sampling a surface in transects is not adequate. Parameters

obtained from 2D data considerably underestimate the surface roughness and do not describe its directional properties. 3D information derived from ground-based and airborne LiDAR is adequate for the proper characterization of surface roughness.

Recommendations

The work presented in this dissertation was described as a multi-step approach to address the current limitations and challenges of the characterization of surface roughness. At this point there are several additional steps that might be taken in future work to continue building on the foundation presented here. Future work might include the extension of the accuracy assessments performed to 3D. Also, analytical models to quantify and correct the effect of random instrument errors in the derived roughness parameters could be developed. An additional lateral direction with high relevance that needs to be explored further has to do with determining what the adequate scale or scales are from which roughness parameters need to be determined. In other words, what is the appropriate detrending method that needs to be applied in order to obtain the best agreement between the observed and modeled microwave signatures? In the dataset used in this study there are several roughness measurements that were performed concurrently with microwave observations and soil moisture measurements during the different MicroWEX experiments. Combining the roughness measurements with the MicroWEX experiments for this purpose would represent an additional advancement in the current state of knowledge.

A forward direction that also needs to be explored involves expanding the experiments employing airborne LiDAR to characterize surface roughness of large areas, considering a variety of surface preparation conditions (rolled, plowed, furrowed) and combining airborne-derived roughness maps with microwave spaceborne

observations and *in situ* soil moisture measurements. An alternate, related approach is the assessment of ICESAT-1 data to derive surface roughness maps at a footprint scale.

Main Contributions

Major achievements that contribute to the advance of knowledge presented in this work include:

- Performing the first assessment of the digitizing fidelity and accuracy of derived roughness parameters for the meshboard and ground-based scanning LiDAR.
- Creation of a large database of 2D profiles (total length 100 km) that was used to: determine the roughness parameter value ranges at different scales; test the hypothesis of the existence of a correlation between the RMS_h and correlation length; and test the applicability of Gaussian and exponential ACF to explain the observed ACF from natural and agricultural surfaces.
- Development of a methodology to derive the traditional surface roughness metrics from 3D DEMs obtained from ground-based LiDAR. Compare roughness parameter values obtained from single profiles to those obtained from the full surface using first and second order detrending.
- Quantified the underestimation of surface roughness parameters when determined from a limited number of surface profiles.
- Developed alternate methodologies to characterize 3D random roughness from DEMs of surface that exhibit quasi-periodic or non-stationary trends, such as those arising from row or furrow structures resulting from agricultural preparations.
- Development of three alternate methods to produce fine-scale roughness maps of large areas employing airborne LiDAR. Demonstrating that it is possible to obtain mm accuracy for surfaces with RMS_h higher than 1 cm and validating it against high resolution data obtained from ground-based LiDAR.
- Development of a method to model and remove systematic errors (geometric distortion and parallax) present in meshboard data, thus being able to obtain fidelity and accuracy in the study profiles and their derived roughness metrics higher than ever reported before in literature.

APPENDIX A MICROWAVE SCATTERING AND EMISSION MODELS APPLIED TO SOIL MOISTURE MAPPING

The water cycle describes how this compound in its different phases (solid, liquid and vapor) moves through the atmosphere, the land, and bodies of water. Water plays an important role in the carbon and energy cycles. It enables the growth of vegetation, which in turn, through the evaporation and transpiration processes, moves vapor and energy from the land to the atmosphere, modifying the weather and climate [48]. Of the water in the planet, roughly 97.5% is salt or mineralized water. Of the remaining 2.52% uncombined fresh water 0.006% is present in rivers and streams, 0.26% in fresh water lakes, and 0.001 % in the atmosphere The rest of the fresh-water component occurs as soil moisture, permanent snow cover, marshes, and active groundwater [49]. Even when the total amount of water on the planet is considered fixed, on a global scale, there are gaps in knowledge about how and at what pace these reserves are being transformed [48].

Soil moisture, which is defined as the water held between soil particles, albeit representing only 0.001% of the total water and 0.05% of the fresh water [50] is a critical factor to many hydrology, biology, biochemistry and ecology processes. It is crucial in regulating the water and energy exchanges between the land and lower atmosphere, and it is the dominant factor in vegetation growth and crop yield. Soil moisture also affects strongly the runoff into streams and rivers. Despite its importance, current datasets are limited to few *in situ* measurements. Global datasets are urgently required to improve our understanding of the global water cycle and to improve the current weather and climate models [48] and [51]. In order to obtain large scale datasets remote sensing techniques must be applied. Different remote sensing technologies have been

researched over the years to map soil moisture, including the analysis of reflectance on visible, near and shortwave infrared; thermal infrared emittance; brightness temperature and scattering coefficient in the microwave bands. To date the most promising results are achieved through the use of active and passive microwave sensors [6]. Microwave remote sensing of soil moisture is based on the principle that there is a large difference in the values of the dielectric constant of dry soil (~3.5) and water (~80) [6]. Soil scattering and emission properties in the microwave region are directly related to the surface roughness and dielectric constant; they are also dependent on sensor characteristics (wavelength and polarization) and observation geometry (incidence angle) [2].

Currently several models exist, ranging from the empirical to purely physical-analytical, that can be used to retrieve soil moisture from the backscatter coefficient obtained from active radar sensors or emissivity obtained from passive radiometers [7]. The physical-analytical models provide estimates of the microwave scattering or emission as a function of the surface's roughness and dielectric constant. In addition, many models provide estimates of the soil dielectric constant based on its composition and water content. If the roughness of a surface and its scattering or emitting properties are determined then it is possible to invert the microwave models to obtain estimates of the dielectric constant, and applying the soil dielectric mixing models is possible to derive estimates of soil moisture.

Among the main analytical models, some worth mentioning are: The Small Perturbation Model (SPM) published by S.O. Rice in 1951 [52]. The Kirchoff Approximation (KA) developed by P. Beckman and A. Spizzichino, which was published

in 1963 [53]. More recently there is the Small Slope Approximation (SSA) published in 1985 by A.G. Voronovich [54]. The Integral Equation Model (IEM) developed by Fung, Li and Chen from the Wave Scattering Research Center, University of Texas at Arlington in 1991 to describe the backscattering from a randomly rough dielectric surface [40]. Finally, the Advanced Integral Equation Model (A-IEM), which is a refined version of the IEM suitable to model emission of a rough surface, was developed by Chen, Wu, Tsang, Li, Shi and Fung in 2002 [41].

These models are based on the assumptions of single scale isotropic surface roughness. They have their intrinsic limitations and regions of holding. For instance the SPM is valid for slightly rough surfaces, the KA is applicable for a rough surface with a large surface curvature, SSA and IEM bridge the gap between the SPM and KA. Results from IEM are in good agreement with the ones obtained from SPM and KA in their respective region of holding [7] and [41]. According to Thoma et al., IEM is currently the most widely used scattering model for bare soil studies [26] with a validity range of $ks < 3$, where k is the wave number ($k=2\pi/\lambda$) and s is the surface RMSh [41]. IEM has been successfully validated in laboratory settings but has yielded contradictory results from real field experiments. Explanations for the discrepancy have been offered in the literature by accounting for several factors: the high heterogeneity of roughness and moisture conditions present in agricultural fields, physical approximations considered in the model which had not been checked *a posteriori*, and finally, that the current mathematical description of the surface roughness is not sufficient to capture its real complexity [7].

Several researchers have recognized the limitation in the description of surface roughness and have proposed alternate models to better explain the microwave backscattering. Zribi et al. has proposed a model for the backscattering on soil structure described by plane facets [12]. Mattia and Toan proposed an enhancement to IEM that described surface roughness as a multiscale fractal random process [55].

All the above models only consider the effect of random roughness. The effects of artificial machined agricultural structures (oriented roughness), such as rows and furrows on microwave backscattering are considered by other analytical models. Ulaby et al. in [42] considers the case of a random roughness component superimposed over a stationary periodic surface along one dimension as a description of row structure typical of many agricultural fields and mathematically characterized by:

$$z(x, y) = z(y + n\Lambda) = A \left[1 + \text{Cos} \left(\frac{2\pi y}{\Lambda} \right) \right], \quad (\text{A1-1})$$

where A is the amplitude of the periodic oscillations and Λ is its spatial period [42].

Kong et al. provides a solution for the emission of one such surface by applying modal theory [56], while Johnson et al. provides solutions for the scattering and emission of periodic surfaces in one and two dimensions [57].

These physical-analytical models provide estimates of the microwave emission and scattering based on the dielectric constant of the soil, the surface roughness, and the sensor parameters (polarization, wavelength, and incidence angle). To obtain the dielectric constant based on the soil composition and its water content several mixing models exist. To learn more of these mixing models refer to [58] - [61].

APPENDIX B IMPROVEMENT TO THE MESHBOARD PROFILE DIGITIZATION METHOD

The meshboard used to record surface profiles is a 2.14 m long by 0.9 m high and 0.003 m thick aluminum plate marked with a 2 cm x 2 cm grid as shown in Figure A2-1. To obtain a profile the meshboard is placed over the study surface, then a digital photo is taken as perpendicular to the meshboard as possible. The photograph is then loaded into image-processing software where the profile is manually digitized by an operator or by an automatic edge detection algorithm. The digitized profile then needs to be converted from pixel coordinates to meshboard or real space coordinates by a transformation model.

For the first meshboard data collections, the meshboard photo was loaded into the image processing software SigmaScan Pro5, where the user selected control points on the meshboard grid and then digitized the soil profile. One of the digitizing methods employed consisted in picking a height measurement at every point where the slope of the surface is changing or at least every 1 cm. For one 2.14 m long mesh board, each digitized picture yields 214 data points if there is no missed sampling point. The digitize profile was output into a MS Excel csv file with two columns for the x and y coordinate pairs. A more detailed description of the meshboard photo digitizing process using SigmaScan Pro can be found in [36] (Mi-Young et al., 2005).

The use of the proprietary software SigmaScan Pro was abandoned because early comparisons between profiles digitized using LiDAR and Meshboard showed systematic errors in the meshboard data causing the edges of the profiles to curve up or down. Figure A2-2 illustrates these distortions resulting from digitizing a flat smooth surface. To try to understand and correct these errors and to have full control over the entire

process Matlab scripts were developed to digitize and process the meshboard data which are described in the next paragraphs.

When deriving measurements from a photograph, it is important to take into account that the image is subjected to spatial deformation due to imaging geometry and effects introduced by the lens. The traditional photogrammetry approach used to obtain accurate measurements from photos consist of first characterizing the lens by determining its systematic distortion parameters, removing those effects present in the image and then determining the scale factors necessary to convert the pixel coordinates to real space coordinates through different transformation models [62].

This approach is not applicable when using inexpensive digital cameras with an autofocus option because the distortion parameters vary for each photo taken. A novel two step approach was followed to minimize the effects of distortion and parallax. First, 5 control points for which coordinates in both image and meshboard coordinates were known were used to determine the parameters of an affine transformation. This transformation is applied to both the study profile and 107 points along one of the marked horizontal lines of the meshboard just on top of the soil profile. The transformed profile and horizontal line contain the effects of geometric distortion but because derived and true real space coordinates are available for the horizontal line points it is possible to calculate coordinate differences between these coordinates as function of the position over the meshboard. This allows the researcher to characterize and remove the distortion present in the digitized profile.

For this work a Canon PowerShot S2IS 5 megapixel camera was employed to obtain the meshboard digital images. To minimize the effect of lens distortion and

parallax, the photos were taken such that meshboard and the camera's focal plane were parallel, the meshboard covered between 80 and 90% of the frame, and the study profile was as close as possible to the horizontal axis of the lens. To process the photograph, the Matlab script loads it to memory and in the first step displays the entire picture on the screen. At that zoom level, it is hard to digitize control points and the profiles in an accurate fashion. So the user then uses the pointer to position and select 12 points that correspond to upper left and lower right corners of 6 areas to be zoomed into as marked on Figure A2-1. The first five of these six areas contain 5 control points marked on the meshboard. The last area contains the profile to be digitized. After the twelve points have been selected, five windows will automatically be displayed, one at a time, for which the user has to position and click over the displayed control point as accurately as possible.

From these control points both image and meshboard coordinates are known, so it is possible to determine a single scale factor or the parameters of an affine transformation. The single scale factor has been used by some researchers to obtain a digitized profile in meshboard coordinates and it can be determined as:

$$ssf = \frac{mb \text{ length [meters]}}{mb \text{ length [pixels]}} = \frac{2.1336 [m]}{\sqrt{(i_{cp2} - i_{cp1})^2 + (j_{cp2} - j_{cp1})^2} [pixels]}, \quad (A2-1)$$

where i_{cp2} and i_{cp1} are the pixel row coordinates of control points 2 and 1, corresponding to the meshboard top right and left corners. j_{cp2} and j_{cp1} are the pixel column coordinates of control points 2 and 1.

The affine transformation model is:

$$\begin{aligned}
X_1 &= A \times i_{cp1} + B \times j_{cp1} + C \\
Y_1 &= D \times i_{cp1} + E \times j_{cp1} + F \\
X_2 &= A \times i_{cp2} + B \times j_{cp2} + C \\
Y_2 &= D \times i_{cp2} + E \times j_{cp2} + F, \\
&\vdots \\
X_5 &= A \times i_{cp5} + B \times j_{cp5} + C \\
Y_5 &= D \times i_{cp5} + E \times j_{cp5} + F
\end{aligned} \tag{A2-2}$$

or in matrix form:

$$\begin{bmatrix} X_{cp1} \\ Y_{cp1} \\ \vdots \\ X_{cpn} \\ Y_{cpn} \end{bmatrix} = \begin{bmatrix} i_{cp1} & j_{cp1} & 1 & 0 & 0 & 0 \\ 0 & 0 & 0 & i_{cp1} & j_{cp1} & 1 \\ & & \vdots & & & \\ i_{cpn} & j_{cpn} & 1 & 0 & 0 & 0 \\ 0 & 0 & 0 & i_{cpn} & j_{cpn} & 1 \end{bmatrix} \times \begin{bmatrix} A \\ B \\ C \\ D \\ E \\ F \end{bmatrix}, \tag{A2-3}$$

where i_{cpn} and j_{cpn} are the pixel row and column coordinates of control point “n” and X_{cpn} and Y_{cpn} are the meshboard metric coordinates of control point “n”. A, B, C, D, E and F are the parameters of the affine transformation of which A, B, D and E are scale factors and C and F are translations [62]. These parameters are determined through a least squares procedure.

After the control points are selected and transformations are computed, six windows are sequentially displayed containing 6 segments of the profile at an appropriate zoom level to be digitized accurately. The user then digitizes the profile on the computer screen using the mouse cursor. The script records the digitized pixel coordinates. After digitizing the study profile, the user has to digitize the 107 intersection points of the vertical lines along one of the marked horizontal lines of the meshboard just on top of the soil profile for is uses in the correction of the remaining distortions. For this purpose a new set of 6 windows are sequentially displayed containing 6 segments

of the meshboard at an appropriate zoom level. After the profile and horizontal line are digitized the Matlab script uses the single scale factor and the 6 parameters of the affine transformation to convert the digitized profiles and horizontal line in pixel coordinates to meshboard coordinates by applying:

$$\begin{aligned} X_{pp_n} &= ssf \times (j_{pp_n} - \min[j_{pp_n}]) \\ Y_{pp_n} &= ssf \times (\max[i_{pp_n}] - i_{pp_n}) \end{aligned} \quad (A2-4)$$

and

$$\begin{aligned} X_{pp_n} &= A \times i_{pp_n} + B \times j_{pp_n} + C \\ Y_{pp_n} &= D \times i_{pp_n} + E \times j_{pp_n} + D \end{aligned} \quad (A2-5)$$

Equation A2-4 is applicable for the single scale transformation model and Equation A2-5 is applied for the affine transformation mode, where ssf is the single scale factor determined according to Equation A2-1, X_{pp_n} and Y_{pp_n} are the metric meshboard coordinates for the “n-th” profile point, and i_{pp_n} and j_{pp_n} are the pixel row and column coordinates of the “n-th” digitized profile point. A, B, C, D, E and F are the scale and transformation parameters.

Figure A3-2 provides an illustration of the distortions suffered by a smooth flat surface ($RMS_h = 0$) when digitized with the meshboard not parallel to the focal plane of the camera for different transformation techniques. Note that besides the curved distortion the meshboard length is distorted from 2.13 to 2.5 m. To remove the distortion effects the coordinates from the 107 interception points of the vertical lines along one of the marked horizontal lines of the meshboard are used. Because derived and true real metric meshboard coordinates are available for these points it is possible to calculate differences between these coordinates as function of the position over the meshboard of the form:

$$\begin{aligned}\Delta x &= X_{lp_n}^{True} - X_{lp_n}^{det} \\ \Delta y &= Y_{lp_n}^{True} - Y_{lp_n}^{det}\end{aligned}\tag{A2-6}$$

where X_{lp}^{True} and Y_{lp}^{True} are the true x and y coordinates meshboard for the line interception points and X_{lp}^{det} and Y_{lp}^{det} are the determined coordinates after the application of the affine transformation. These coordinate differentials are plotted as dots in Figure A2-3. These differentials were then modeled as high order polynomial following the forms:

$$f\Delta x(X_l^{det}) = A_x \times (X_l^{det})^6 + B_x \times (X_l^{det})^5 + C_x \times (X_l^{det})^4 + D_x \times (X_l^{det})^3 + E_x \times (X_l^{det})^2 + F_x \times (X_l^{det}) + G_x \tag{A2-7}$$

$$f\Delta y(X_l^{det}) = A_y \times (X_l^{det})^3 + B_y \times (X_l^{det})^2 + C_y \times (X_l^{det}) + D_y . \tag{A2-8}$$

The coefficients $A_x, B_x, C_x, D_x, E_x, F_x, G_x, A_y, B_y, C_y$ and D_y are determined via least squares. Once the coefficients are known Equations A2-7 and A2-8 are applied to obtain the correction factors for each individual point of the digitized profile, the final corrected profile coordinate points are given by:

$$X_{lp_n}^{corr} = X_{lp_n}^{det} + f\Delta x(X_l^{det}), \tag{A2-9}$$

$$Y_{lp_n}^{corr} = Y_{lp_n}^{det} + f\Delta y(X_l^{det}). \tag{A2-10}$$

Figure A2-2 shows the final corrected profile. Once the profile is corrected the Matlab script writes a text file containing the x and y coordinates for the profile points.

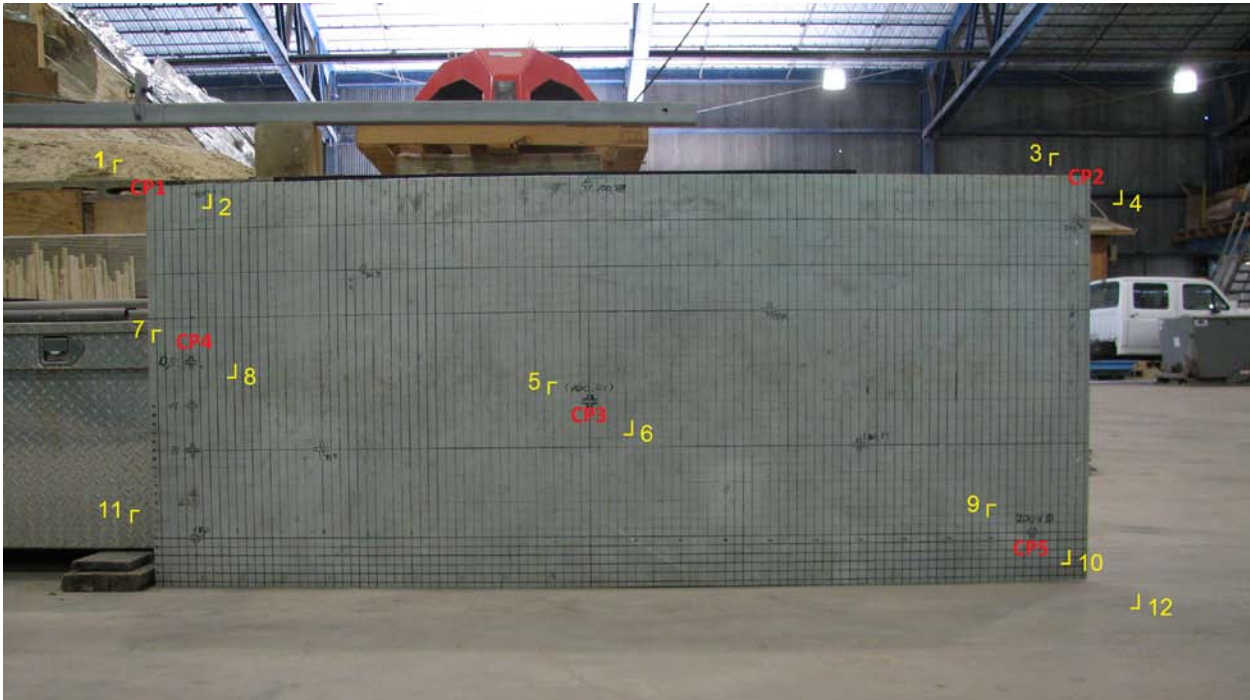


Figure A2-1. Meshboard and the marked control points.

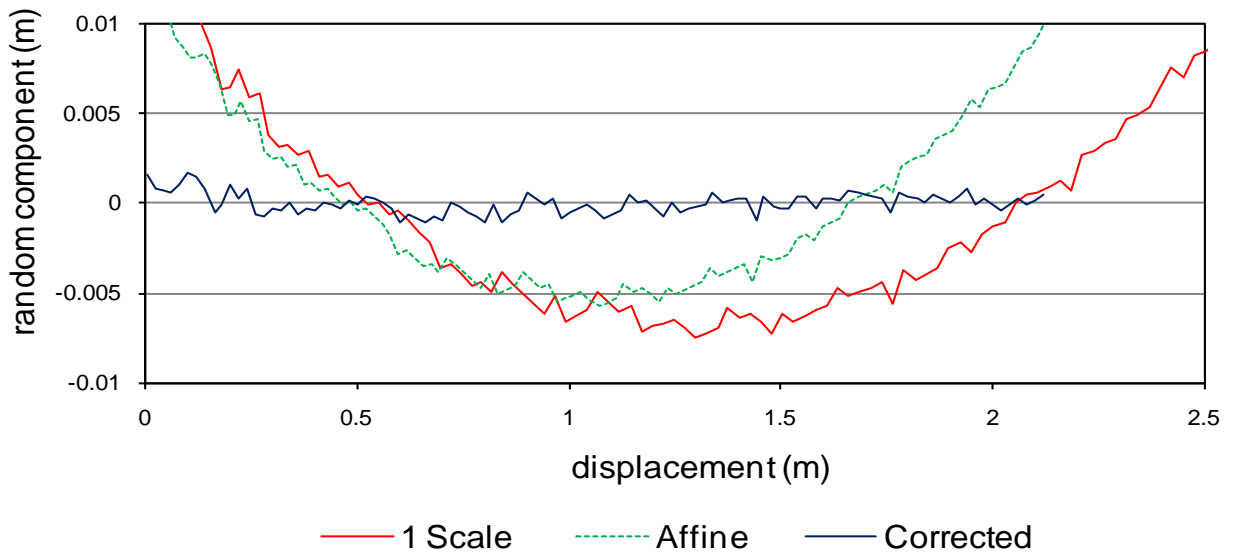


Figure A2-2. Flat smooth profile at different processing steps.

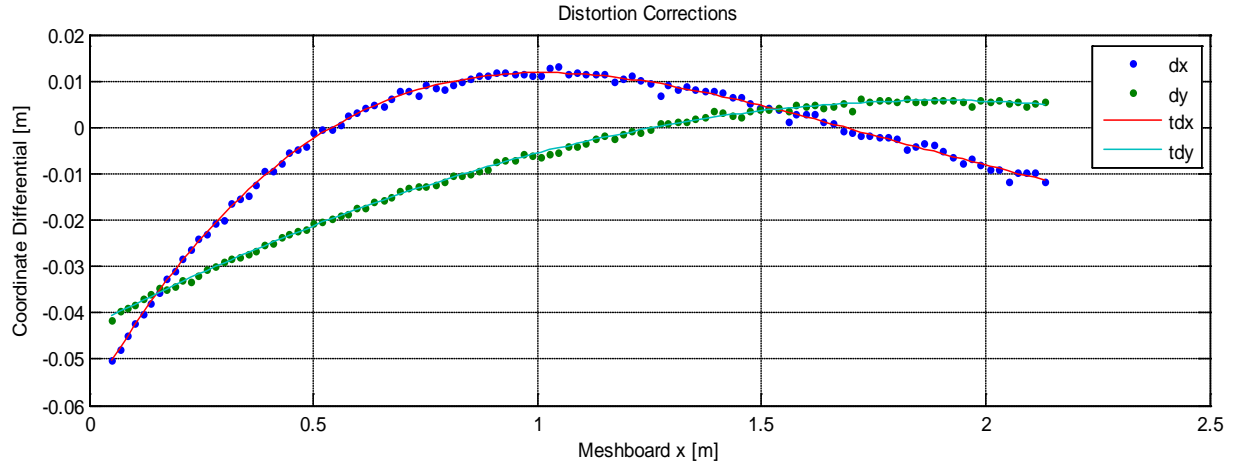


Figure A2-3. Coordinate differentials and distortion correction factors.

APPENDIX C SELECTED MATLAB SCRIPTS

Fit a Plane and Level a Point Cloud

planefit.m

```
%fit plane
clear all
close all
clc

%Load XYZ Point Cloud File

data=load('F:\TEMP Juan Backup\68 Roughness
Calibration\CoastalLab_floor_FF\xyz\CoastalLab_floor_FF_CropB.xyz');
sized=size(data);
npoints=(sized(1));

minx=min(data(:,1))
miny=min(data(:,2))
meanz=mean(data(:,3))

%Fit a plane to the Points Z=aX+bY+c
X=data(:,1);
Y=data(:,2);
Z=data(:,3);
obs=[X,Y,ones(npoints,1)];

par=obs\Z %par=[a;b;c]

%Residuals
res=obs*par-Z;
res2=res.*res;
rms=sqrt(sum(res2)/npoints)

%Normal Vector

NV=[par(1);par(2);-1]

%Rotations to level the plane

Rx=atan(par(2)/-1)
Ry=-1*atan(par(1)/-1)

Rxdeg=Rx*180/pi()
Rydeg=Ry*180/pi()
```

2D Detrending Function

detrend_fn_np.m

```
function [R2,rc] = detrend_fn_np(prf)
```

```

%
%Detrend
%USAGE: [c1,R2exp,R2exp2l,R2gau,R2gau2l,n0,R2pls,R2pls2l] =
detrend_fn_np(prf)
%Input (prf) 2D vector
%Output

[npoints,ncols]=size(prf);%Number of points & Number of Columns
sspace=prf(2,1)-prf(1,1);% Sample or Grid Space

%Detrend
%First order
par_1=[prf(:,1),ones(npoints,1)]\prf(:,2); %Trend Parameters
t_1=prf(:,1)*par_1(1)+par_1(2); % Z values Trend
rc_1=prf(:,2)-t_1;% Z Random Component
R2_1=1-(rc_1'*rc_1)/(var(prf(:,2))*npoints);%R2 of trend

%Second order
par_2=[prf(:,1).^2,prf(:,1),ones(npoints,1)]\prf(:,2);
t_2=prf(:,1).^2*par_2(1)+prf(:,1)*par_2(2)+par_2(3);
rc_2=prf(:,2)-t_2;
R2_2=1-(rc_2'*rc_2)/(var(prf(:,2))*npoints);

%FFT filter
nfsamples=round(sspace*(npoints-1));
prf_f=fft(prf(:,2));
prf_fm=prf_f;
prf_fm(1:nfsamples+1)=0;
prf_fm(npoints-nfsamples+1:npoints)=0;
rc_f=real(ifft(prf_fm));
t_f=prf(:,2)-rc_f;
R2_f=1-(rc_f'*rc_f)/(var(prf(:,2))*npoints);

%Group Output
R2=[R2_1,R2_2,R2_f];
rc=[rc_1,rc_2,rc_f];

```

2D Roughness Parameters Determination Function

```

acf_fn_np.m

function [acf_res] = acf_fn_np(acf)
%
%ACF Analysis function
%USAGE: [c1,R2exp,R2exp2l,R2gau,R2gau2l,n0,R2pls,R2pls2l] = acf_fn(acf)
%Input (acf) normalized ACF in 2 cols, first lags
%Output

clear i0;
clear icl;

[npoints,ncols]=size(acf);

```

```

%Determine correlation length
i0=ceil(npoints/2)+1;
icl=ceil(npoints/2);
while acf(icl,2)>=1/exp(1);%find the 1/e crossing point
    icl=icl+1;
end
cl=interp1(acf(icl-1:icl,2),acf(icl-1:icl,1),1/exp(1));%Correlation Length

%Build ACF
expacf=exp(-1*abs(acf(:,1))/cl);%exponential autocorrelation function
gauacf=exp(-1*(acf(:,1).*acf(:,1))/cl^2);%Gaussian Autocorrelation function

diffexp=expacf-acf(:,2);
R2exp=1-(diffexp'*diffexp)/((std(acf(:,2)))^2*npoints);
%R2exp2l=1-(diffexp(i0-1:icl)'*diffexp(i0-1:icl))/(acf(i0-1:icl,2)'*acf(i0-1:icl,2));
R2exp2l=1-(diffexp(2*i0-icl-2:icl)'*diffexp(2*i0-icl-2:icl))/((std(acf(2*i0-icl-2:icl,2)))^2*(2*(icl-i0)+3));

diffgau=gauacf-acf(:,2);
R2gau=1-(diffgau'*diffgau)/((std(acf(:,2)))^2*npoints);
%R2gau2l=1-(diffgau(i0-1:icl)'*diffgau(i0-1:icl))/(acf(i0-1:icl,2)'*acf(i0-1:icl,2));
R2gau2l=1-(diffgau(2*i0-icl-2:icl)'*diffgau(2*i0-icl-2:icl))/((std(acf(2*i0-icl-2:icl,2)))^2*(2*(icl-i0)+3));

%Fit the Power Law Spectrum

n0=1.5; %Initial Guess
dn=0.2;
obs=(acf(:,2));

while abs(dn)>0.05;

    Un=(abs(acf(:,1))/cl).^n0;
    cmp=exp(-1*Un);
    dfdn=-1.*cmp.*Un.*log(abs(acf(:,1))/cl);
    dn=dfdn(i0:icl+1,1)\(obs(i0:icl+1,1)-cmp(i0:icl+1,1));

    n0=n0+dn;

end

Un=(abs(acf(:,1))/cl).^n0;
cmp=exp(-1*Un);

diffpls=cmp-acf(:,2);
R2pls=1-(diffpls'*diffpls)/((std(acf(:,2)))^2*npoints);
%R2pls2l=1-(diffpls(i0-1:icl)'*diffpls(i0-1:icl))/(acf(i0-1:icl,2)'*acf(i0-1:icl,2));
R2pls2l=1-(diffpls(2*i0-icl-2:icl)'*diffpls(2*i0-icl-2:icl))/((std(acf(2*i0-icl-2:icl,2)))^2*(2*(icl-i0)+3));

```

```
%Concatenate results
acf_res=[c1,R2exp,R2exp21,R2gau,R2gau21,n0,R2pls,R2pls21];
```

2D Accuracy Assessment with Roughness References

```
cal_v2_05_20mm_1cm_ABCD.m
```

```
clear all;
clc;
close all;
```

```
%Load Referece Profile
```

```
ref=load('C:\Dissertation\Data\calibration\20mmRMS_1cmCL_ABCD\20mmRMS_1cmCL_A
BCD_ref.txt');
sizeref=size(ref);
nrefpt=sizeref(1);
refsp=(ref(2,1)-ref(1,1));
```

```
%Load Meshboard data
```

```
mbd=load('C:\Dissertation\Data\calibration\20mmRMS_1cmCL_ABCD\20mmRMS_1cmCL_A
BCD_mbcor.txt');
sized=size(mbd);
npoints=(sized(1));
%Obtain extremes
minx=min(mbd(:,1));
maxx=max(mbd(:,1));
miny=min(mbd(:,2));
maxy=max(mbd(:,2));
```

```
%Load LiDAR Derived Grid
```

```
X=load('C:\Dissertation\Data\calibration\20mmRMS_1cmCL_ABCD\9mmbins2\X.grd');
%FOR BINS
Y=load('C:\Dissertation\Data\calibration\20mmRMS_1cmCL_ABCD\9mmbins2\Y.grd');
Z=load('C:\Dissertation\Data\calibration\20mmRMS_1cmCL_ABCD\9mmbins2\Zmax.grd
');
```

```
gsize=size(X);
nrows=gsize(1);
ncols=gsize(2);
grdsp_l=X(1,2)-X(1,1);
```

```
%Extract Profiles
```

```
frow=21;%%%%UPDATE THIS
startc=10;%%AND THIS
endc=265;%%AND THIS
cbefore=startc-1;
cafter=ncols-endc;
```

```
procl=[X(frow,1:ncols-cbefore-
cafter);(Z(frow,startc:endc)+Z(frow+1,startc:endc))/2];%Selected Profile
%procl=[X(frow,1:ncols-cbefore-cafter);Z(frow,startc:endc)];%Selected
Profile
```

```

%procl=[X(frow,:);(Z(frow,:)+Z(frow+1,:))/2]';%Selected Profile

%%%Detrend Profiles
%Reference
param_ref=[ref(:,1),ones(nrefpt,1)]\ref(:,2);%[m,b], [X 1]\Y
tr_ref=ref(:,1)*param_ref(1)+param_ref(2);
randc_rf=ref(:,2)-tr_ref;

%Meshboard
param_mb=[mbd(:,1),ones(npoints,1)]\mbd(:,2);%[m,b], [X 1]\Y
tr_mb=mbd(:,1)*param_mb(1)+param_mb(2);
randc_mb=mbd(:,2)-tr_mb;

%Interpolate Random Component Meshboard Data
grdsp=(maxx-minx)/nrefpt;%Gridspacing
xvec=(minx:grdsp:maxx)';
%randc_mb_g=interp1(mbd(:,1),randc_mb,xvec);%Linea Interpolation
randc_mb_g=interp1(mbd(:,1),randc_mb,xvec,'nearest');
ngrid=size(xvec);
nsamples=ngrid(1,1);

%LiDAR
%param_l=[procl(:,1),ones(ncols,1)]\procl(:,2);%[m,b], [X 1]\Y
param_l=[procl(:,1),ones(ncols-cbefore-cafter,1)]\procl(:,2);%[m,b], [X 1]\Y
FOR BINS
tr_l=procl(:,1)*param_l(1)+param_l(2);
randc_l=procl(:,2)-tr_l;

%%Compute RMS of Height
%Reference
std_ref=std(randc_rf,1)% Standard Deviation

%Meshboard
std_mb=std(randc_mb,1)
std_mb_g=std(randc_mb_g,1)

%LiDAR
std_l=std(randc_l,1)

%%Compute R2
%Meshboard wrt to Reference
diff_mb=randc_mb-randc_rf;
R2_mb=1-(diff_mb'*diff_mb)/(std_mb^2*npoints)

%LiDAR wrt to Reference
diff_l=randc_l-randc_rf;
R2_l=1-(diff_l'*diff_l)/(std_l^2*nrefpt)

```

```

%Compute Correlation Coefficient
%Mesboard Reference
ccm_mbrf=corrcoef(randc_rf,randc_mb);
cc_mb=ccm_mbrf(1,2)

%Lidar Reference
ccm_lrf=corrcoef(randc_rf,randc_l);
cc_l=ccm_lrf(1,2)

%%Compute AutoCorrelation

%Reference
hcorr_ref=xcorr(randc_rf);
maxhcorr_ref=max(hcorr_ref);
nhcorr_ref=1/maxhcorr_ref*hcorr_ref;
lagsv_ref=((-1*nrefpt+1):1:(nrefpt-1))*refsp';
i_ref=nrefpt;
while nhcorr_ref(i_ref)>=1/exp(1);%find the 1/e crossing point
    i_ref=i_ref+1;
end
corl_ref=interp1(nhcorr_ref(i_ref-1:i_ref,1),lagsv_ref(i_ref-1:i_ref,1),1/exp(1))%Correlation Length
% expaf_mb=exp(-1*abs(lagsv_mb)/corl_mb);%exponential autocorrelation
function
% gauaf_mb=exp(-1*(lagsv_mb.*lagsv_mb)/corl_mb^2);%Gaussian Autocorrelation
function

%Meshboard
hcorr_mb=xcorr(randc_mb_g);
maxhcorr_mb=max(hcorr_mb);
nhcorr_mb=1/maxhcorr_mb*hcorr_mb;
lagsv_mb=((-1*nsamples+1):1:(nsamples-1))*(xvec(2,1)-xvec(1,1))';
i_mb=nsamples;
while nhcorr_mb(i_mb)>=1/exp(1);%find the 1/e crossing point
    i_mb=i_mb+1;
end
corl_mb=interp1(nhcorr_mb(i_mb-1:i_mb,1),lagsv_mb(i_mb-1:i_mb,1),1/exp(1))%Correlation Length
% expaf_mb=exp(-1*abs(lagsv_mb)/corl_mb);%exponential autocorrelation
function
% gauaf_mb=exp(-1*(lagsv_mb.*lagsv_mb)/corl_mb^2);%Gaussian Autocorrelation
% function

%
% %%LiDAR
hcorr_l=xcorr(randc_l);
maxhcorr_l=max(hcorr_l);
nhcorr_l=1/maxhcorr_l*hcorr_l;

%lagsv_l=((-1*(ncols)+1):1:(ncols-1))*grdsp_l;
%i_l=(ncols);

```

```

lagsv_l=(-1*(ncols-cbefore-cafter)+1):1:(ncols-cbefore-cafter-1))*grdsp_l;%
FOR BINS
i_l=(ncols-cbefore-cafter);

while nhcorr_l(i_l)>=1/exp(1);%find the 1/e crossing point
    i_l=i_l+1;
end
corl_l=interp1(nhcorr_l(i_l-1:i_l,1),lagsv_l(1,i_l-
1:i_l),1/exp(1))%Correlation Length
% expaf_l=exp(-1*abs(lagsv_l)/corl_l);%exponential autocorrelation function
% gauaf_l=exp(-1*(lagsv_l.*lagsv_l)/corl_l^2);%Gaussian Autocorrelation
function

%%%%%%%%%%%%%
%Plot Data

figure(1);
set(gcf, 'Color', [1,1,1]);
subplot(4,1,1)
plot(ref(:,1),ref(:,2))
title('Reference Profile');
xlabel('Length [m]');
ylabel('Height [m]');
axis ([0 2.5 0.9*min(ref(:,2)) 1.1*max(ref(:,2))]);
grid;

subplot(4,1,2)
plot(mbd(:,1),mbd(:,2))
title('Profile from Meshboard');
xlabel('Length [m]');
ylabel('Height [m]');
axis ([0 2.5 0.9*min(ref(:,2)) 1.1*max(ref(:,2))]);
grid;

subplot(4,1,3)
imagesc([X(1,1),X(1,ncols)], [Y(1,1),Y(nrows,1)], Z);
title('Gridded Surface from LiDAR')
%imagesc([minx,maxx],[miny,maxy],intth);
xlabel('Length [m]');
ylabel('Depth [m]');
axis xy;
axis image;
%colorbar;

subplot(4,1,4)
plot(procl(:,1),procl(:,2))
title('Extracted Profile from LiDAR Grid');
xlabel('Length [m]');
ylabel('Height [m]');
axis ([0 2.5 min(min(Z)) max(max(Z))]);
grid;

figure(2)
set(gcf, 'Color', [1,1,1]);

```

```

plot(ref(:,1),randc_rf,xvec,randc_mb_g);
title('Random Component extracted from profiles');
legend('Reference','Meshboard');
xlabel('Length [m]');
ylabel('Height [m]');
grid

figure(3)
set(gcf,'Color',[1,1,1]);
plot(ref(:,1),randc_rf,ref(:,1),randc_mb);
title('Random Component extracted from profiles - Reference X');
legend('Reference','Meshboard');
xlabel('Length [m]');
ylabel('Height [m]');
grid

figure(4)
set(gcf,'Color',[1,1,1]);
plot(ref(:,1),randc_rf,procl(:,1),randc_l);
title('Random Component extracted from profiles');
legend('Reference','LiDAR');
xlabel('Length [m]');
ylabel('Height [m]');
grid

figure(5)
set(gcf,'Color',[1,1,1]);
plot(ref(:,1),randc_rf,ref(:,1),randc_l);
title('Random Component extracted from profiles- Reference X');
legend('Reference','LiDAR');
xlabel('Length [m]');
ylabel('Height [m]');
grid

figure(6);%AutoCorrelation Functions
set(gcf,'Color',[1,1,1]);
plot(lagsv_ref,nhcorr_ref,lagsv_mb,nhcorr_mb,lagsv_l,nhcorr_l)
line([-2.4 2.4],[1/exp(1) 1/exp(1)],'Color',[0 0 0])%1/e axis line
grid;
xlabel('X Lags [Meters]');
ylabel('Normalized AutoCorr');
title('Height AutoCorrelation');
axis ([-2.4 2.4 -0.2 1.2]);
legend('Reference','Meshboard','LiDAR');

figure(7);% Difference
set(gcf,'Color',[1,1,1]);
plot(ref(:,1),diff_mb,ref(:,1),diff_l);
title('Height Difference wrt Reference not considering x');
legend('Meshboard','LiDAR');
grid;

```

3D Correlation Length from DEMs

```
plotterraincorr.m

close all;
clear all;
clc;

%Define Path
path='C:\Dissertation\Data\20060308\Sample4x4\10mmgrids\';
%path='C:\Dissertation\Data\200711SL\10mmGrids\';

%Load data files
xgrid=load(strcat(path,'X.grd'));
ygrid=load(strcat(path,'Y.grd'));
zgrid=load(strcat(path,'Z2dtdr.grd'));
%zgrid=load(strcat(path,'Z2dt.grd'));
corrgrid=load(strcat(path,'xcorZ2dtdr.grd'));
%corrgrid=load(strcat(path,'xcorZ2dt.grd'));
sizearray=size(xgrid);
ncol=sizearray(2);
nrows=sizearray(1);

%Derive Plot Limits
minx=xgrid(1,1);
maxx=xgrid(1,ncol);
miny=ygrid(1,1);
maxy=ygrid(nrows,1);
maxcorr=corrgrid(nrows,ncol);
gridspc=xgrid(1,2)-xgrid(1,1);

%Compute grid Height Mean and RMS
meanz=mean(mean(zgrid));
meanzgrid=meanz*ones(nrows,ncol);
hdiffgrid=zgrid-meanzgrid;
sdiffgrid=hdiffgrid.*hdiffgrid;
rmshg=sqrt(mean(mean(sdiffgrid)))

%Compute normalized Auto Correlation
nrncorr=1/maxcorr*corrgrid;

%Create x & y grids for Coorelation Array
[Xcor,Ycor] = meshgrid((-1*(ncol-1)):1:(ncol-1),-1*(nrows-1):1:(nrows-1));

%test Contour Def

[ctest,hctest]=contour(nrncorr,[1/exp(1) 1/exp(1)]);
sizectestv=size(ctest);
npcnt=sizectestv(2);

%Obtain contour in absolute coordinates
orix=ncol*ones(1,npcnt);
```

```

oriy=nrows*ones(1,npcnt);

fncntr=[(ctest(1,:)-orix)',(ctest(2,:)-oriy)']*gridspc;%Final Contour
fncntr(1,:)=[];%Remove First countour point

% Compute Contour Distance vectors & Mean Distance
%Distance to Each Point on the Coutour
corlvec=sqrt((ctest(1,:)-orix).^2+(ctest(2,:)-oriy).^2);% grid Units
clvt=corlvec'*gridspc;%in Meters
ang=(rad2deg(atan2(ctest(2,:)-oriy,ctest(1,:)-orix)))';

%Remove Elements
clvt(1,:)=[];
ang(1,:)=[];
%clvt(469,:)=[];
%ang(469,:)=[];

%Obtain Results
meancorl=mean(corlvec);
stdcorl=std(corlvec);

% Results [min max mean std]
RES=gridspc*[min(corlvec(1,2:npcnt)),max(corlvec(1,2:npcnt)),mean(corlvec(1,2:npcnt)),std(corlvec(1,2:npcnt))]

binmin=floor(meancorl-2*stdcorl);
binsize=round(((meancorl+2*stdcorl)-(meancorl-2*stdcorl))/40);
binvec=binmin:binsize:binsize*42+binmin;

%dlmwrite(strcat(path,'CorlV_ZFdtdr.txt'), [ang,clvt], 'delimiter', '
','newline', 'pc','precision', 6);

%Plot Graphics

figure(2);
set(gcf, 'Color',[1,1,1]);
subplot(1,2,1)
imagesc([minx,maxx],[miny,maxy],zgrid);
title('Terrain Height');
axis xy;
axis image;
colorbar;
xlabel('X [Meters]')
ylabel('Y [Meters]')

subplot(1,2,2)
imagesc([-1*ncol*gridspc,ncol*gridspc],[-1*nrows*gridspc,nrows*gridspc],nrmcorr);
title('Height Autocorrelation');
axis xy;

```

```

axis image;
colorbar;
xlabel('X Lags [Grid units]')
ylabel('Y Lags [Grid units]')

figure(7);
set(gcf, 'Color', [1,1,1]);
subplot(1,2,1)
plot(fncntr(:,1),fncntr(:,2))
axis([-1*ncol*gridspc,ncol*gridspc,-1*nrows*gridspc,nrows*gridspc])
xlabel('X Lags [m]');
ylabel('Y Lags [m]');

subplot(1,2,2)
plot(ang,clvt, '.')
xlabel('Angle from the X axis [deg]');
ylabel('Correlation length [m]');

```

RMS_h from Single Scan Line from Airborne LiDAR Data

AbPC_Rssl_v1.m

```

clear all;
close all;
clc;

%Define Desired Profile Length
pl=3;

%Load Pointcloud data
pc=load('C:\Dissertation\Data\20100902_Airborne\Strip009\S1C1_ascii_245b_009-1_c.txt');
%1 Time, 2 Easting, 3 Northing, 4 Height, 5 Intensity, 6 Range, 7 ScanAngle
[npoints,ncols]=size(pc);

%Create Empty arrays
RMSh=NaN(npoints,1);

%Extract Arrays
xy1=pc(1:npoints-1,2:3);
xy2=pc(2:npoints,2:3);

%Compute Distance
dist=sqrt((xy2(:,1)-xy1(:,1)).^2+(xy2(:,2)-xy1(:,2)).^2);
mdist=mean(dist);

%Compute scan angle difference between successive points
dsa=diff(pc(:,7));

%Determine number of points in profile
npp=pl/mdist;
npph=ceil(npp/2-1);

```

```

%Cycle through Point Cloud

for i=npph+1:(npoints-npph);

    %obtain vectors
    hv=pc(i-npph:i+npph,4);

    % create displacement vector
    dv=zeros(npsh*2+1,1);

    for j=2:npsh*2+1
        dv(j)=dv(j-1)+dist(i-npph+j-2);
    end

    %linear detrend of profile
    par=[dv,ones(npsh*2+1,1)]\hv;%aD+b=Z
    tr=par(1)*dv+par(2)*ones(npsh*2+1,1);

    %Obtain RMSH
    RMSH(i)=std(hv-tr);

end

%Fill first and last values
RMSH(1:npsh)=RMSH(npsh+1);
RMSH(npoints-npph+1:npoints)=RMSH(npoints-npph);

%Write XYZis PC
%dlmwrite('C:\Dissertation\Data\20100902_Airborne\Strip009\245b_009-
1_c_xyzis.xyz', [pc(:,2:5),RMSH],'delimiter',' ','newline','pc','precision',
10, '-append');

```

Meshboard Digitizing and Correction

```

meshboard_C.m

%Mesboard Digitization and Distortion Correction

clear all;
close all;
clc;
tic;

%Set Path
path='C:\Dissertation\Data\20100903\20100903_PD&MA\';
outnm='PD&MA_A';

%Load Image

```

```

MBimg=imread(strcat(path,'IMG_9733.JPG'));
imshow(MBimg);
imsize=size(MBimg);
imrows=imsize(1);
imcols=imsize(2);

%Display Image
figure(1);
set(gcf,'Color',[1,1,1]);
imshow(MBimg);

%Get Corners of ROI
%Top Left and Bottom Right points around:
%1,2. MB TL corner
%3,4. MB TR corner
%5,6. Mark @ 100,41
%7,8. Mark @ 10,51
%9,10. Mark @ 200,11
%11,12. Profile Extremes
[xc, yc] = getpts;
controlp=fix([xc,yc]);

%%%%%%%%%%%%%%%%%%%%%%%%%%%%%%%%%%%%%%%%%%%%%%%%%%%%%%%%%%%%%%%%%%%%%%%%
%Display Subimages to obtain control points
%Control Point 1
close all;
figure(1);
set(gcf,'Color',[1,1,1]);
imshow(MBimg(controlp(1,2):controlp(2,2),controlp(1,1):controlp(2,1),:));
[xc1, yc1] = getpts;

%Control Point 2
close all;
figure(1);
set(gcf,'Color',[1,1,1]);
imshow(MBimg(controlp(3,2):controlp(4,2),controlp(3,1):controlp(4,1),:));
[xc2, yc2] = getpts;

%Control Point 3
close all;
figure(1);
set(gcf,'Color',[1,1,1]);
imshow(MBimg(controlp(5,2):controlp(6,2),controlp(5,1):controlp(6,1),:));
[xc3, yc3] = getpts;

%Control Point 4
close all;
figure(1);
set(gcf,'Color',[1,1,1]);
imshow(MBimg(controlp(7,2):controlp(8,2),controlp(7,1):controlp(8,1),:));
[xc4, yc4] = getpts;

%Control Point 5
close all;
figure(1);
set(gcf,'Color',[1,1,1]);

```

```

imshow(MBimg(controlp(9,2):controlp(10,2),controlp(9,1):controlp(10,1),:));
[xc5, yc5] = getpts;

%Single scale
scf=2.1336/sqrt((xc2+xc(3)-xc1-xc(1))^2+(yc2+yc(3)-yc1-yc(1))^2);%m/pixel

%Affine Transformation Parameters
%X=Ay+Bx+C
%Y=Dy+Ex+F
%X,Y Real Coordinates, x,y Pixel Coordinates
CPC=[0;0.9144;2.1336;0.9144;1;.41;.1;.51;2;.11];
Amat=[yc1+yc(1),xc1+xc(1),1,0,0,0;
      0,0,0,yc1+yc(1),xc1+xc(1),1;
      yc2+yc(3),xc2+xc(3),1,0,0,0;
      0,0,0,yc2+yc(3),xc2+xc(3),1;
      yc3+yc(5),xc3+xc(5),1,0,0,0;
      0,0,0,yc3+yc(5),xc3+xc(5),1;
      yc4+yc(7),xc4+xc(7),1,0,0,0;
      0,0,0,yc4+yc(7),xc4+xc(7),1;
      yc5+yc(9),xc5+xc(9),1,0,0,0;
      0,0,0,yc5+yc(9),xc5+xc(9),1];

param=Amat\CPC;
%[A B C D E F]'

%# Pixels Meshboard Profile
npixels=controlp(12,1)-controlp(11,1);

npixelinc=floor(npixels/6);

%%%%%%%%%%%%%%%%%%%%%%%%%%%%%%%%%%%%%%%%%%%%%%%%%%%%%%%%%%%%%%%%%%%%%%%%
%Display Subimages to obtain Profile points
%Profile Fragment 1/6
close all;
figure(1);
set(gcf,'Color',[1,1,1]);
imshow(MBimg(controlp(11,2):controlp(12,2),controlp(11,1):controlp(11,1)+npixelinc,:));
[xp1, yp1] = getpts;

%Profile Fragment 2/6
close all;
figure(2);
set(gcf,'Color',[1,1,1]);
imshow(MBimg(controlp(11,2):controlp(12,2),controlp(11,1)+npixelinc:controlp(11,1)+npixelinc*2,:));
[xp2, yp2] = getpts;

%Profile Fragment 3/6
close all;
figure(3);
set(gcf,'Color',[1,1,1]);
imshow(MBimg(controlp(11,2):controlp(12,2),controlp(11,1)+npixelinc*2:controlp(11,1)+npixelinc*3,:));
[xp3, yp3] = getpts;

```

```

%Profile Fragment 4/6
close all;
figure(4);
set(gcf, 'Color', [1,1,1]);
imshow(MBimg(controlp(11,2):controlp(12,2),controlp(11,1)+npixelinc*3:control
p(11,1)+npixelinc*4,:));
[xp4, yp4] = getpts;

%Profile Fragment 5/6
close all;
figure(5);
set(gcf, 'Color', [1,1,1]);
imshow(MBimg(controlp(11,2):controlp(12,2),controlp(11,1)+npixelinc*4:control
p(11,1)+npixelinc*5,:));
[xp5, yp5] = getpts;

%Profile Fragment 6/6
close all;
figure(6);
set(gcf, 'Color', [1,1,1]);
imshow(MBimg(controlp(11,2):controlp(12,2),controlp(11,1)+npixelinc*5:control
p(11,1)+npixelinc*6,:));
[xp6, yp6] = getpts;

%Concatenate Profile Points in Pixel Coordinates
ppcoor=[xp1+xc(11),yp1+yc(11);xp2+xc(11)+npixelinc*1,yp2+yc(11);xp3+xc(11)+np
ixelinc*2,yp3+yc(11);xp4+xc(11)+npixelinc*3,yp4+yc(11);xp5+xc(11)+npixelinc*4
,yp5+yc(11);xp6+xc(11)+npixelinc*5,yp6+yc(11)];

%Final Profile Points in MB Coordinates
fp=[ppcoor*[param(2);param(1)]+param(3),ppcoor*[param(5);param(4)]+param(6)];

%Single Scale
ssp=scf*[ppcoor(:,1)-min(ppcoor(:,1)),max(ppcoor(:,2))-ppcoor(:,2)];

%%%%%%%%%%%%%%%%%%%%%%%%%%%%%%%%%%%%%%%%%%%%%%%%%%%%%%%%%%%%%%%%%%%%%%%%
%Display Subimages to obtain correction line
%Profile Fragment 1/6
close all;
figure(1);
set(gcf, 'Color', [1,1,1]);
imshow(MBimg(controlp(11,2):controlp(12,2),controlp(11,1):controlp(11,1)+npix
elinc,:));
[xl1, yl1] = getpts;

%Profile Fragment 2/6
close all;
figure(2);
set(gcf, 'Color', [1,1,1]);
imshow(MBimg(controlp(11,2):controlp(12,2),controlp(11,1)+npixelinc:controlp(
11,1)+npixelinc*2,:));
[xl2, yl2] = getpts;

```

```

%Profile Fragment 3/6
close all;
figure(3);
set(gcf, 'Color', [1,1,1]);
imshow(MBimg(controlp(11,2):controlp(12,2),controlp(11,1)+npixelinc*2:control
p(11,1)+npixelinc*3,:));
[xl3, yl3] = getpts;

%Profile Fragment 4/6
close all;
figure(4);
set(gcf, 'Color', [1,1,1]);
imshow(MBimg(controlp(11,2):controlp(12,2),controlp(11,1)+npixelinc*3:control
p(11,1)+npixelinc*4,:));
[xl4, yl4] = getpts;

%Profile Fragment 5/6
close all;
figure(5);
set(gcf, 'Color', [1,1,1]);
imshow(MBimg(controlp(11,2):controlp(12,2),controlp(11,1)+npixelinc*4:control
p(11,1)+npixelinc*5,:));
[xl5, yl5] = getpts;

%Profile Fragment 6/6
close all;
figure(6);
set(gcf, 'Color', [1,1,1]);
imshow(MBimg(controlp(11,2):controlp(12,2),controlp(11,1)+npixelinc*5:control
p(11,1)+npixelinc*6,:));
[xl6, yl6] = getpts;

%Concatenate Line Points in Pixel Coordinates
lpcoor=[xl1+xc(11),yl1+yc(11);xl2+xc(11)+npixelinc*1,yl2+yc(11);xl3+xc(11)+np
ixelinc*2,yl3+yc(11);xl4+xc(11)+npixelinc*3,yl4+yc(11);xl5+xc(11)+npixelinc*4
,yl5+yc(11);xl6+xc(11)+npixelinc*5,yl6+yc(11)];

%Final Line Points in MB Coordinates
fl=[lpcoor*[param(2);param(1)]+param(3),lpcoor*[param(5);param(4)]+param(6)];

disp('Time to process Mesboard Image')
toc

%%%%%%%%%%%%%%%%%%%%%%%%%%%%%%%%%%%%%%%%%%%%%%%%%%%%%%%%%%%%%%%%%%%%%%%%Correct Profile for Distortions

ref=fl;% Correction Reference Line Coordinates
prof=fp;% Digitized Profile coordinates
[nrefpt,ncols]=size(ref);

%Create reference Vectors
Xref=(0:.02:(nrefpt-1)*.02)';
Yref=0.11*ones(nrefpt,1);%%%%%%%%UPDATE THIS WITH PROPER REFERENCE LINE
dx=Xref-ref(:,1);%X-x=dx
dy=Yref-ref(:,2);%Y-y=dy

```

```

%Obtain Correction Polynomials
%dx 6th order polynomial Ax^6+Bx^5+Cx^4+Dx^3+Ex^2+Fx+G
param_dx=[ref(:,1).^6,ref(:,1).^5,ref(:,1).^4,ref(:,1).^3,ref(:,1).^2,ref(:,1)
),ones(nrefpt,1)]\dx;%[A,B,C,D,E,F,G]
tr_dx=ref(:,1).^6*param_dx(1)+ref(:,1).^5*param_dx(2)+ref(:,1).^4*param_dx(3)
+ref(:,1).^3*param_dx(4)+ref(:,1).^2*param_dx(5)+ref(:,1)*param_dx(6)+param_d
x(7);

%dy 3th order polynomial Ax^3+Bx^2+Cx+D
param_dy=[ref(:,1).^3,ref(:,1).^2,ref(:,1),ones(nrefpt,1)]\dy;%[A,B,C,D]
tr_dy=ref(:,1).^3*param_dy(1)+ref(:,1).^2*param_dy(2)+ref(:,1)*param_dy(3)+pa
ram_dy(4);

%Correct Profile
X=prof(:,1)+prof(:,1).^6*param_dx(1)+prof(:,1).^5*param_dx(2)+prof(:,1).^4*pa
ram_dx(3)+prof(:,1).^3*param_dx(4)+prof(:,1).^2*param_dx(5)+prof(:,1)*param_d
x(6)+param_dx(7);
Y=prof(:,2)+prof(:,1).^3*param_dy(1)+prof(:,1).^2*param_dy(2)+prof(:,1)*param
_dy(3)+param_dy(4);

%%% Plots
%Final Profile Pixel Coordinates
close all;
figure(1);
set(gcf, 'Color',[1,1,1]);
plot(ppcoor(:,1),ppcoor(:,2),lpcoor(:,1),lpcoor(:,2));
title('Pixel Coordinates')
xlabel('MBx [pixels]');
ylabel('MBy [Pixels]');
legend('Affine Profile', 'Cor Line')

figure(2);
set(gcf, 'Color',[1,1,1]);
plot(ssp(:,1),ssp(:,2),fp(:,1),fp(:,2),fl(:,1),fl(:,2),X,Y);
title('MB Coordinates')
xlabel('MBx [m]');
ylabel('MBy [m]');
legend('Single Sc', 'Affine', 'Cor Line', 'Corrected')

figure(3)
set(gcf, 'Color',[1,1,1]);
plot(ref(:,1),dx,ref(:,1),dy,ref(:,1),tr_dx,ref(:,1),tr_dy);
title('Distortion Corrections');
legend('dx', 'dy', 'tdx', 'tdy');
xlabel('x [m]');
ylabel('y [m]');
grid

%%%%%%%%%%%%%%%%%%%%%%%%%%%%%%%%%%%%%%%%%%%%%%%%%%%%%%%%%%%%%%%%%%%%%%%%
%Write Output Files
%_mbor for original, %_mbdxdy for Correction , %_mbcor for corrected
dlmwrite(strcat(path,outnm,'_mbor.txt'), fp, 'delimiter', ' ', 'newline',
'pc','precision', 5);% Distorted Profile

```

```

dlmwrite(strcat(path,outnm,'_mbss.txt'), ssp, 'delimiter', ' ', 'newline',
'pc','precision', 5);% Distorted Profile
dlmwrite(strcat(path,outnm,'_mbdxdy.txt'), fl, 'delimiter', ' ', 'newline',
'pc','precision', 5); %Reference Line
dlmwrite(strcat(path,outnm,'_mbcor.txt'), [X,Y], 'delimiter', ' ', 'newline',
'pc','precision', 5); %Corrected Profile

dlmwrite(strcat(path,outnm,'_rep.txt'), 'Affine Transformation Parameters',
'delimiter', ' ', 'newline', 'pc'); %Report
dlmwrite(strcat(path,outnm,'_rep.txt'), 'Ay+Bx+C ; Y=Dy+Ex+D ; [A B C D E F]',
'delimiter', ' ', 'newline', 'pc', '-append'); %Report
dlmwrite(strcat(path,outnm,'_rep.txt'), param , 'delimiter', ' ', 'newline',
'pc','precision', 5, '-append'); %Report
dlmwrite(strcat(path,outnm,'_rep.txt'), ' ', 'delimiter', ' ', 'newline',
'pc', '-append'); %Report
dlmwrite(strcat(path,outnm,'_rep.txt'), 'Single Scale' , 'delimiter', ' ',
'newline', 'pc', '-append'); %Report
dlmwrite(strcat(path,outnm,'_rep.txt'), scf , 'delimiter', ' ', 'newline',
'pc','precision', 5, '-append'); %Report
dlmwrite(strcat(path,outnm,'_rep.txt'), ' ', 'delimiter', ' ', 'newline',
'pc', '-append'); %Report
dlmwrite(strcat(path,outnm,'_rep.txt'), 'Correction Polynomials' ,
'delimiter', ' ', 'newline', 'pc', '-append'); %Report
dlmwrite(strcat(path,outnm,'_rep.txt'), 'dx = Ax^6+Bx^5+Cx^4+Dx^3+Ex^2+Fx+G',
'delimiter', ' ', 'newline', 'pc', '-append'); %Report
dlmwrite(strcat(path,outnm,'_rep.txt'), param_dx , 'delimiter', ' ',
'newline', 'pc','precision', 5, '-append'); %Report
dlmwrite(strcat(path,outnm,'_rep.txt'), 'dy = Ax^3+Bx^2+Cx+D' , 'delimiter',
' ', 'newline', 'pc', '-append'); %Report
dlmwrite(strcat(path,outnm,'_rep.txt'), param_dy , 'delimiter', ' ',
'newline', 'pc','precision', 5, '-append'); %Report

```

LIST OF REFERENCES

- [1] M.K. Shepard, B.A. Campbell, M.H. Bulmer, T.G. Farr, L.R. Gaddis, J.J. Plaut "The Roughness of Natural Terrain: A Planetary and Remote Sensing Perspective," *Journal of Geophysical Research*, Vol. 106, No. E12, pp 32,777–32,795, December 25, 2001
- [2] M. Callens, N.E.C. Verhoest, M.W.J. Davidson "Parameterization of Tillage-Induced Single-Scale Soil Roughness From 4-m Profiles," *IEEE Transactions on Geoscience and Remote Sensing*, vol.44, no.4, pp. 878–888, April 2006.
- [3] C.J. Dodds and J.D. Robson, "The Description of Road Surface Roughness," *Journal of Sound and Vibration*, 31 (2), pp. 175–183, 1973.
- [4] T.R. Thomas, "Characterization of Surface Roughness," *Precision Engineering*, vol. 3, iss. 2, pp. 97–104, April 1981
- [5] J. M. Bennett, "Recent Developments in Surface Roughness Characterization," *Measurement Science and Technology*, vol. 3, pg. 1119–1127, 1992.
- [6] M.S. Moran, C.D. Peters-Lidard, J. M. Watts, and S. McElroy, "Estimating soil moisture at the watershed scale with satellite-based radar and land surface models," *Canadian Journal of Remote Sensing*, Vol. 30, No. 5, pp. 805–826, 2004
- [7] N.E. Verhoest, H., Lievens, ; W. Wagner, J. Álvarez-Mozos, M..S. Moran, F. Mattia. "On the Soil Roughness Parameterization Problem in Soil Moisture Retrieval of Bare Surfaces from Synthetic Aperture Radar". *Sensors* 2008, 8, pp. 4213–4248, 2008.
- [8] W. Dierking, "Quantitative roughness characterization of geological surfaces and implications for radar signature analysis," *IEEE Transactions on Geoscience and Remote Sensing*, vol.37, no.5, pp. 2397–2412, September 1999.
- [9] F. T. Ulaby, R. K. Moore, A. K. Fung, "*Microwave Remote Sensing: Active and Passive*"; Artech House: Boston, MA, vol. II, ch 11, 1982.
- [10] J.A. Ogilvy and J.R. Foster, "Rough surfaces: Gaussian or exponential statistics?," *Journal of Physics D: Applied Physics*, vol. 22, pp. 1243–1251, 1989.
- [11] Q. Li, J. Shi, and K.S. Chen, "A general power law spectrum and its application to the backscattering of soil surfaces based on the integral equation model," *IEEE Transaction on Geoscience and Remote Sensing*, vol. 40, no. 2. February 2002.
- [12] M. Zribi, V. Ciarletti, O. Taconet, P. Boissard, M. Chapron, and B. Rabin, "Backscattering on soil structure described by plane facets." *International Journal on Remote Sensing*, vol. 21, no. 1, pp. 137–153, 2000.

- [13] F. Mattia, M.W.J. Davidson, T. Le Toan, C.M.F. D'Haese, N.E.C. Verhoest, A.M. Gatti, M. Borgeaud, "A comparison between soil roughness statistics used in surface scattering models derived from mechanical and laser profilers," *IEEE Transactions on Geoscience and Remote Sensing*, vol. 41, pp. 1659–1671, 2003.
- [14] M.L. Oelze, J.M. Sabatier, R. Raspert, Richard, "Roughness Measurements of Soil Surfaces by Acoustic Backscatter," *Soil Science Society of America Journal*, Vol. 67, pp. 241–250, 2003.
- [15] R. Bryant, M.S. Moran, D.P. Thoma, C.D. Holifield Collins, S. Skirvin, M. Rahman, K. Slocum, P. Starks, D. Bosch, M.P. González Dugo, "Measuring surface roughness height to parameterize radar backscatter models for retrieval of surface soil moisture," *IEEE Geoscience and Remote Sensing Letters*, vol. 4, no. 1, 2007.
- [16] P. Marzahn and R. Ludwig, "On the derivation of soil surface roughness from multi parametric PolSAR data and its potential for hydrological modeling," *Hydrology and Earth System Sciences*, 13, pg. 381–394, 2009.
- [17] L. Zhixiong, C. Nan, U.D. Perdok, W.B. Hoogmoed, "Characterization of Soil Profile Roughness," *Biosystems Engineering*, vol. 91, 369–377, 2005.
- [18] F. Darboux and C.H. Huang "An instantaneous-profile laser scanner to measure soil surface microtopography," *Soil Science Society of America Journal*, vol. 67, pp. 92–99, 2003
- [19] J. Fernandez-Diaz, "Scientific applications of the Mobile Terrestrial Laser Scanner (M-TLS) system," M.S. thesis, Department of Civil Engineering, University of Florida, Gainesville, Florida, 2007. Available: <http://purl.fcla.edu/fcla/etd/UFE0021101>
- [20] I.J. Davenport, J. Holden, R.J. Pentreath, "Derivation of soil surface properties from airborne laser altimetry," in *Proceedings of the International Geoscience and Remote Sensing Symposium (IGARSS '03)*, Toulouse, France, pp. 4389–4391, 2003.
- [21] I.J. Davenport, N. Holden, R.J., Gurney, "Characterizing errors in airborne laser altimetry data to extract soil roughness," *IEEE Transaction on Geoscience and Remote Sensing*, vol. 42, pp. 2130–2141, 2004.
- [22] C. Perez-Gutierrez, J.M. Martinez-Fernandez, N. Sanchez, J. Álvarez-Mozos, "Modeling of soil roughness using terrestrial laser scanner for soil moisture retrieval," in *Proceedings of the International Geoscience and Remote Sensing Symposium (IGARSS 2007)*, Barcelona, Spain, pp. 1877–1880, 2007.
- [23] M.J.M. Romkens and J.Y. Wang, "Effect of tillage on surface roughness," *Transactions of the ASAE*, vol. 29 (2), March–April, 1986.

- [24] N. Baghdadi, O. Cerdan, M. Zribi, V. Auzet, F. Darboux, M. El Hajj and R.B. Kheir, "Operational performance of current synthetic aperture radar sensors in mapping soil surface characteristics in agricultural environments; applications to hydrological and erosion modeling," *Hydrological Processes*, 22, pp. 9-20, 2008.
- [25] H. Lievens, H. Vernieuwe, J. Alvarez-Mozos, B. De Baets and N. Verhoest, "Error in radar-derived soil roughness parameterization: An analysis based on synthetical surface profiles," *Sensors*, 9, pp. 1067–1093, 2009.
- [26] D.P. Thoma, M.S. Moran, R. Bryant, M. Rahman, C.D. Holifield-Collins, S. Skirvin, E.E. Sano, and K. Slocum, "Comparison of four models to determine surface soil moisture from C-band radar imagery in a sparsely vegetated semiarid landscape," *Water Resources Research*, vol. 42, (1), pp. 1–12, 2006.
- [27] N. Baghdadi, I. Gherboudj, M. Zribi, M. Sahebi, C. King and F. Bonn, "Semi-empirical calibration of the IEM backscattering model using radar images and moisture and roughness field measurements," *International Journal of Remote Sensing*, vol 25, no. 18, pg. 3593–3623, September 2004.
- [28] N. Baghdadi, C. King and L. Bonnifait, "An empirical calibration of the Integral Equation Model based on SAR data and soil parameter measurements," , In *Proceedings of the International Geoscience and Remote Sensing Symposium (IGARSS 2002)*, vol.5., pp. 2646–2650, 2002.
- [29] U. Wandering, "Introduction to Lidar," in *Lidar: Range-Resolved Optical Remote Sensing of the Atmosphere*, C. Weitkamp, Ed. New York, Springer, pp. 1–18, 2005.
- [30] Carter, W. E., R. Shrestha and K.C. Slatton, 2007, "Geodetic Laser Scanning," *Physics Today*, Vol. 60, Number 12, pp 41–47, 2007.
- [31] K. C. Slatton, W. E. Carter, R. L. Shrestha and W. Dietrich, "Airborne Laser Swath Mapping: Achieving the resolution and accuracy required for geosurficial research," *Geophysical Research Letters*, Vol. 34, 2007.
- [32] Y. Oh and Y.C. Kay, "Condition for precise measurements of soil surface roughness," *IEEE Transactions on Geoscience and Remote Sensing*, vol. 36, no. 2, pp. 691–695, March 1998.
- [33] A.M. Gatti, F. Mattia, C.M.F. D'Haese, N.E.C. Verhoest, M.W.J. Davidson, T. Le Toan, M. Borgeaud, "A comparison between Laser, needle-like and meshboard techniques for soil roughness measurements," in *Proceedings of the 3rd International Symposium, 'Retrieval of Bio- and Geophysical parameters from SAR Data for Land Applications*, Sheffield, UK, 11–14 September 2001, ESA SP-475, January 2002.
- [34] J.A. Ogilvy, "Computer simulation of acoustic wave scattering from rough surfaces" *Journal of Physics D: Applied Physics*, vol. 21, pp. 260–277, 1988.

- [35] J. Casanova, L. Tzu-yun, L. Mi-young, J. Kai-Jen, C. Tien, J. Judge, O. Lanni, L. Miller "Field Observations During the Fourth Microwave Water and Energy Balance Experiment (MicroWEX-4): March 10 - June 14, 2005," IFAS report available: <http://edis.ifas.ufl.edu/AE362>
- [36] J. Mi-Young, C.T. Kai-Jen, J. Casanova, J. Judge, "Measurements of Soil Surface Roughness during the Fourth Microwave Water and Energy Balance Experiment from April 18 through June 13, 2005," IFAS report available: <http://edis.ifas.ufl.edu/AE363>
- [37] J. Casanova, F. Yan, J. Mi-young, J. Fernandez, J. Judge, C. Slatton, J. Kai-Jen, C. Tien, L. Tzu-yun, O. Lanni, L. Miller "Field Observations During the Fifth Microwave Water and Energy Balance Experiment: from March 9 through May 26, 2006," IFAS report available: <http://edis.ifas.ufl.edu/AE407>
- [38] M.W.J. Davidson, F. Mattia, G. Satalino, N. E. C. Verhoest, T. Le Toan, M. Borgeaud, J. M. B. Louis, E. Attema, "Joint Statistical Properties of RMS Height and Correlation Length Derived From Multisite 1-m Roughness Measurements," *IEEE Transactions on Geoscience and Remote Sensing*, vol. 41, no. 7, pp. 1651–1658, July 2003.
- [39] O. Taconet, V. Ciarletti, "Estimating soil roughness indices on a ridge-and-furrow surface using stereo photogrammetry," *Soil & Tillage Research*, vol. 93, pp. 64–76, 2007.
- [40] K. Fung, Z. Li, and K. S. Chen, "Backscattering from a randomly rough dielectric surface," *IEEE Transactions on Geoscience and Remote Sensing*, vol. 30, pp. 356–369, Mar. 1992.
- [41] K. S. Chen, S. Wu, L. Tsang, Q. Li, J. Shi, A. K. Fung, "Emission of Rough Surfaces Calculated by the Integral Equation Method With Comparison to Three-Dimensional Moment Method Simulations," *IEEE Transactions on Geoscience and Remote Sensing*, vol. 41, pp. 90–101, Jan. 2003.
- [42] F. T. Ulaby, R. K. Moore, A. K. Fung, "*Microwave Remote Sensing: Active and Passive*"; Artech House: Boston, MA, 1982; vol. III, ch 19., 2001.
- [43] J.E. Gilley and E.R. Kottwitz, "Random roughness assessment by the pin and chain methods," *Applied Engineering in Agriculture*, vol. 12, (1), pp. 39–43, 1995.
- [44] R.C. Gonzales and R.E. Woods, "Digital Image Processing," Second Edition, Prentice Hall, Upper Saddle River, New Jersey, ch. 7.
- [45] E.P. Baltsavias, "Airborne Laser scanning: Basic relations and formulas," *ISPRS Journal of Photogrammetry & Remote Sensing*, vol. 54, pp. 199–214, 1999.
- [46] A. Wehr and U. Lohr, "Airborne laser scanning – an introduction and overview," *ISPRS Journal of Photogrammetry & Remote Sensing*, vol. 54, pp. 68–82, 1999.

- [47] G.A. Neumann, J. B. Abshire, O. Aharonson, J. B. Garvin, X. Sun, and M. T. Zuber, "Mars Orbiter laser Altimeter pulse width measurements and footprint-scale roughness," *Geophysical Research Letters*, vol. 30, no. 11, pp. 15-1–15-4, 2003.
- [48] National Research Council, Space Studies Board, "Earth Science and Applications from Space: National Imperatives for the Next Decade and Beyond," National Academies Press, ch. 11, 2007.
- [49] M. Murakami, *Managing Water for Peace in the Middle East: Alternative Strategies*. Tokyo: United Nations University Press, 1995. Available: <http://www.unu.edu/unupress/unupbooks/80858e/80858E00.htm#Contents>
- [50] V.I. Korzun, *World water balance and water resources of the Earth*, Paris, UNESCO, pp. 1756, 1978.
- [51] European Space Agency, SMOS: ESA's Water Mission, Paris, 2009. Available: http://esamultimedia.esa.int/docs/SMOS/BR-278_low-res.pdf
- [52] S.O. Rice, "Reflection of electromagnetic waves from slightly rough surfaces," *Communications in Pure and Applied Mathematics*, 4, pp. 361–378, 1951.
- [53] P. Beckman, and A. Spizzichino, "The Scattering of Electromagnetic Waves from Rough Surfaces," London, Pergamon Press A., 1963.
- [54] A.G. Voronovich, "Small-Slope Approximation in wave scattering from rough surfaces," *Soviet Physics Journal of Experimental and Theoretical Physics*, 62, pp. 65-70, 1985.
- [55] F. Mattia, T. Le Toan, "Backscattering properties of multi-scale rough surfaces," *Journal of Electromagnetic Waves and Applications*, vol 13, pp. 491–526, 1999.
- [56] J.A. Kong, S.L. Lin and S.L. Chuang, "Microwave Thermal Emission from Periodic Surfaces," *IEEE Transactions on Geoscience and Remote Sensing*, vol. GE-22, no. 4, pp. 337–382, July 1984.
- [57] J. T. Johnson, R. T. Shin and J. A. Kong, "Scattering and thermal emission from a two dimensional periodic surface," *Progress In Electromagnetics Research*, vol. 15, 303–333, 1997.
- [58] M. T. Hallikainen, F. T. Ulaby, M. C. Dobson, M. A. El-Rayes, and L.-K. Wu, "Microwave dielectric behavior of wet soil—Part I: Empirical model and experimental observations," *IEEE Transactions on Geoscience and Remote Sensing*, vol. 23, pp. 25–34, Jan. 1985.
- [59] M. T. Hallikainen, F. T. Ulaby, M. C. Dobson, M. A. El-Rayes, and L.-K. Wu, "Microwave dielectric behavior of wet soil—Part II: Dielectric mixing models," *IEEE Transactions on Geoscience and Remote Sensing*, vol. 23, pp. 25–34, Jan. 1985.

- [60] N. R. Peplinski, F. T. Ulaby, and M. C. Dobson, "Dielectric properties of soils in the 0.3–1.3-GHz range," *IEEE Transactions on Geoscience and Remote Sensing*, vol. 33, pp. 803–807, May 1995.
- [61] V. L. Mironov, M. C. Dobson, V. H. Kaupp, S. A. Komarov, and V. N. Kleshchenko, "Generalized Refractive Mixing Dielectric Model for Moist Soils," *IEEE Transactions on Geoscience and Remote Sensing*, vol. 42, no. 4, pp. 773–785, April 2004.
- [62] P.R. Wolf, *Elements of Photogrammetry, With Air Photo Interpretation and Remote Sensing*. Second Edition, New York: McGraw-Hill, 1983.

BIOGRAPHICAL SKETCH

Juan Carlos Fernandez Diaz was born in 1976 in Tegucigalpa, Honduras, to Venancio Fernandez and Ana Maria Diaz. He also has one sister, Maria Esther, and two brothers, David and Jose Venancio. From a very young age, he developed a strong interest towards science and technology, especially earth and space science, aviation, telecommunications and electronics. He was fortunate to attend an American school (Elvel School) from kindergarten to 11th grade, where the teachers motivated his scientific curiosity.

In 1993, he graduated from High School from a program that fulfills the requirements from both the American and Honduran academic curriculum. That same year, he enrolled in the Electrical Engineering program of the Universidad Nacional Autonoma de Honduras (UNAH). Not finding college challenging enough, he decided to work full time while pursuing the bachelor's degree. His first position was as an instructor of the university's astronomical observatory where he acquired knowledge and expertise related to the design, use and maintenance of astronomical instrumentation as well as astronomical data processing and analysis. During this period, he also participated in a traineeship at the European Space Agency Satellite Tracking Station in Villafranca del Castillo, Spain and received a Summer Undergraduate Research Fellowship (SURF) from the California Institute of Technology (CALTECH) to perform scientific research at the Jet Propulsion Laboratory.

Soon after this experience, he accepted a new position with the Honduras national telecommunications commission (CONATEL) as a spectrum planning and engineering technician. He obtained the BS degree in electrical engineering in June 2001,

complimenting the formal academic knowledge with solid experience in telecommunications, space science and technology.

From 2002 to 2005, he continued his career in telecommunications holding positions at a Wireless service provider where he performed functions such as network planning engineer and quality assurance chief. During that same time, he obtained a Master of Business Administration degree with a *summa cum laude* distinction from the Universidad Catolica de Honduras in 2005. During 2004, he applied for a Fulbright Scholarship to participate in a Masters program in the fields of Satellite Applications (Navigation, Communications and Remote Sensing). He was fortunate to receive the scholarship and to be accepted to the University of Florida, Geosensing Systems Engineering graduate program. He started the program during the fall of 2005, and obtained the Master of Science degree in the summer of 2007. After the MS degree, Juan received a University of Florida alumni fellowship to continue his graduate education in pursuit of a PhD degree. During his PhD studies, he also participated in the summer program of the International Space University in 2007 in Beijing, China and 2008 in Barcelona, Spain. He served as a teaching associate for team design projects, which aimed to identify and propose space technologies to monitor and respond to geophysical hazards. In the summer of 2009, Juan participated in an internship program sponsored by the University of Maryland Baltimore County. During this internship he worked at the Microwave Instruments and Technology Branch at the National Aeronautics and Space Administration (NASA) Goddard Space Flight Center.

Juan hopes to keep enhancing his multidisciplinary experience and continue to explore his interest in space science and technology.